Stony Brook University

Evaluation of WRF Planetary Boundary Layer Schemes over the Coastal Waters of Southern New England

A Thesis Presented

by

Matthew J. Sienkiewicz

to

The Graduate School

in Partial Fulfillment of the

Requirements

for the Degree of

Master of Science

in

Marine and Atmospheric Science

Stony Brook University

December 2014

Stony Brook University

The Graduate School

Matthew J. Sienkiewicz

We, the thesis committee for the above candidate for the

Master of Science degree, hereby recommend

acceptance of this thesis.

Dr. Brian Colle – Thesis Advisor
Professor
Institute for Terrestrial and Planetary Atmospheres
School of Marine and Atmospheric Sciences

Dr. Sultan Hameed – Second Reader
Professor
Institute for Terrestrial and Planetary Atmospheres
School of Marine and Atmospheric Sciences

Dr. Marat Khairoutdinov – Third Reader
Professor
Institute for Terrestrial and Planetary Atmospheres
School of Marine and Atmospheric Sciences

This thesis is accepted by the Graduate School

Charles Taber
Dean of the Graduate School

Abstract of the Thesis

Evaluation of WRF Planetary Boundary Layer Schemes over the Coastal Waters of Southern New England

by

Matthew J. Sienkiewicz

Master of Science

in

Marine and Atmospheric Science

Stony Brook University

2014

Winds, temperatures and moisture in the planetary boundary layer (PBL) are often difficult for operational models to predict given the relatively sparse observations and that most model PBL parameterizations were developed over inland locations. Coastal marine layer forecasts are important for the forecasting of severe storms and wind energy resources in the highly populated coastal marine environment of the Northeast U.S. (NEUS). Mesoscale models are known to have large biases in wind speeds and temperatures at these lower levels over coastal waters. The goal of this project is to evaluate the performance of six PBL schemes in the Weather Research and Forecasting (WRF-ARW) model version 3.4.1 in the coastal marine environment of the NEUS. This study region, stretching from the south shore of Long Island out to Cape Cod is an ideal location for an offshore wind energy grid based on such factors as regional energy demand, water depth, and available wind resource.

Verification of six WRF PBL schemes (two non-local, first-order schemes and four local, TKE-order schemes) was performed using a dataset of observations at multiple levels from the

Cape Wind tower in Nantucket Sound from 2003 to 2011, as well as surrounding NDBC and ASOS stations. A series of 30-hour WRF runs were conducted for 90 randomly selected days between 2003 and 2011, with initial and boundary conditions supplied by the North American Regional Reanalysis (NARR). All schemes generally displayed negative wind speed biases over the water. The cool season displayed the largest negative biases as well as a shear profile indicative of an over-mixed boundary layer. It is hypothesized that errors in the model SST field in Nantucket Sound aided in the too-stable (unstable) model MABL structures during the warm (cool) seasons and the resultant under-mixed (over-mixed) wind shear profiles. Additional model verification from three Long-EZ aircraft flights during the Improving the Mapping and Prediction of Offshore Wind Resources (IMPOWR) field campaign during strong southwesterly flow and a developing low-level jet (LLJ) supported the hypotheses. WRF simulations show that most schemes underestimated the height and magnitude of the LLJ, while overestimating the static stability below the LLJ in the vicinity of Nantucket Sound. A warmer SST field was found to improve the near-surface thermal and moisture profiles. Model runs were forced with a variety of analyses, and it was found that even for long simulations the results were more sensitive to the boundary conditions than to the PBL schemes.

Table of Contents

List of Tables

Chapter 2 **Page**

Chapter 3

List of Figures

Chapter 1 **Page**

Chapter 2

Chapter 3

Chapter 4

Chapter 5

Acknowledgments

Financial support for this research project was given by the Department of Energy.

I would like to thank my advisor Dr. Brian Colle for his continued support and guidance throughout this project.

I would also like to thank my committee members, Dr. Sultan Hameed and Dr. Marat Khairoutdinov for their assistance and help.

I would like to give thanks to Dr. Dana Veron and Dr. Cristina Archer at the University of Delaware for the acquisition, quality control, and continued support and guidance with the data obtained from the Cape Wind meteorological mast.

A special thanks to Dr. John Mak, the pilot of the Long-EZ aircraft used during the IMPOWR field campaign, for performing the flights and aiding in the quality control and interpretation of the aircraft data.

Particular thanks go to all of my friends and colleagues at SoMAS for their endless support, advice, and tolerance.

Chapter 1: Introduction

1.1 Background

As alternative energy sources such as offshore wind power become more common, offshore wind resource mapping and forecasting will increase in demand. Given the combination of a high population density, shallow coastal bathymetry, and potentially high available wind resource, the coastal waters of the northeast United States are ideal for offshore wind energy (Dvorak et al. 2012). Since in situ observational data is spatially scarce in offshore areas and few observations are collected at the height of wind turbine hubs, numerical mesoscale models are necessary for offshore wind resource mapping and operational forecasting. Kinematic and thermodynamic processes in the lowest part of the atmosphere where these wind turbines are located, known as the planetary boundary layer (PBL), are parameterized in these mesoscale models by various surface layer and PBL schemes. However, these models are known to have large biases in wind speeds near the surface in these coastal waters (Colle et al. 2003). Largely unknown are the regional biases above the water surface around turbine hub height and across the rotor-swept area. Understanding the systematic errors of the available planetary boundary layer schemes in mesoscale models will provide increased insight for offshore wind resource mapping, as well as wind energy planning and forecasting.

1.2 Offshore Wind Power Challenges

Archer et al. (2013) addressed three main topics relevant to offshore wind farm development: (1) offshore wind resource assessment, (2) wind power forecasting, and (3) turbulent wake losses of wind farms. Wind resource assessment in coastal and offshore areas currently

suffers from a lack of observations at turbine hub height, and the need for more multilevel observations of wind and temperature on offshore platforms was identified. Understanding and modeling of coastal processes is also necessary to accurate wind resource assessment and wind forecasting, yet PBL parameterizations have not been comprehensively evaluated in this offshore area. Since power is proportional to the cube of the wind speed, small wind speed forecast errors can result in large errors in power production. Accurate representation of mesoscale and synoptic-scale processes are important for both hour-ahead and day-ahead power production forecasts, upon which hinge unit commitment and scheduling decisions, as well as market trading.

1.3 Marine Atmospheric Boundary Layer

Over land, the atmospheric boundary layer typically displays a distinct diurnal trend (Fig. 1.1). After sunrise, solar heating warms the surface and results in convection and large turbulent eddies that create a mixed layer capped by an entrainment zone where mixing of free atmosphere air and boundary layer air takes place. After sunset, radiational cooling at the surface leads to the formation of a stable (nocturnal) boundary layer. Above the nocturnal boundary layer turbulence decays in the remnants of the convective mixed layer, now referred to as the residual layer. (Stull 1988)

Over the ocean the large heat capacity of water combined with mixing within the oceanic mixed layer results in a dynamic and slowly varying lower boundary for the marine atmospheric boundary layer compared to over land. As a result the MABL is more spatially homogeneous than over land with little to no diurnal trend. Variability in the MABL over the open ocean lends itself mostly to the passage of synoptic and mesoscale systems, as well as sharp thermal boundaries found near ocean currents. (Stull 1988)

In low-wave conditions the ocean surface drag is relatively small, resulting in stronger and more geostrophic winds over the water than over the land. The MABL is typically moister than the continental boundary layer and often characterized by near-neutral stability and the presence of clouds at the top of the boundary layer (Garratt 1992). Strong deviations from the near-neutral stability regime of the MABL in coastal areas can be caused by the advection of continental air offshore or maritime air onshore due to either changing synoptic and mesoscale conditions or the initiation of land- and sea-breeze circulations (Archer et al. 2013). Very unstable MABL conditions can be found during cold continental air outbreaks over warmer waters, resulting in large latent heat fluxes that vastly exceed the typically small sensible heat fluxes (Garratt 1992). Angevine et al. (2006) showed the presence of a highly stable marine boundary layer over the Gulf of Maine due to the summertime advection of warm continental air over cool waters. Air leaving the continent at night already exhibits stable conditions while mixed-layer air leaving the continent during the day undergoes rapid (within 10 km of the coastline) and shallow (50-100 m) stable internal boundary layer (IBL) formation.

1.3.1 Coastal and Marine Low Level Jets

Boundary layer wind maxima known as low-level jets (LLJs) occur adjacent to terrain along the U.S. West Coast (Olson et al. 2007), ahead of cold frontal systems along the U.S. East Coast (Bell and Bosart 1988), differential heating along the East Coast (Colle and Novak 2010), and over the Great Plains during the summer at night (Storm et al. 2009). Nocturnal LLJs can occur over land when the development of the stable nocturnal boundary layer suppresses turbulence and the flow above decouples from the surface, resulting in supergeostrophic wind speeds. Inertial oscillations of the jet-level winds due to the frictional decoupling from the surface, as well as the

baroclinicity resulting from either the sloping terrain (e.g. Great Plains) or the sloping characteristic of the inversion within the coastal marine boundary layer, are frequently attributed to the formation of these LLJs. These LLJ events can drastically increase the available wind resource in a region. However, the sharp shear effects and subsequent turbulence production may also have negative impacts on wind turbines, making the observation, understanding and accurate numerical modeling of LLJs crucial to the wind energy industry. (Storm et al. 2009)

Colle and Novak (2010) showed the existence of a diurnally-forced LLJ in the New York Bight region that often consisted of wind speeds in excess of 13 m s^{-1}. Occurrences of the New York Bight Jet (NYBJ) peak in the late spring time when the land-sea temperature contrast is the greatest, on days when the flow is primarily southwesterly around a Bermuda high pressure system. The jet maxima, which were part of a larger scale coastal wind enhancement in the coastal southern New England region, were found to occur at ~150 m AMSL and contain both inertial and baroclinic components.

Helmis et al. (2013) used various observational datasets from the CBLAST-Low field campaign to investigate the presence of several summertime LLJ structures above Nantucket, MA. Similar to Colle and Novak (2010) it was found that the favored synoptic setup for the LLJ events consisted of a stationary Bermuda high pressure system and a low-pressure system in the northeast United States. The presence of the marine sloping inversion was found to play a role in supplying baroclinicity and inertial oscillations were associated with the LLJ structures between 200-250 m AMSL.

1.4 Accurate Modeling and Forecasting of the MABL

Ohsawa et al. (2009) identified three main contributing factors to the accurate representation of offshore winds at the Horns Rev wind farm in Denmark, using the PSU/NCAR mesoscale model MM5: (1) the accuracy of the SST field used as the lower boundary in the model, (2) use of the four dimensional data assimilation (FDDA) option, and (3) the selection of the planetary boundary layer scheme within the model. Horizontal resolution and model nesting configurations were found to not have as large an impact on the modeled offshore winds as the three factors listed above.

1.4.1 Planetary Boundary Layer Schemes in Mesoscale Models

In the turbulent boundary layer, equations for momentum, moisture, and sensible heat cannot be explicitly solved. As a result the following equations, using statistically averaged flow fields, are used:

Eq. 1.1 $$\partial\bar{u}/\partial t = -\rho^{-1}\,\partial\bar{p}/\partial x + f\bar{v} - \partial(\overline{u'v'})/\partial z$$

Eq. 1.2 $$\partial\bar{v}/\partial t = -\rho^{-1}\,\partial\bar{p}/\partial y + f\bar{u} - \partial(\overline{u'w'})/\partial z$$

Eq. 1.3 $$\partial\overline{\theta_v}/\partial t = \left(\rho c_p\right)^{-1}\partial\overline{R_N}/\partial z - \partial\left(\overline{w'\theta_v{}'}\right)/\partial z$$

Eq. 1.4 $$\partial\bar{q}/\partial t = -\,\partial(\overline{w'q'})/\partial z$$

The problem with these equations, known as the turbulence closure problem, is that if equations are used to calculate the averaged quantities (second-order moments), third-order moments would appear. So these higher-order terms are often parameterized in numerical models using either known values at the grid point (local PBL closure schemes) or known quantities in the region of the grid point (non-local PBL closure schemes). If the second-order terms are parameterized in a scheme and the above equations are solved, the scheme is said to be first-order or *K*-closure. A

second-order scheme would solve equations to calculate the second-order terms and parameterize the third-order moments. First-order schemes use eddy diffusivities *K* to relate the turbulent fluxes of a quantity to the local gradient of that quantity. Values for *K* can be determined by several different methods; they can be assigned, a *K*-profile for the PBL can be assigned, or they can be determined in terms of the TKE. Mainly the second option is used in first-order PBL schemes, but *K*-closure is not accurate for highly unstable boundary layers. The third option is an intermediate approach that utilizes a prognostic turbulent kinetic energy equation to determine the eddy diffusivity coefficients, known as one-and-a-half order closure or *TKE*-closure, without explicitly solving for the second-moment terms. The master equations for these TKE schemes are

Eq. 1.5 $$\frac{\partial \bar{e}}{\partial t} = -\frac{1}{\rho}\frac{\partial}{\partial z}\rho\overline{w'e'} - \overline{u'w'}\frac{\partial u}{\partial z} - \overline{v'w'}\frac{\partial v}{\partial z} + \beta\overline{w'\theta_v{}'} - \varepsilon$$

Eq. 1.6 $$\overline{u'w'} = -K_m\,\partial u/\partial z$$

Eq. 1.7 $$\overline{v'w'} = -K_m\,\partial v/\partial z$$

Eq. 1.8 $$\overline{e'w'} = -K_e\,\partial \bar{e}/\partial z$$

Eq. 1.9 $$\overline{w'\theta_v{}'} = -K_h\,\partial \theta_v/\partial z$$

where ε is the TKE dissipation rate, β is the buoyancy coefficient, and $\bar{e}$ is the TKE. The coefficients K_m, K_h, and K_e represent the eddy diffusivity coefficients for momentum, heat, and TKE, respectively, and are calculated using

Eq. 1.10 $$K_c = S_c l \bar{e}^{1/2}$$

where $S_c$is an empirically determined length scale and l is the master length scale. The definitions of these variables may vary from scheme to scheme. In non-local schemes, a gradient adjustment term is added to equations 8 and 9 to help account for non-local mixing. (Garratt 1992; Xie et al. 2012; Holtslag and Boville 1992).

Between schemes there are many differences in how the PBL top is defined and calculated, as well as how entrainment processes are treated (Shin and Hong 2011). Non-local first-order schemes define the top of the PBL to be where the bulk Richardson number first exceeds a critical value. Local TKE-closure schemes use a low TKE threshold to define the top of the boundary layer. Xie et al. (2012) found that local TKE-closure schemes produced unrealistically shallow PBL heights in simulations over Hong Kong compared to non-local first-order schemes.

1.4.2 WRF PBL Scheme Evaluations

To date, most WRF PBL scheme evaluations have been performed over land, in stable or neutral conditions. Shin and Hong (2011) compared five PBL schemes with observations for one day at a site in Leon, Kansas. They found vast inconsistencies between the five schemes for thermodynamic variables during the daytime and large biases in wind speeds during the night. While the higher-order schemes performed the best, it was found that no schemes accurately simulated the stable boundary layer. Storm et al. (2009) tested various WRF PBL configurations during nocturnal low-level jet (LLJ) events over West Texas and Kansas. In all model configurations, the heights of these LLJs were found to be overestimated, and the wind speeds were underestimated. These LLJs contribute significantly to the wind resource of the region and while all model configurations improved significantly on a simple $1/7^{th}$ power law approximation, which is a wind profile power law assuming neutral stability, Storm et al. speculates that the wind energy industry may require more accurate model results before committing to the region. Shimada et al. (2011a) compared the model outputs of seven different PBL schemes to wind profiler data from ten coastal sites across Japan and found a positive wind speed bias in the lower PBL in all schemes. They concluded that the bias is systematic of the WRF model and therefore cannot be

removed simply by changing PBL schemes. Gathering in situ observations over the ocean is a cumbersome and expensive process, and therefore PBL scheme comparisons for marine environments have largely been avoided. Suselj and Sood (2010) performed WRF PBL simulations in the North Sea and Baltic Sea and altered the MYJ PBL and surface layer schemes to better represent the master length scale l. They found that the updated schemes better represented wind shear in the lowest 30 meters, but also state that coupling of the WRF with a wave model as well as implementation of a highly-resolved sea surface temperature field will help to greatly improve the lower marine PBL. Shimada et al. (2011b) evaluated the performance of PBL schemes for the whole year of 2005 at the Shirahama offshore research platform in Japan and found large positive wind speed biases in the surface layer and PBL, and negative biases above 1-km. Removing this bias resulted in a decrease in the error of wind energy estimates from 47% down to 4%. However, the authors go on to conclude that more offshore PBL evaluations and studies are necessary to improve the accuracy of offshore wind speed estimates.

1.4.3 Sensitivity of WRF MABL Simulations to SST Field

Sea surface temperatures play a significant role in determining sensible and latent heat fluxes into the lower MABL, which in turn contribute towards the stability and momentum fields as well as cloud formation within the MABL. Accurately resolving mesoscale temperature gradients such as SST fronts across currents and in coastal areas is crucial to the accurate representation and forecasts of coastal processes within mesoscale models. LaCasse et al. (2007) compared WRF simulations of the MABL over the Florida Shelf and Florida Current using the 0.5 degree RTG SST and the 1-km NASA SPoRT SST product. The higher-resolution NASA SPoRT product led to small improvements in surface momentum and thermal fields over the RTG product.

The SPoRT product also showed an increase in precipitation over the RTG simulations as well as an altered MABL structure downwind of the warmer Florida Current.

1.4.4 Sea Surface Temperature Variability in the Southern New England Shelf Region

The sea surface temperature field over the continental shelf of southern New England is highly heterogeneous. The shallow Nantucket Sound heats up in the spring and stays warm throughout the warm season compared to the surrounding waters. Cooler water makes its way south from the Gulf of Maine and mostly branches eastward to Georges Bank. However, some of the cooler water branches westward and pools over the shallow Nantucket Shoals to the south-southeast of Nantucket. This water, which is normally confined to the Nantucket Shoals due to westward tidal forces being balanced by eastward transport, has been observed to make westward excursions in the form of narrow tongues of cooler water that enhance the SST gradients south of Martha's Vineyard. High resolution SST observations from a Pelican aircraft during the CBLAST-Low field campaign found horizontal SST gradients as large as 6 °C over a horizontal distance of 5 km attributed to these cold tongues (Edson et al. 2007). Navy Coastal Ocean Model (NCOM) simulations showed that these cold tongues can be attributed to deviations from the summertime prevailing southwesterly winds by the passage of synoptic systems that allow for the westward transport of the cooler water off of the Nantucket Shoals. (Hong et al. 2009)

1.5 Motivation

The goal of this study is to evaluate the performance of six PBL schemes in the WRF-ARW model version 3.4.1 in the coastal marine environment of the northeast United States (NEUS). This region, stretching from the south shore of Long Island to Georges Bank, has been

identified by Dvorak et al. (2012) as an ideal location for an offshore wind energy grid based on such factors as regional energy demand and water depth, as well as available wind resource due in part to such meteorological features as the New York Bight jet (Colle and Novak 2010). In the region, the capability of the mesoscale models such as the WRF-ARW to accurately represent offshore winds are not fully understood. This study aims to address the following questions:

1. What are the systematic errors (biases) of the WRF PBL schemes in wind speed, temperature and dew point in the region, and how do these biases vary spatially, diurnally and seasonally?
2. How do these biases change with height above the water surface and are there certain stability and flow regimes that are more susceptible to these biases?
3. How do perturbations to the SST field, as well as different analyses used as initial and lateral boundary conditions, alter the simulated MABL structure?

This thesis will be organized as follows: Chapter 2 will discuss the data and methods used in this study. Chapter 3 will discuss the evaluation of six WRF PBL schemes using available surface in situ observations as well as a unique multi-level meteorological tower dataset. Chapter 4 will discuss high-resolution observations of the MABL from three aircraft flights as part of the IMPOWR field campaign, as well as comparison of the observations to WRF simulations. Chapter 5 discusses the results of several sensitivity tests, and Chapter 6 summarizes the work and describes future goals.

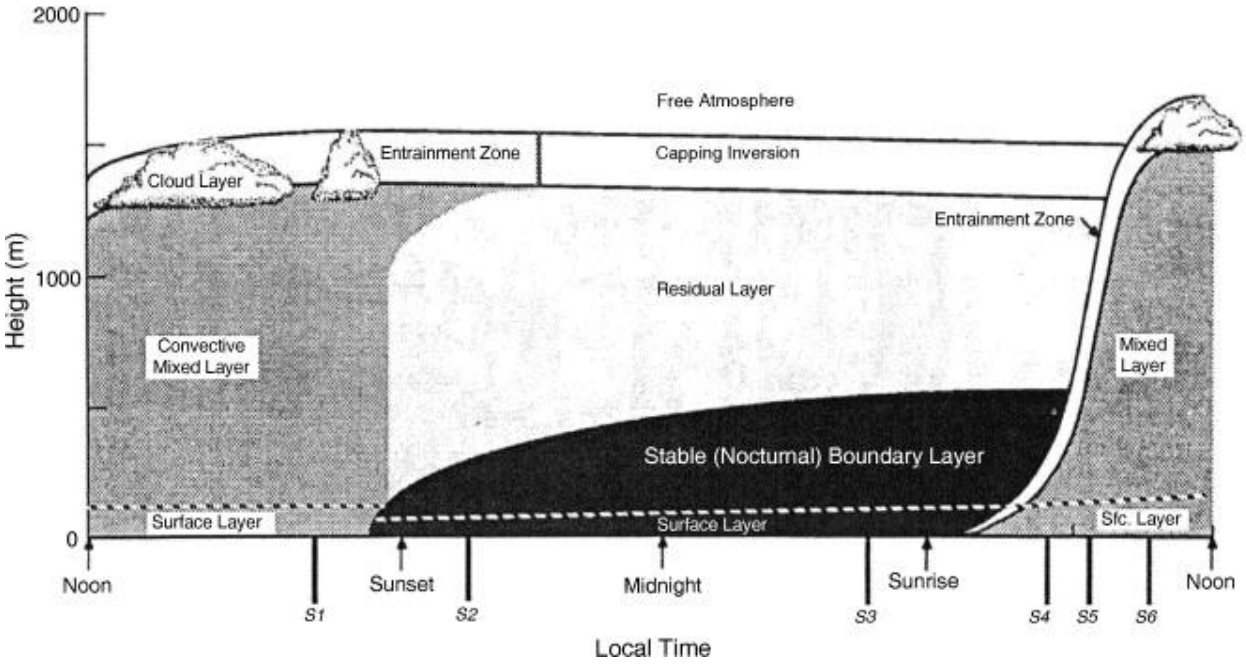

Figure 1.1. Schematic representing the evolution of the boundary layer over land from Fig. 1.7 in Stull (1988).

Chapter 2: Data and Methods

2.1 Instrumentation and Datasets

A number of different in situ observational datasets were used for verification of the WRF PBL schemes. Observations over the coastal waters were provided by NDBC moored buoys and Coastal Marine Automated Network (C-MAN) stations and observations at the surface over the adjacent land were provided by NWS ASOS stations (Fig. 2.1). Wind power resources are not measured at the surface, however, so observations that extend through a greater depth of the PBL are necessary. NWS radiosondes provided intermittent observations of temperature, moisture, and winds throughout the PBL but the most important dataset was that of the Cape Wind meteorological mast (Fig. 2.1). This mast provides data at multiple levels (wind speed and direction at 20, 41 and 60 m and temperature and pressure at 10 and 55 m) within the PBL, and it is located in the coastal waters where a wind farm is planned. To obtain an observational dataset with higher spatial and temporal resolution, flights were completed for a set of days with the Long-EZ aircraft. More details about each of these observational datasets can be found in the following subsections.

2.1.1 NDBC Moored Buoys and C-MAN Stations

Eleven NDBC moored buoys and three C-MAN stations were selected in the coastal and offshore region extending from Delaware Bay to the south up to Portland, ME to the north. The buoys record hourly observations of wind speed and direction, temperature and dew point temperature. The anemometer is located 5 m above the water surface, and the temperature and dew point temperature sensors are located 4 meters above the water surface. The C-MAN stations are

fixed platforms instead of floating platforms like the buoys, and the height of the instrument sensors varies station to station. The three C-MAN stations used in this study have instruments at heights between 24 and 32 meters AMSL. (NDBC 2009)

2.1.2 NWS ASOS Stations

Hourly observations from fourteen National Weather Service Automated Surface Observing System stations were selected for this study from Massachusetts, Rhode Island, Connecticut, New York and New Jersey (Fig. 2.1). The ASOS stations uniformly record wind speed and direction at the standard level of 10 meters AGL and temperature and dew point temperature at 2 meters AGL.

2.1.3 NWS Radiosondes

Twice daily at 0000 UTC and 1200 UTC weather balloons are launched from 102 locations across the United States. This study utilized profiles of wind speed and direction, temperature, dew point temperature, virtual potential temperature and mixing ratio of the lowest 2 km derived from radiosondes launched from Chatham, MA (CHH; Fig.2.1).

2.1.4 Cape Wind Meteorological Mast

Unique to this study is the inclusion of a multi-level dataset of wind speed and direction, temperature and pressure from the Cape Wind Meteorological Mast located in Nantucket Sound (Fig. 2.1). Sonic and cup anemometers, as well as temperature and pressure sensors, were installed and maintained on the mast from 2003 through 2011. Wind, temperature, and pressure observations were recorded at a frequency of 10 minutes, however only hourly observations were

used in this verification study. The anemometers were located at heights of 20, 41 and 60 m AMSL. The temperature and pressure sensors were located at 10 and 55 m AMSL. Quality control of the wind observations was performed by collaborators at the University of Delaware using a three-step process:

1. General cleaning, i.e., removal of outliers, unphysical values, and values that were incorrectly repeated because either the wind instrument or the data logger was malfunctioning. Also, wind speed readings that were below 2.5 m/s or above 25 m/s were removed.
2. Removal of the tower shadowing effect via the "Smart Direction" method. In brief, wind directions were first identify for which one of the two instruments (sonic or vane) was entirely in the wake and its wind direction readings were replaced with those from the other instrument. This swapping of the wind directions ensures that only the upwind anemometer is retained for wind direction information in wake conditions. The rest of the time, both directions are retained. In addition, wind readings were flagged as invalid if:
    - the wind directions from the two instruments were off by more than 15 degrees;
    - the ratio of wind speeds was greater than 1.3 or smaller than 0.7 (i.e., error ±30%);
    - excessive wind shear was present (i.e., wind speed more than doubled between two consecutive layers);
    - sudden jumps in wind speed occurred (i.e., wind speed more than doubled between two consecutive records).

3. Generation of single time series at each of the three levels (20, 41, and 60 m) from the two original time series (from the sonic and from the cup/vane). The final value of wind speed and direction at this step was either the mean of the two values if both were present or the non-null value if only one non-null value was present. These single time series of wind speed and direction at each level were used for the model validation. (Personal communication with Cristina Archer, University of Delaware)

Due to the inability of obtaining the raw observational data of wind speed and direction from 2008-2011, quality controlled wind data is only available for 2003-2007 in this study.

2.1.5 Long-EZ Aircraft with AIMMS-20 Instrument

Long-EZ aircraft flights were conducted as part of the Improving the Mapping and Prediction of Offshore Wind Resources (IMPOWR) field campaign during the spring and summer of 2013 and 2014. The aircraft was fitted with the Aircraft-Integrated Meteorological Measurement System (AIMMS-20) instrument which is capable of up to 40 Hz observations of three-dimensional winds, temperature, pressure and relative humidity. Flight operations were based out of Brookhaven Airport (KHWV) in Shirley, NY and targeted the coastal areas of Nantucket Sound, Buzzard's Bay and Block Island Sound, as well as offshore areas to the south. Various flight maneuvers such as constant-level flight legs, spiral soundings in the lowest 2 km and slant-sounding flight legs below 1 km were conducted in order to provide MABL profiles of momentum, thermal, and moisture fields, as well as turbulence and flux quantities.

2.2 WRF Simulations

This study implemented the Advanced Research WRF (Weather Research and Forecasting; Skamarock et al. 2008) model version 3.4.1 and six of the included planetary boundary layer (PBL) schemes (Table 2.1). Two first-order schemes, Yonsei University (YSU; Hong et al. 2006) and Asymmetric Convective Model (ACM2; Pleim 2007), were evaluated along with four 1.5 order or TKE closure schemes; the Mellor-Yamada-Janjic (MYJ; Mellor and Yamada 1982), Quasi-Normal Scale Elimination (QNSE; Sukoriansky et al. 2006), Mellor-Yamada Nakanishi and Niino Level 2.5 (MYNN2.5; Nakanishi and Niino 2009), and Bougeault-Lacarrère (BouLac; Bougeault and Lacarrère 1989) schemes. The WRF was used for two separate evaluation periods: the Historical Period centered on the available data from the Cape Wind Meteorological Mast (2003-2011), and the IMPOWR aircraft flights conducted in June 2013. The model domains and initial and lateral boundary conditions varied between the two verification periods.

2.2.1 Historical Period

The outermost domain of the WRF consisted of 36-km grid spacing with one-way nesting down to 12-, and 4-km horizontal resolution over the operational area. Thirty-seven half-sigma levels were used, with maximum resolution in the boundary layer. The lowest 1 km contained 13 half-sigma levels. The lowest model level was located in the surface layer at an altitude of approximately 8 m above ground level, as in Shin et al. (2011).

Ninety dates were randomly and uniformly selected between 2003 and 2011, corresponding with the availability of data from the Cape Wind Meteorological Mast. The dates were evenly distributed between the cool season (October-March) and the warm season (April-September), as well as between 0000 UTC and 1200 UTC model initialization times. The WRF

was run for each of these dates out to 30 forecast hours using each of the six different PBL schemes. The simulation was kept to 30 hours in order to limit the verification to short-term (hour-ahead and day-ahead) forecasts comparable to what would be used in operational wind power forecasting. The North American Regional Reanalysis (NARR; Mesinger et al. 2006) was used as the initial and lateral boundary conditions. In order to improve on the one-degree Reynolds SST used in the NARR, the 0.5° Real-time Global (RTG) daily gridded sea surface temperature field was prescribed as the lower boundary. History files from the 36- and 12-km domains were discarded and only the 4-km domain was used in the verification (Fig. 2.2). Furthermore, the first 6 model forecast hours were ignored in the verification as model spin-up time.

2.2.2 IMPOWR Flights

For the WRF simulations of the IMPOWR Flights, a large 4-km domain was used as the outer domain with a one-way nested inner 1.33-km domain (Fig. 2.3). The initial and lateral boundary conditions were supplied by hourly analyses from the NCEP Rapid Refresh (RAP; Benjamin et al. 2009). The RAP was chosen for the WRF simulations of the flight cases because of the higher spatial and temporal resolution, as well as improved data assimilation methods over other available gridded analyses. The WRF domains were altered for the historical period to accommodate the smaller RAP spatial coverage. The $1/12^{th}$ degree RTG daily gridded SST product was prescribed for all WRF runs. The history interval for the 1.333-km domain was increased to 5 minutes in order to allow for interpolation of the model variables to the aircraft position in time and space.

2.3 WRF Model Verification

WRF model variables were bi-linearly interpolated to the latitude and longitude coordinates of each station used in the verification. The creation of a gridded observational dataset for verification was deemed unfeasible due to the sparse buoy observational network and inconsistencies in instrument heights between buoys, C-MAN stations, ASOS stations and the Cape Wind Meteorological Mast. For stations with instrument heights above that of the lowest model level (~7.5 m), model results were vertically and linearly interpolated to the instrument height using geopotential height on the model levels as the vertical coordinate. For NDBC moored buoys the lowest model level winds were reduced to the anemometer height of 5 m using the wind power law and an exponent experimentally determined for neutrally stable marine conditions by Hsu et al. (1994):

Eq. 2.1 $$\frac{u_2}{u_1} = \left(\frac{z_2}{z_1}\right)^P, where\ P = 0.11$$

Lowest model level temperatures and dew point temperatures were compared directly to buoy 4-m observations. ASOS 2-m temperature and dew point temperature observations were compared with the WRF model-calculated 2-m values. Model dew point temperatures were calculated via the Clausius-Clapeyron equation using the model pressure and mixing ratio values. Mean error (ME) and mean absolute error (MAE) were calculated for wind speed, temperature and dew point at each of the station locations using the following equations, respectively:

Eq. 2.2 $$ME = \frac{1}{n}\sum_{i=1}^{n} f_i - o_i$$

Eq. 2.3 $$MAE = \frac{1}{n}\sum_{i=1}^{n} |f_i - o_i|$$

where *f* represents the model forecast value and *o* represents the observation. ME and MAE scores were also divided into day (1200 UTC to 2300 UTC) and night (0000 UTC to 1100 UTC) diurnal

periods, as well as warm (April through September) and cool (October through March) seasons. Confidence in ME and MAE scores was approximated using the bootstrap resampling method (REF), where 95% confidence levels were calculated based on resampling the datasets 1000 times.

Wind shear for the Cape Wind Meteorological Mast verification was defined as the difference in wind speed between the 60-m and 20-m levels:

Eq. 2.4 $$WSHR = \left|\overrightarrow{V_{60}}\right| - \left|\overrightarrow{V_{20}}\right|$$

Static stability was similarly calculated as the difference in potential temperature between the 55-m and 10-m levels:

Eq. 2.5 $$SS = \theta_{55} - \theta_{10}$$

2.4 IMPOWR Flight Verification

To accompany the aircraft observations of winds, temperature, pressure, and relative humidity, virtual potential temperature (θ_v) and mixing ratio were calculated from the processed flight data. Five-minute output of model variables from the 1.33-km domain were bi-linearly interpolated to the aircraft coordinates, linearly interpolated to the aircraft altitude, and linearly interpolated to the aircraft position in time, resulting in simulated flight-level datasets as if the aircraft had flown through the model simulations.

Flight observations during aircraft spirals were bin-averaged to uniformly distributed altitude levels to create profiles of wind speed, virtual potential temperature, and mixing ratios that were compared with model profiles at the aircraft spiral time and location. Similarly, vertical cross-sections of wind speed and potential temperature in the MABL were created for aircraft slant-sounding flight legs by hand-contouring the observed values in the vertical plane. Model vertical cross-sections were similarly created using the simulated flight-level datasets. Horizontal constant-

altitude flight legs were compared to model results using plotted horizontal model cross-sections at flight level.

Flight-level data were used to estimate such parameters as turbulent kinetic energy (TKE), eddy-diffusivity, and momentum fluxes using the methods described in Zhang et al. (2011). TKE was calculated using the velocity perturbations and a 30-second sliding-window average:

Eq. 2.6 $$\bar{e} = \frac{1}{2}\left(\overline{u'^2} + \overline{v'^2} + \overline{w'^2}\right)$$

The sampling rate of the instrument is 40 Hz, but only 20 Hz data were used in this study and should have been able to capture the majority of the TKE. Zhang et al. (2011) compared 1-Hz data to 40-Hz data collected in the lower boundary layer of the outer rainbands of Hurricane Frances during the CBLAST (Couple Boundary Layer Air-Sea Transfer; Black et al. 2007) experiment and found that the 1-Hz data captured approximately 75% of the momentum flux and 70% of the TKE. However, the 1-Hz flight data could not resolve eddies smaller than 200 m. These TKE values were compared to the TKE values output by the four TKE-closure schemes implemented in this study (MYJ, MYNN2, BouLac, and QNSE). The first-order schemes do not predict TKE.

Table 2.1. Description of the six PBL schemes from the WRF-ARW version 3.4.1 proposed for use in this study. Adapted from Shimada et al. (2011a).

Scheme	Turbulence Closure Order	Surface Layer Scheme	Summary
YSU	1.0	MM5	Non-local-K scheme with explicit entrainment layer and parabolic K profile in unstable mixed layer
ACM2	1.0	MM5	Asymmetric Convective Model with non-local upward mixing and local downward mixing
BouLac	1.5	MM5	Designed for use with BEP (Building Environment Parameterization) urban model
MYJ	1.5	MYJ	One-dimensional prognostic turbulent kinetic energy scheme with local vertical mixing
QNSE	1.5	QNSE	A TKE-prediction option that uses a new theory for stably stratified regions
MYNN2.5	1.5	MM5	Predicts sub-grid TKE terms

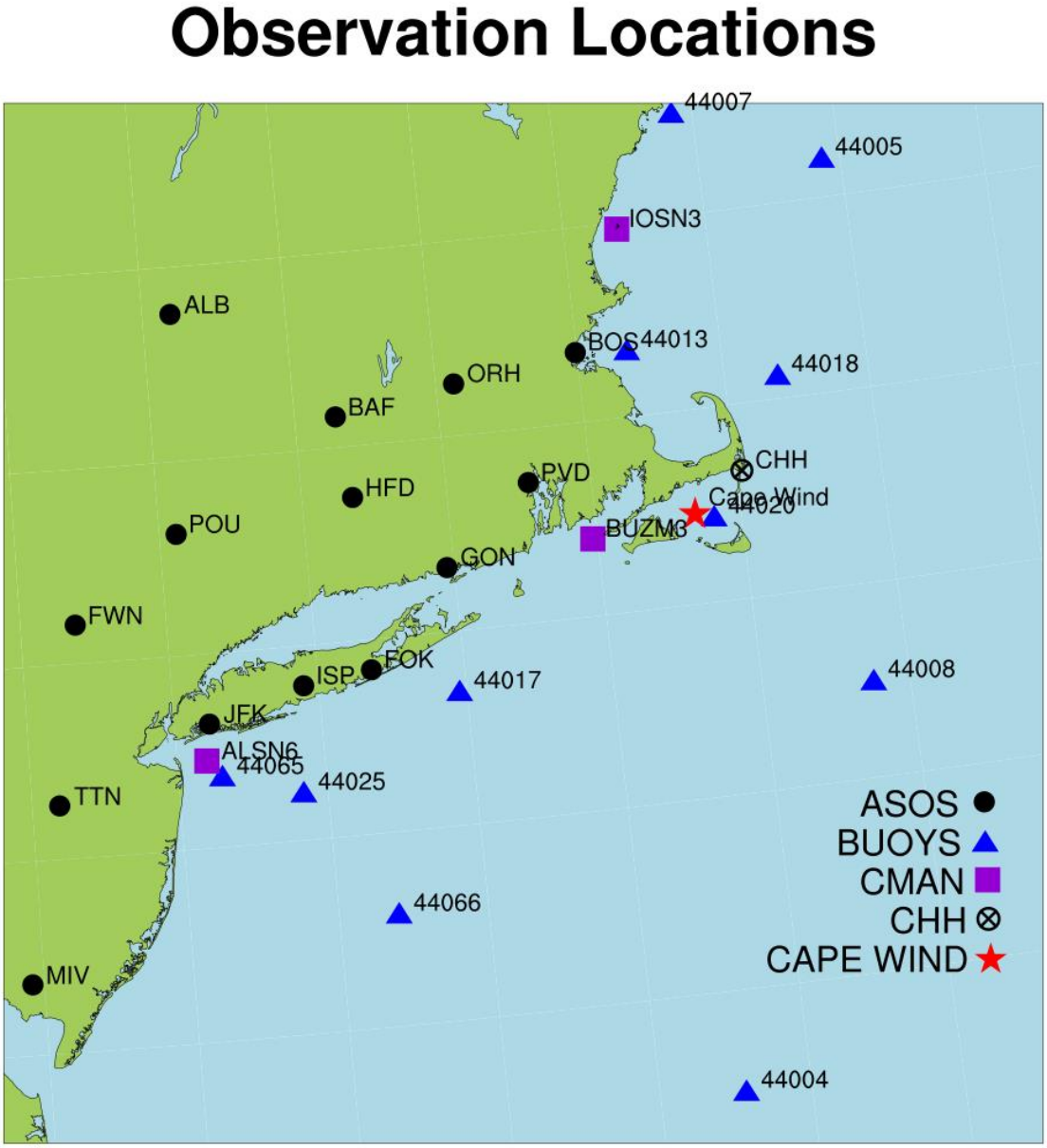

Figure 2.1. Map showing locations of stations used in the verification of WRF PBL schemes.

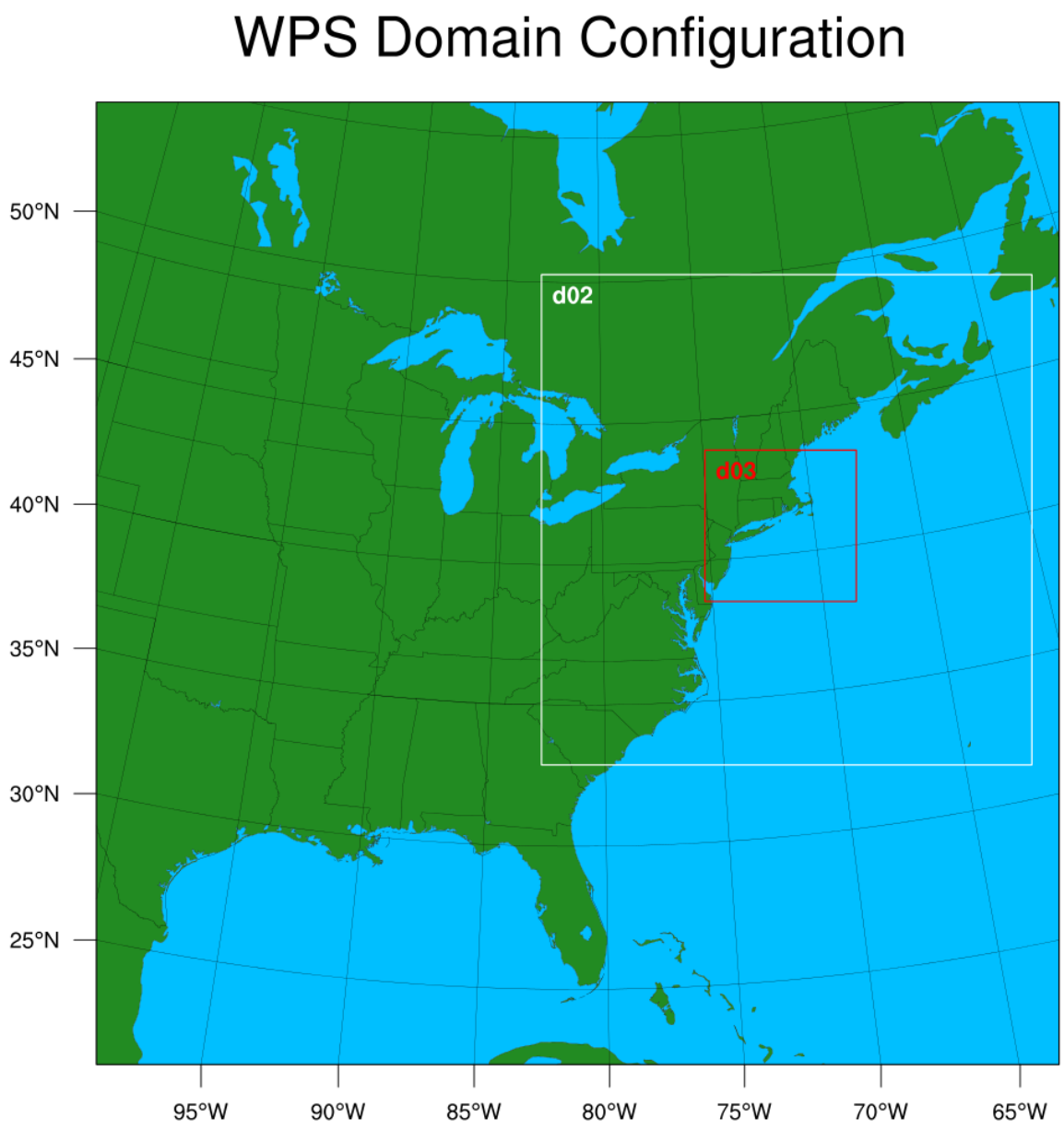

Figure 2.2. Map showing location of WRF domains used in the historical period analysis. Outer map represents the 36-km domain while d02 and d03 are the 12- and 4-km domains, respectively.

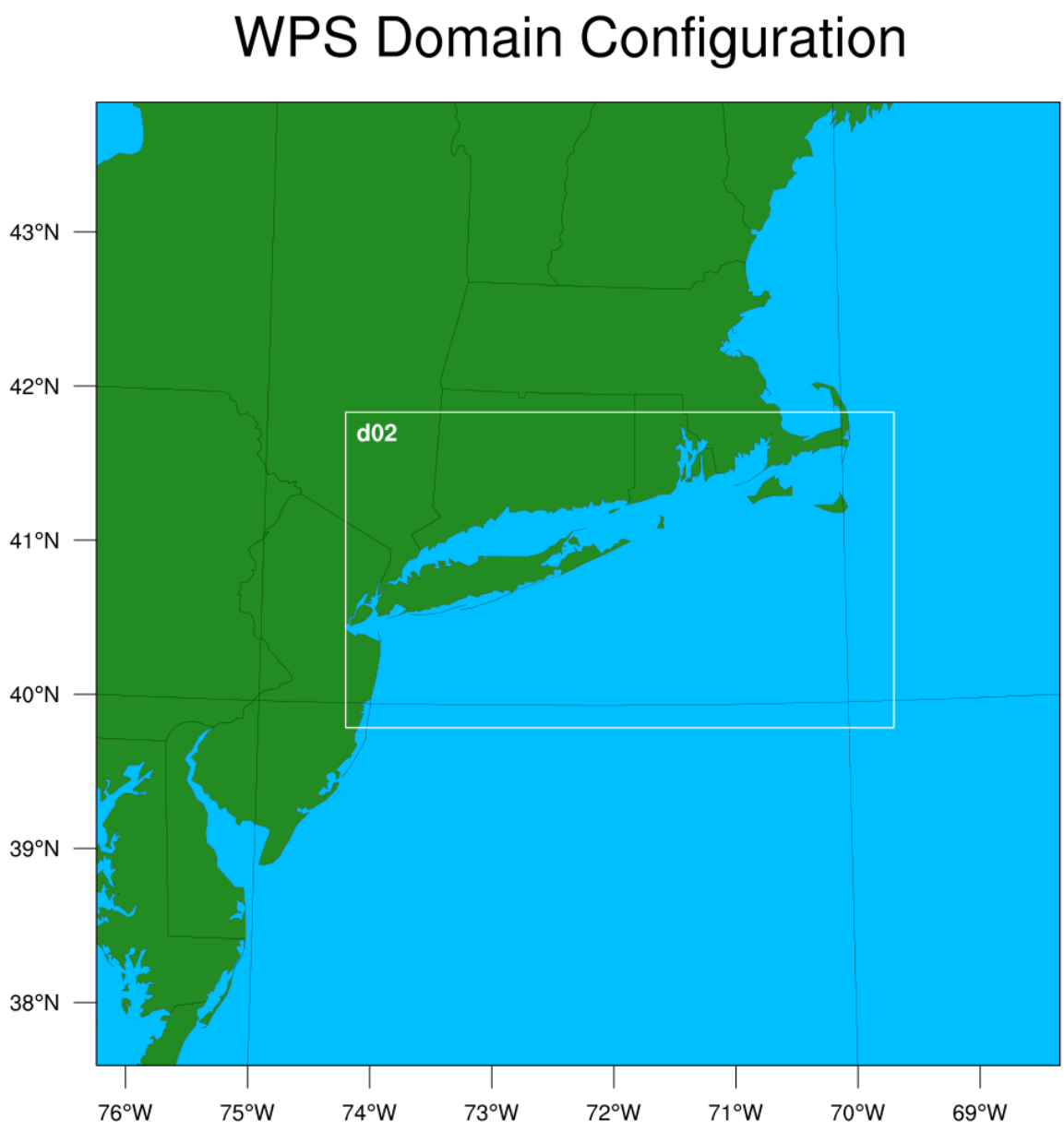

Figure 2.3. Map showing location of domains used for the IMPOWR flight cases. Outer map represents the 4-km domain and d02 is the 1.33-km domain.

Chapter 3: Historical Study Period

3.1 Conventional Observations

3.1.1 NDBC Buoys, C-MAN Stations and ASOS Stations

Model mean error (ME) of wind speed, temperature, and dew point were calculated for 11 NDBC moored buoys, 3 NDBC C-MAN stations and 14 ASOS stations in the model domain. The analysis is divided into day (1200 UTC to 2300 UTC) and night (0000 UTC to 1100 UTC) for the warm season (April to September) and cool season (October to March).

Figure 3.1 shows the mean error in wind speed for each PBL scheme at each station for the warm season daytime. All schemes show positive wind speed mean errors south of Long Island and east of New Jersey. The BouLac scheme shows the largest mean error at buoy 44025 of 0.65 m s^{-1}, and the MYNN2 scheme shows the smallest error of 0.1 m s^{-1}. Similar figures for temperature and dew point temperature mean errors show negative temperature ME (~ -1 °C) for all schemes at buoy 44025 as well as positive dew point temperature ME (0.1 - 0.37 °C) (Fig. 3.2, Fig. 3.3). However, the biases of temperature and dew point temperature at this buoy are not representative of the New York Bight region. Buoys 44005 and 44007 in the Gulf of Maine exhibit positive wind speed ME (0.2 - 1.0 m s^{-1}) for all schemes, as well as negative temperature ME (-0.2 - -0.7 °C) for all but the BouLac scheme. The sign in dew point temperature ME reverses in this region for all schemes from negative near the shore (buoy 44007) to positive offshore (buoy 44005). ME for all variables vary spatially and by scheme for the offshore waters surrounding Massachusetts. Buoys 44018 (east of Provincetown, MA) and 44020 (Nantucket Sound) show neutral to negative wind speed ME for the YSU, MYJ, MYNN2 and QNSE schemes (0 - -0.26 m s^{-1}), compared with positive ME at buoy 44013 in Boston Harbor and the BUZM3 C-MAN station

in Buzzard's Bay. Temperature ME are negative in Nantucket Sound while positive at buoy 44018 for most schemes. Variability in the ME for each variable over the continent also exists for each scheme. The YSU, ACM2, MYNN2 and BouLac schemes show negative wind speed ME at ASOS stations to the north that become positive into southern New York and New Jersey. Alternatively the MYJ and QNSE schemes show positive wind speed ME at most ASOS stations. Temperature ME at the ASOS stations vary spatially for all schemes. For example, strong negative temperature ME exist at BOS for all schemes (-2.8 - -4.0 °C) with positive ME at ORH ~60 km farther inland to the west (0.4 - 0.6 °C). In general, ME for wind speed, temperature and dew point temperature at all observing stations for the warm season daytime exhibit large spatial and inter-scheme variability.

Wind speed ME for the warm season nighttime (0000 - 1100 UTC) exhibit more spatial consistency than during the day (Fig. 3.4). Positive biases are generally present over the continent and offshore wates for all schemes except for in Nantucket Sound and for buoy 44004 off of the continental shelf. Temperature ME are negative in all but the BouLac scheme over the continent, but positive temperature biases are present in the Gulf of Maine for all schemes (Fig. 3.5). Dew point temperature ME are variable and often small for all schemes (Fig. 3.6).

For the cool season (October to March) daytime, temperate ME are generally negative over the continent and the waters south of Long Island for all schemes, with the exception of the BouLac scheme which displays very weak ME in these regions (Fig. 3.8). The QNSE scheme has the strongest biases (< -1 °C) in these regions. The YSU, ACM2 and MYNN2 schemes show weak positive temperature ME at the northern buoys and in Nantucket Sound (0.2 – 0.4 °C). Dew point temperature ME are generally positive at all stations for all schemes, with the exception of the negative ME over the water in the QNSE scheme and two far offshore buoys in the MYJ scheme

(44008 and 44004) (Fig. 3.9). The consistency in temperature and dew point temperature ME is not reflected in the wind speed ME, with large inter-scheme and spatial variability (Fig. 3.7). The wind speed ME in Nantucket Sound are positive for all but the BouLac scheme, but the values in the Gulf of Maine as well as south of Long Island vary in sign and magnitude.

Finally during the cool season nighttime (0000 – 1100 UTC), the dew point temperature ME for all schemes are very similar to during the cool season daytime (Fig. 3.12). The QNSE scheme shows negative temperature ME at most stations while the BouLac scheme shows positive temperature ME at most stations (Fig. 3.11). The temperature ME distribution for the YSU, ACM2, MYJ and MYNN2 schemes is more variable. The YSU, ACM2 and MYNN2 schemes agree on positive temperature ME in the Gulf of Maine. Nantucket Sound is too warm in all schemes (0.1 – 1.1 °C). A positive wind speed ME is shown throughout the entire region save for ~2 out of 28 stations for both the ACM2 and QNSE schemes (Fig. 3.10). The MYJ and BouLac schemes both generally exhibit positive wind speed ME over the land, and neutral to negative ME over the coastal waters. The YSU and MYNN2 schemes exhibit the most variability over both the land and coastal waters in wind speed ME. All schemes show positive wind speed ME in Nantucket Sound ($0.04 – 0.8$ m s^{-1}).

To summarize, the ME for wind speed, temperature and dew point temperature were calculated for each diurnal and seasonal period to elucidate how the various PBL schemes perform under various conditions throughout the historical study period. The data show at all observing stations for each seasonal and diurnal period large spatial and inter-scheme variability, with geographically unique areas like Nantucket Sound often displaying starkly different biases than neighboring stations.

3.1.2 Chatham, MA Soundings

The ME for wind speed, temperature were calculated for each of the WRF PBL schemes using the 0000 UTC and 1200 UTC radiosonde soundings from Chatham, MA (CHH). Sounding times corresponded with model forecast hours 12 and 24. Figures 3.13-15 show the model wind speed mean errors for the lowest 2000 m for all soundings, the warm season soundings, and the cool season soundings, respectively. The wind speed biases are largest and positive for each season in the lowest 200 m for all PBL schemes (1.9 – 3.0 m s^{-1}), before switching sign and becoming slightly negative between 500 and 600 m. All schemes except the BouLac scheme show a local maximum in positive bias at about 100 m during both the warm and cool seasons. The biases below this maximum are higher during the cool season than the warm season. The temperature mean error profiles show that the near-surface temperatures are 0.5-0.75 °C too cool in the warm season (excluding the BouLac scheme) and 0.5-1.4 °C too warm in the cool season (Figs. 3.16-3.18), resulting in model thermal profiles that are too stable in the warm season and not stable enough in the cool season. The profiles of ME for temperature and wind speed for 0000 and 12000 UTC were similar and not shown here.

3.2 Cape Wind Meteorological Mast

3.2.1 Wind Speed

The 60-m wind speed observations are not available after 2007, therefore only the first 53 of the 90 historical dates were included in ME and MAE (Table. 3.1) values for wind speed. MAE scores for each of the six PBL schemes increase from the 20 m level (1.73-1.85 m s^{-1}) up to 60 m (1.86-2.02 m s^{-1}). Average observed wind speeds at the 20-, 40- and 60-m levels were 8.20, 8.86 and 9.27 m s^{-1}, respectively, and so MAE is approximately 21-22% of the magnitude of the

observed wind speeds. The ACM2 scheme exhibits the smallest MAE at all levels, while the QNSE scheme exhibits the largest MAE at all levels. ME is negative at all levels for most schemes and relatively small at these short lead times, with magnitudes under 0.5 m s^{-1}, with the largest biases (0.5-0.8 m s^{-1}) found at the 20 m level. The exception is the BouLac scheme which displays relatively larger biases that increase with height (-0.55 m s^{-1} at 20 m to -0.91 m s^{-1} at 60 m).

ME for each scheme were calculated for day (1200 UTC through 2300 UTC) and night (0000 UTC through 1100 UTC) periods during the warm season (April to September; Fig. 3.19) and cool season (October to March; Fig. 3.20). This allows for a more in-depth investigation of the model wind speed biases as a function of the diurnal heating. During the warm season, wind speed biases for all schemes are largest at the 20-m level during the night and negative, with values between -0.50 and -0.80 m s^{-1}. The negative bias is smaller at the 41- and 60-m levels for both day and night, with the exception of the BouLac scheme, which shows negative biases increasing in magnitude from 20 m to 60 m. During the cool season, the nighttime biases are small, but the daytime biases are consistently negative in sign and increasing in magnitude with height. The largest cool season wind speed biases are found in the BouLac scheme, with a daytime value approaching -1.5 m s^{-1} at the 60-m level. MAE is very similar for all schemes at all times and levels, and fall between 1.65 and 2.15 m s^{-1} (Fig. 3.21-22). Excluding the BouLac scheme, there is little difference in wind speed bias or MAE between first-order (e.g, YSU, ACM2) or TKE-order closure (e.g, MYJ, MYNN2, BouLac, QNSE) schemes.

3.2.2 Temperature

Temperature sensors were located on the Cape Wind Tower at heights of 10 and 55 meters. ME and MAE scores by PBL scheme are in Table 3.1. MAE scores for all schemes are greater at

55 m (1.5 – 2.0 °C) than at 10 m (1.4 – 1.9 °C), with the BouLac scheme displaying the lowest values at both levels and the QNSE scheme displaying the highest values at both levels. Mean error scores are negative for all schemes at both levels, and also increased in magnitude with height. Similar to the MAE, the QNSE scheme exhibits the largest temperature biases and the BouLac scheme exhibits the lowest temperature biases.

Figure 3.23-24 show the ME by day and night for the warm and cool seasons. Negative temperature biases were found at all times and levels for each of the six PBL schemes. However, the magnitudes of the biases were greater during the warm season than the cool season and strongest at the 10-m level with values for most schemes excess of -2 °C. Comparatively, cool season ME increase from 10 m up to 55 m and range between -0.1 and -1.5 °C and are generally largest at night. Temperature MAE is also largest during the warm season, with values around 2 °C as compared to < 1.5 °C during the cool season (Fig. 3.25-26). The BouLac scheme consistently shows the smallest temperature biases and MAE than other schemes regardless of season or time of day.

3.2.3 Stability

Potential temperatures at the 10- and 55-m levels were calculated from the observed temperatures and pressures. Figure 3.27 shows composite profiles of potential temperature for all six model PBL schemes and the observations, separated by season and time of day. Large negative temperature biases are evident for both day and night as well as each season. The observations show the warm season (average 55-m minus 10-m potential temperature differences of 0.72 K and 0.70 K for day and night, respectively) to be more statically stable than the cool season (0.50 K and 0.55 K for day and night, respectively). The model PBL schemes are similar to the observed

differences; however, with the exception of the BouLac scheme during the night, all model PBL schemes are more statically stable during the warm season than the observations. Too high static stability in the lowest 60 m can inhibit mixing of higher momentum air from above with lower momentum air from below resulting in the negative wind speed biases found at the 20-m level, as well as inhibit mixing of near-surface moisture throughout the boundary layer.

During the cool season the opposite is true, in which the PBL schemes are less stable than observed. However, the model PBL schemes all depict average profiles of potential temperature decreasing with height for both the day and night, which implies super-adiabatic and absolutely unstable lapse rates. The observed profile is more neutral. The existence of super-adiabatic lapse rates suggests the presence of a superadiabatic surface layer, resulting from large sensible heat fluxes due to advection of cold air over warm water. The surface fluxes in the model may be too large, resulting in the more unstable thermal profile. During the cool season the observed wind directions at the Cape Wind tower were generally westerly to north-northeasterly (270° – 15°), which could be considered cold air advection (CAA) scenarios, either through cold continental air being advected offshore or cold marine air being advected southwestwards.

3.2.4 Wind Shear

Composite wind speed profiles for the model PBL schemes and the observations by season and diurnal period are shown in Fig. 3.28. The negative bias at the 20 m level is visible for all schemes during the warm season, with the two first-order schemes (YSU and ACM2) showing the largest negative bias. The warm season bias decreases with height up to 60 m for all but the BouLac scheme. The remaining TKE-order schemes (MYJ, MYNN2 and QNSE) show positive biases at and above the 41-m level during the warm season daytime. The wind speed biases being negative

and largest at the 20-m level during the warm season suggests too little mechanical mixing within the model as higher momentum air is not making it down to the 20-m level. This is consistent with the previously mentioned too high static stability in the models, which will inhibit such mixing and result in an increased wind shear profile. Three of the four TKE-order schemes also suggest too little mixing of lower momentum air from below with the higher momentum air at 41 m and above. The BouLac scheme behaves differently than all other schemes and shows negative biases at all levels that increase in magnitude with height during the warm season, resulting in a relaxed shear profile that suggests too little mixing of higher momentum air from above the 60-m level.

During the cool season daytime all model PBL schemes show a relaxed wind shear profile relative to the observations, with negative biases increasing in magnitude with height. This is also indicative of too much mixing within the lower MABL and consistent with the composite stability profiles that suggest over-mixing in the models. The cool season nighttime composite shear profiles show better agreement with the observations with the exception of the BouLac scheme which still exhibits the large negative biases and characteristics of under-mixing.

Figure 3.29 highlights the relationship between wind shear and static stability at the Cape Wind tower for the model PBL schemes and the tower observations. Wind shear is in the form of the ratio of the wind speed at 60 m to the wind speed at 20 m. In absolutely unstable conditions (static stability less than zero) the models and observations show a constant wind speed ratio between 1.02 and 1.06 which agrees well with the value of 1.04 shown by Shimada et al. (2011) at the FINO1 tower in the North Sea. In the stable regime approximated by static stability values greater than 1 K the models and observations show fair agreement, with the exception of the BouLac scheme which is suffering from the relaxed shear profile resulting from too little downward mechanical mixing. In the neutral to slightly stable stability regimes, approximated by

static stability values between 0 K and 0.5 K, the model PBL schemes all show far higher wind shear values than the observations. This implies that the mixing problem in the model occurs mostly in neutral to slightly stable regimes.

3.3 NARR Composites

In an effort to determine what synoptic flow regimes are most contributing to the negative wind speed biases at the Cape Wind tower, NARR composites of several variables were constructed for negative error cases. A negative error case was defined as any NARR analysis time (00z, 03z, 06z, etc.) where the wind speed errors at each level exceed -0.5 standard deviations for the entire 3-hour period centered on that time. If 4 of the 6 PBL schemes met those conditions at a single analysis time, that time was considered to be a negative error case. Thirty-two NARR analysis times were singled out using this method, 14 during the cool season and 18 during the warm season.

The NARR composites of various fields are shown in Fig. 3.30. The flow regime shown in the composites is dominated by a high pressure system centered over the Tennessee and Lower Mississippi valleys with a trough offshore the NEUS resulting in north-northwesterly flow across the southern New England region at the surface that becomes more northwesterly and then westerly with height (1000 – 850 hPa). The result is cold air advection across Nantucket Sound which is likely contributing to the models creating unstable surface layers during the cool season. Too little mechanical mixing in the models from above fails to remove the super-adiabatic lapse rates and ultimately results in negative wind speed biases that increase in magnitude with height throughout the lowest 60 m. During the warm season nighttime, the same flow regime can result in warm, stable air being advected over Nantucket Sound. The PBL schemes are tending to overdo

the stability, leading to too little mixing of higher momentum from above and large negative wind speed biases at the lower levels.

Table 3.1. Mean error and mean absolute error for each of the six WRF PBL schemes for wind speed at the 20-, 41- and 60-m levels, as well as temperature at the 10- and 55-m levels.

Cape Wind Meteorological Mast Mean Error and Mean Absolute Error

	YSU		ACM2		MYJ		MYNN2		BouLac		QNSE	
	ME	MAE	ME	MAE	ME	MAE	ME	MAE	ME	MAE	ME	MAE
WSP60	-0.26	1.95	-0.33	1.85	-0.19	1.91	-0.27	1.96	-0.91	1.94	-0.14	2.02
WSP41	-0.33	1.85	-0.32	1.77	-0.25	1.84	-0.20	1.89	-0.72	1.84	-0.22	1.92
WSP20	-0.44	1.77	-0.34	1.72	-0.45	1.78	-0.30	1.82	-0.55	1.80	-0.38	1.85
TMP55	-1.57	1.75	-1.51	1.70	-1.64	1.75	-1.49	1.68	-1.24	1.50	-1.93	2.00
TMP10	-1.36	1.61	-1.27	1.55	-1.59	1.68	-1.35	1.60	-0.93	1.39	-1.79	1.88

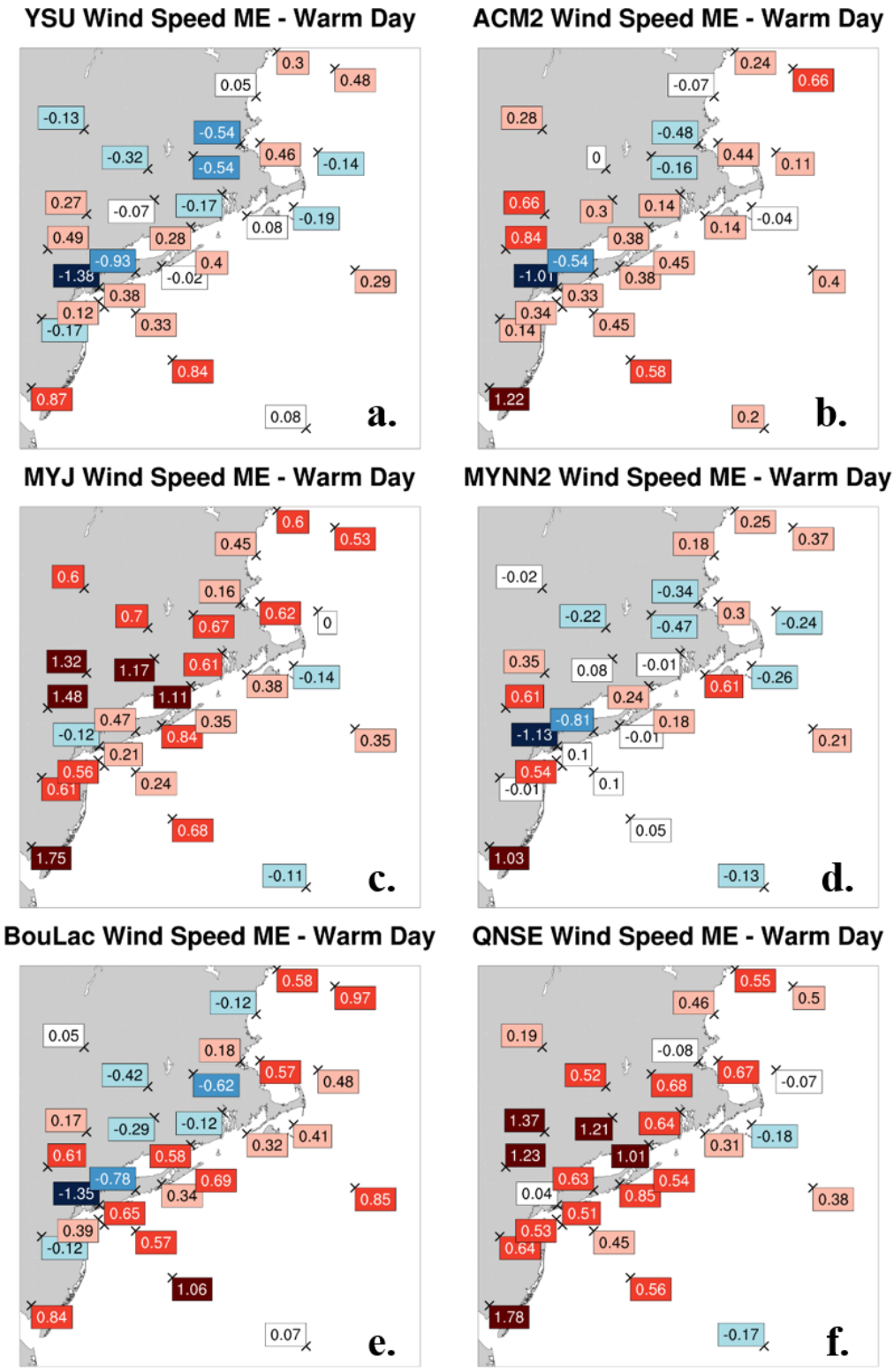

Figure 3.2. Wind speed mean error in m s^{-1} at each of the buoy, C-MAN and ASOS stations for the warm season (April - September) during the daytime (1200 - 2300 UTC) for the (a) YSU, (b) ACM2, (c) MYJ, (d) MYNN2, (e) BouLac, and (f) QNSE schemes.

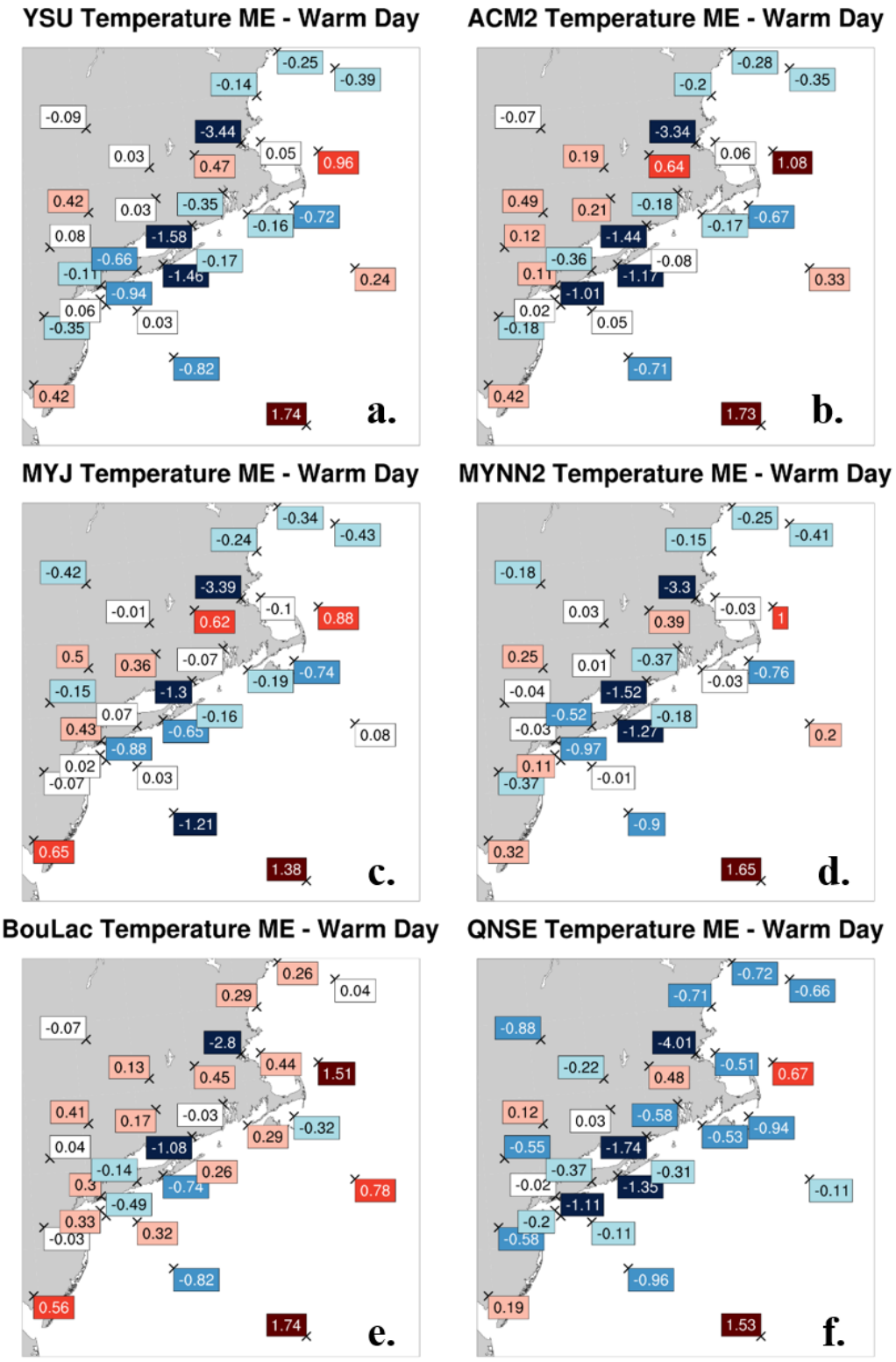

Figure 3.2. As in Fig. 3.1, but for temperature (°C).

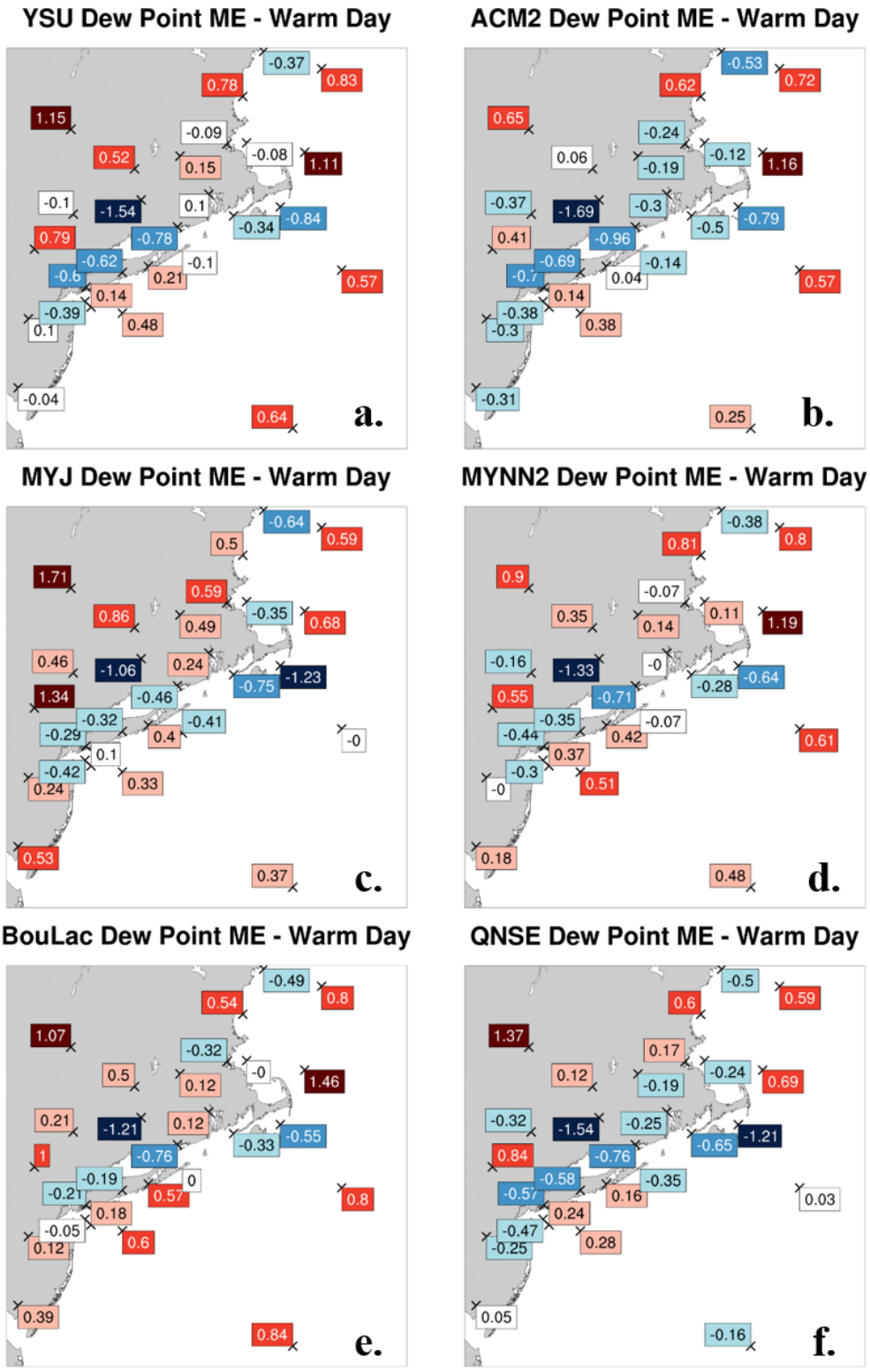

Figure 3.3. As in Fig. 3.1, but for dew point temperature (°C).

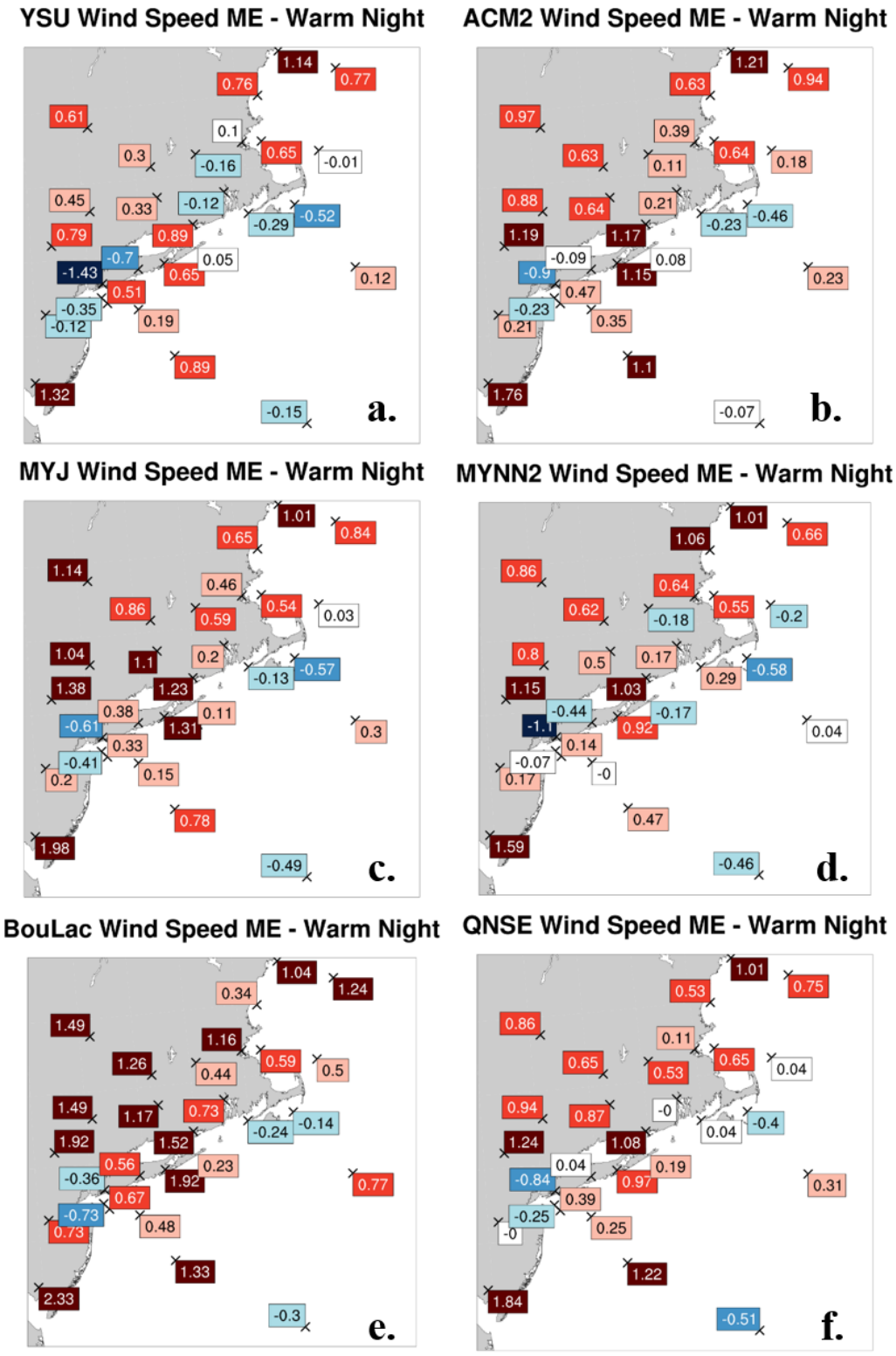

Figure 3.4. As in Fig. 3.1, but for the warm season (April - September) nighttime (0000 - 1100 UTC).

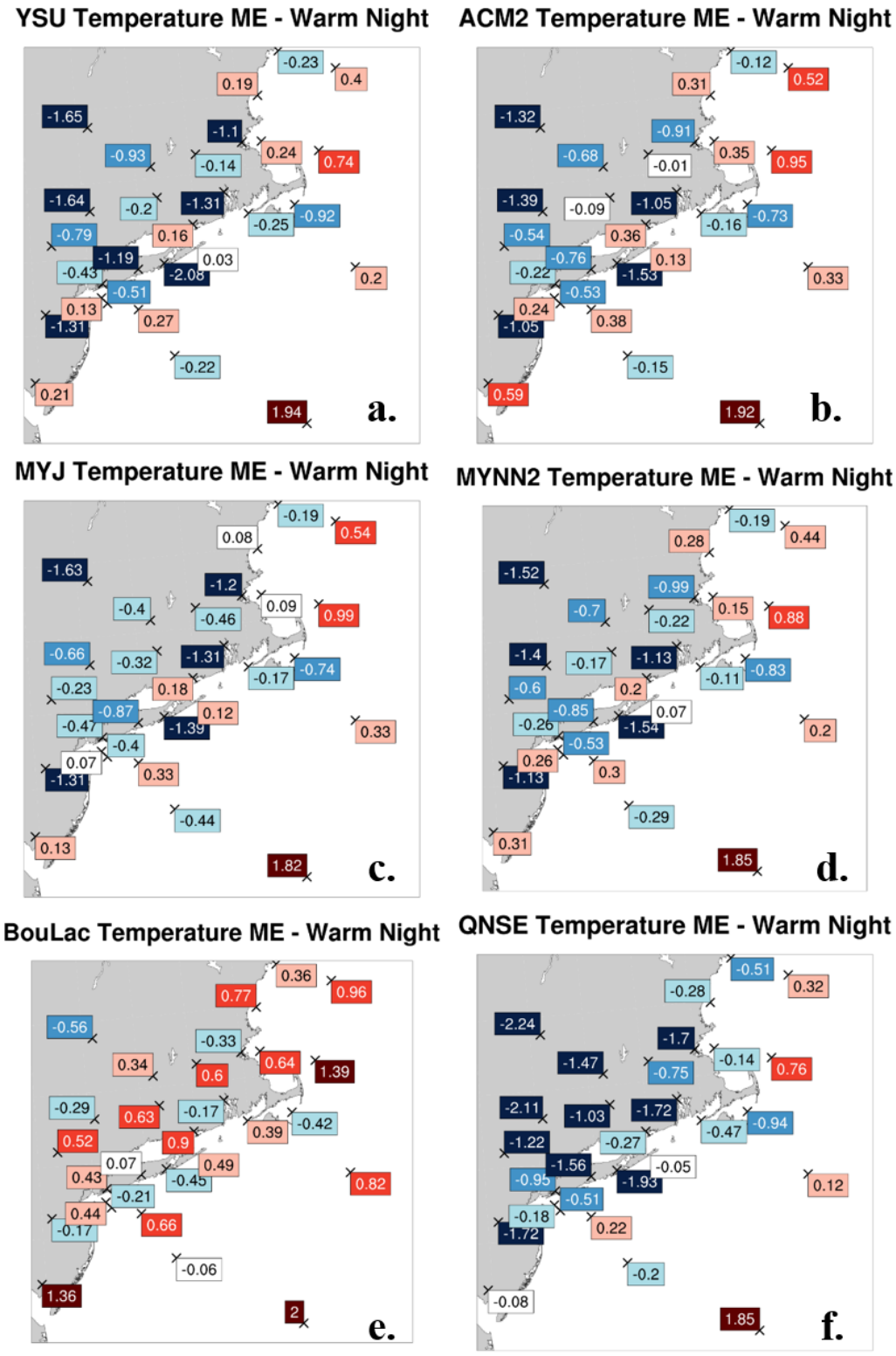

Figure 3.5. As in Fig. 3.2, but for the warm season (April - September) nighttime (0000 - 1100 UTC).

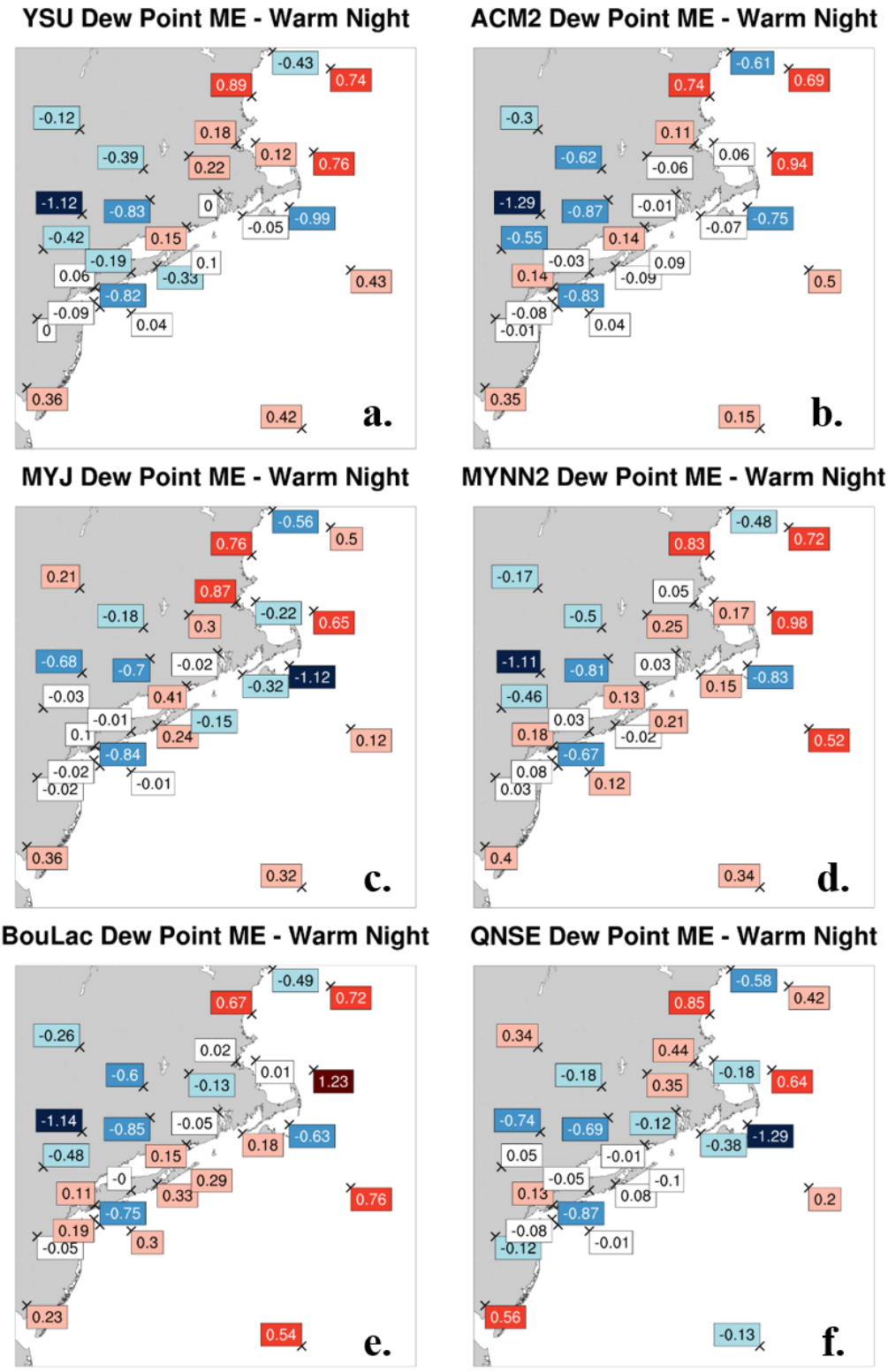

Figure 3.6. As in Fig. 3.3, but for the warm season (April - September) nighttime (0000 - 1100 UTC).

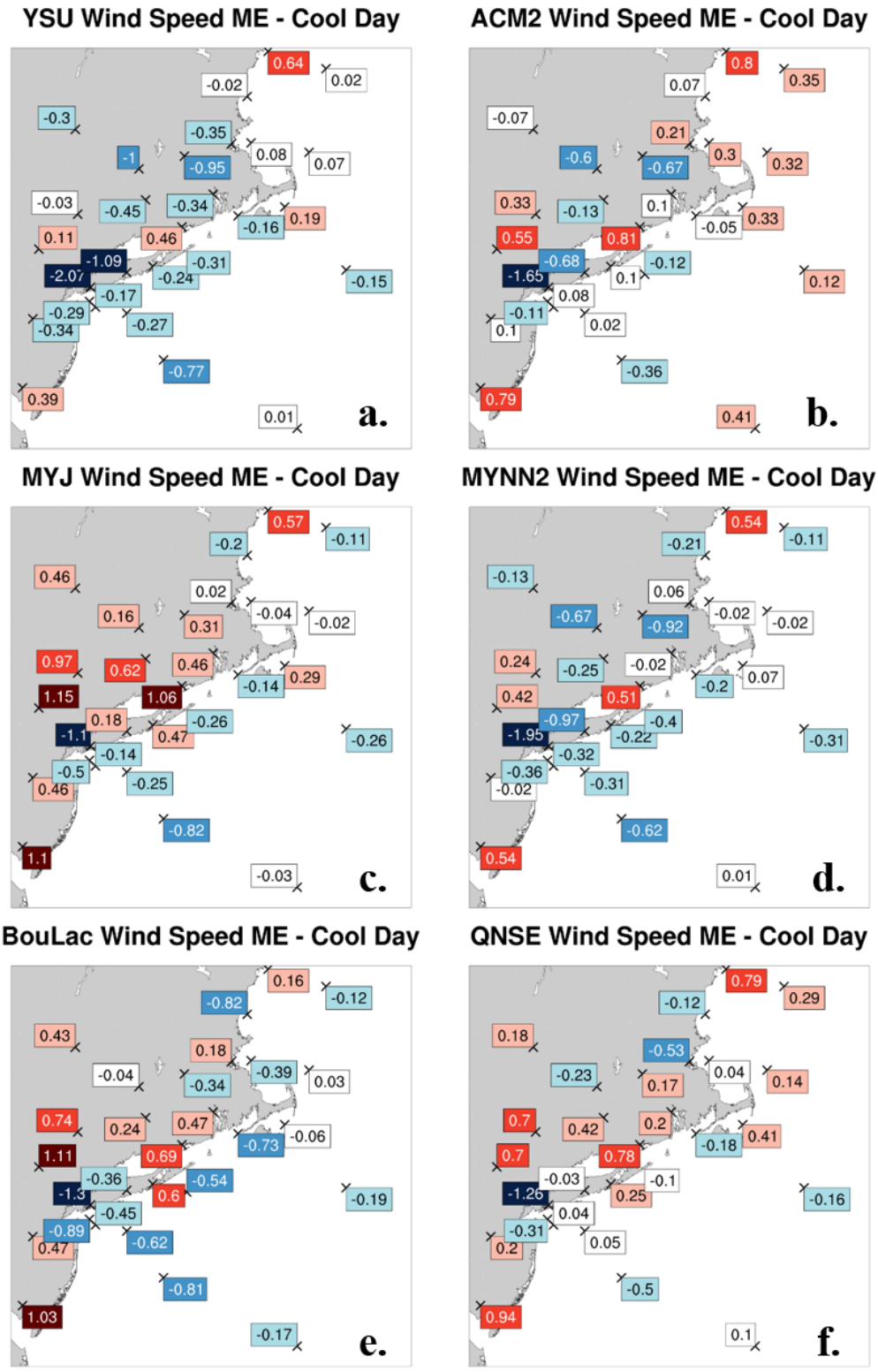

Figure 3.7. As in Fig. 3.1, but for the cool season (October - March) daytime (1200 - 2300 UTC).

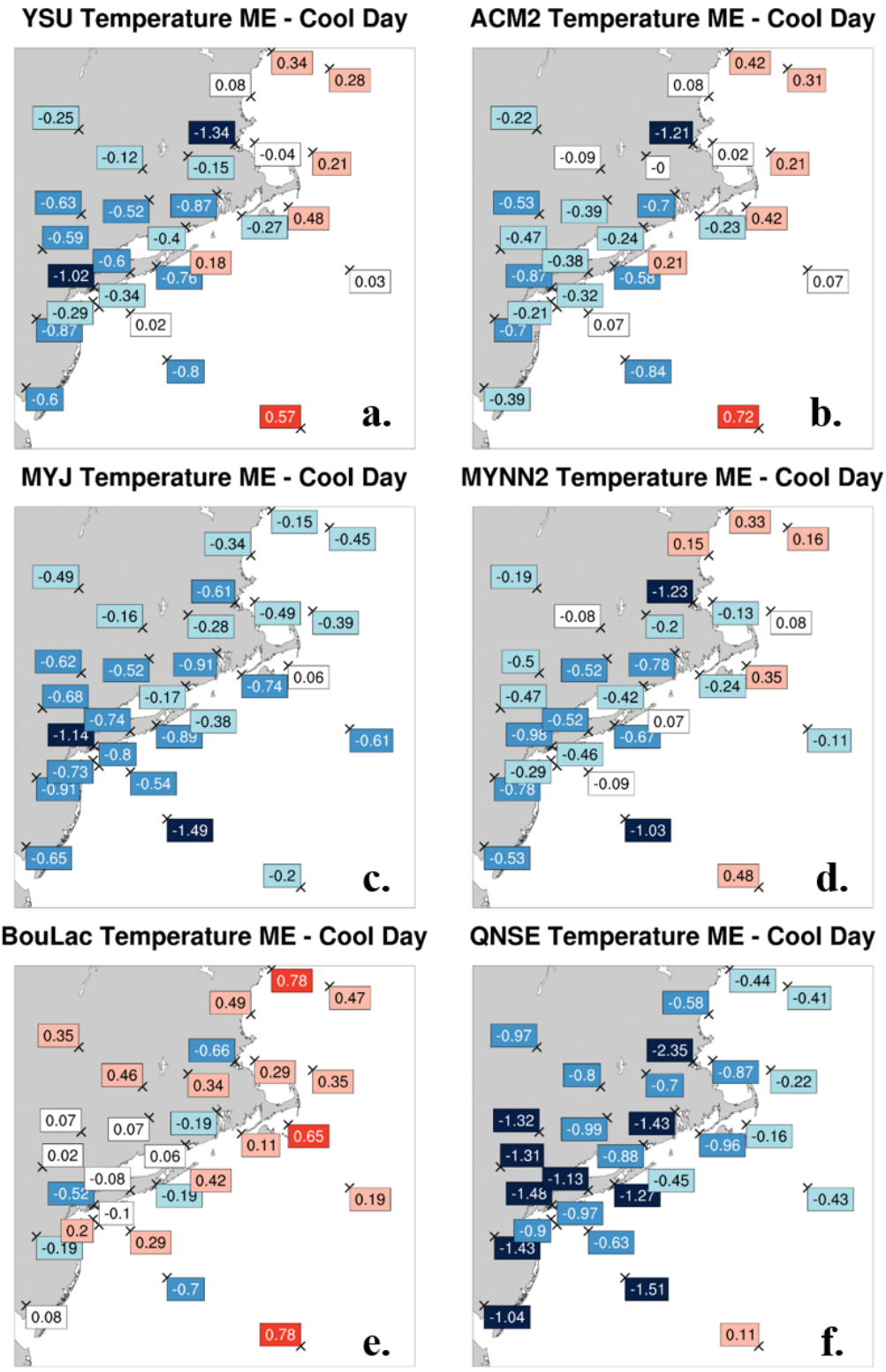

Figure 3.8. As in Fig. 3.2, but for the cool season (October - March) daytime (1200 - 2300 UTC).

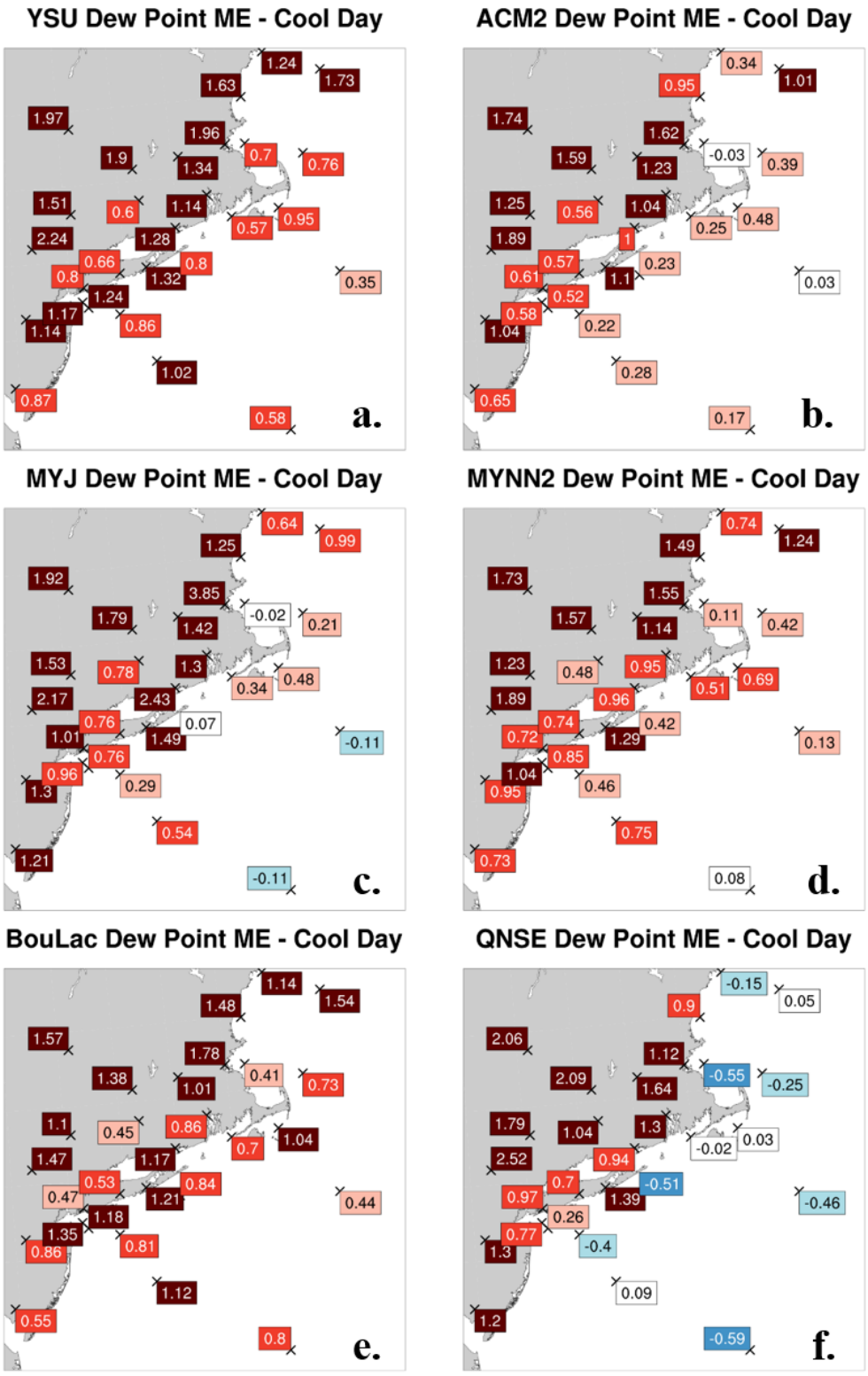

Figure 3.9. As in Fig. 3.3, but for the cool season (October - March) daytime (1200 - 2300 UTC).

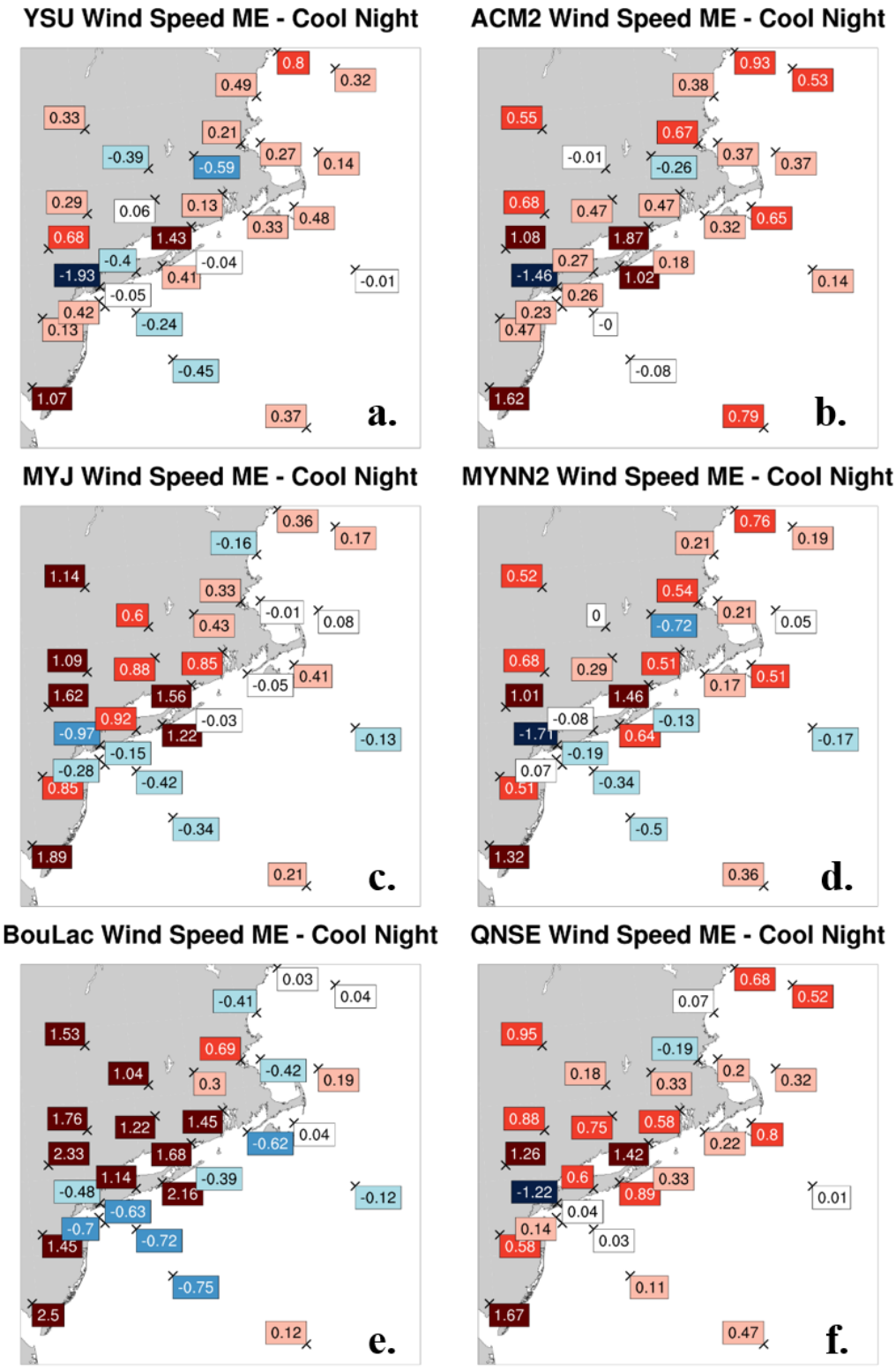

Figure 3.10. As in Fig. 3.1, but for the cool season (October - March) nighttime (0000 - 1100 UTC).

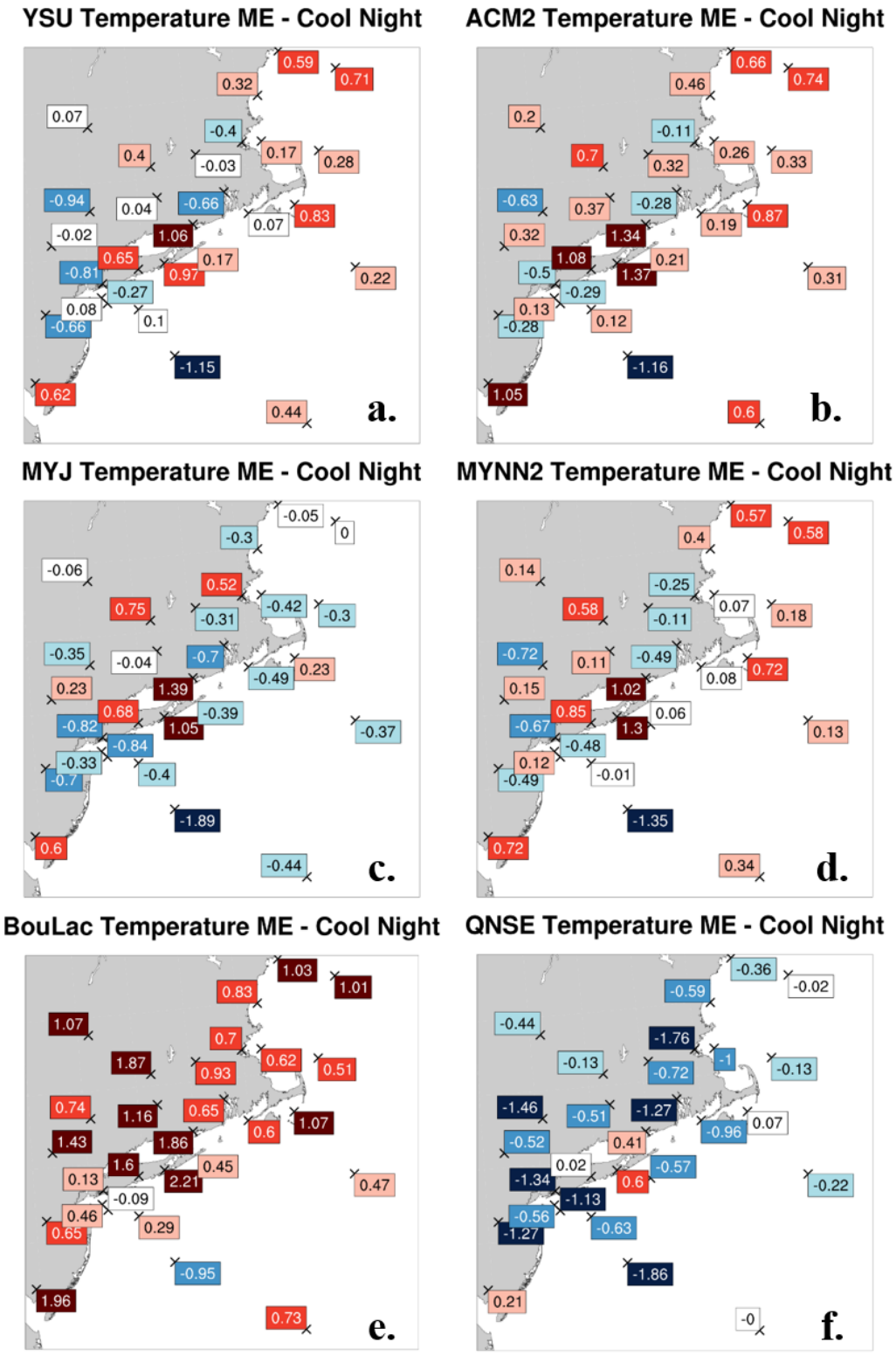

Figure 3.11. As in Fig. 3.2, but for the cool season (October - March) nighttime (0000 - 1100 UTC).

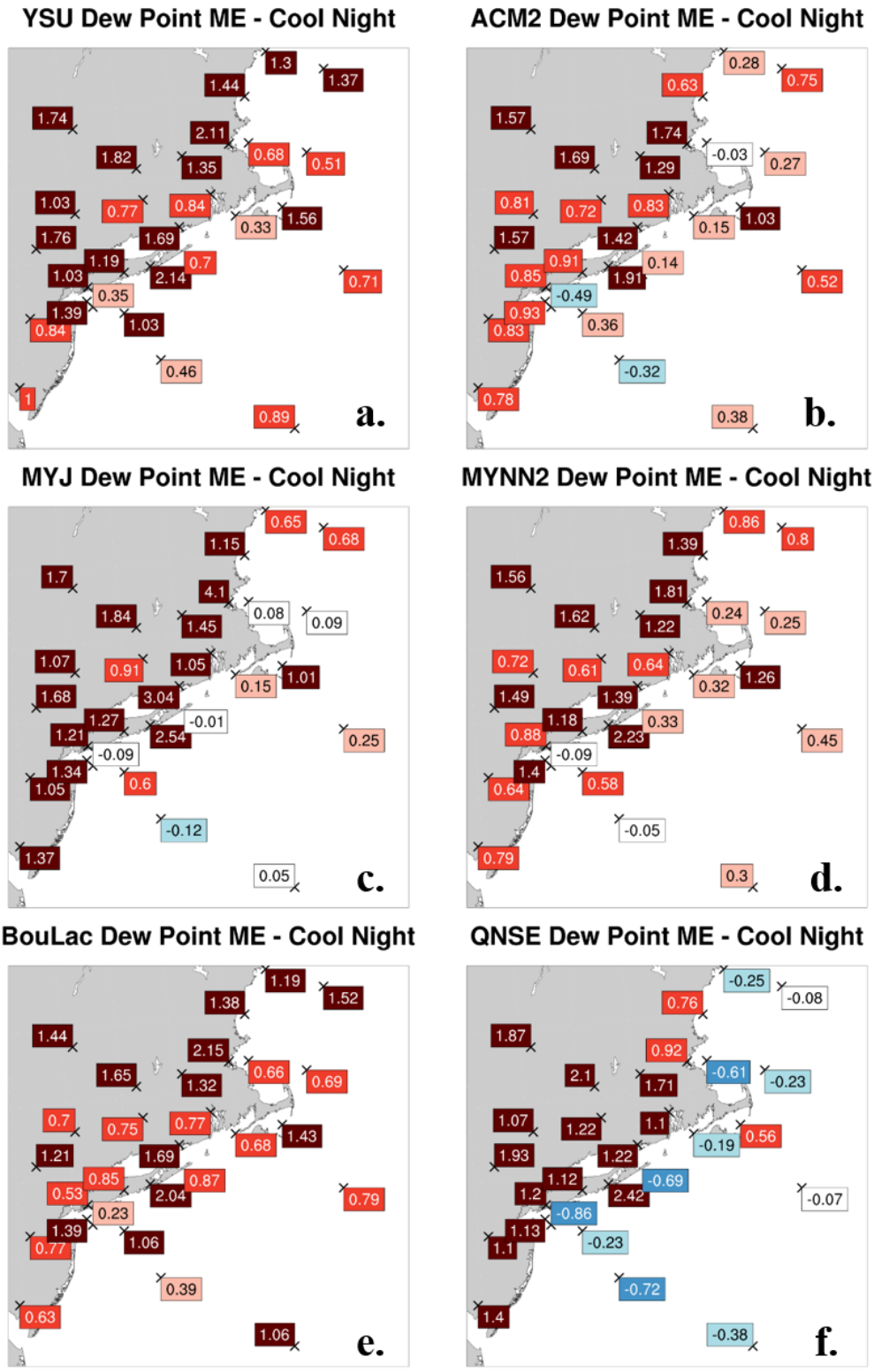

Figure 3.12. As in Fig. 3.3, but for the cool season (October - March) nighttime (0000 - 1100 UTC).

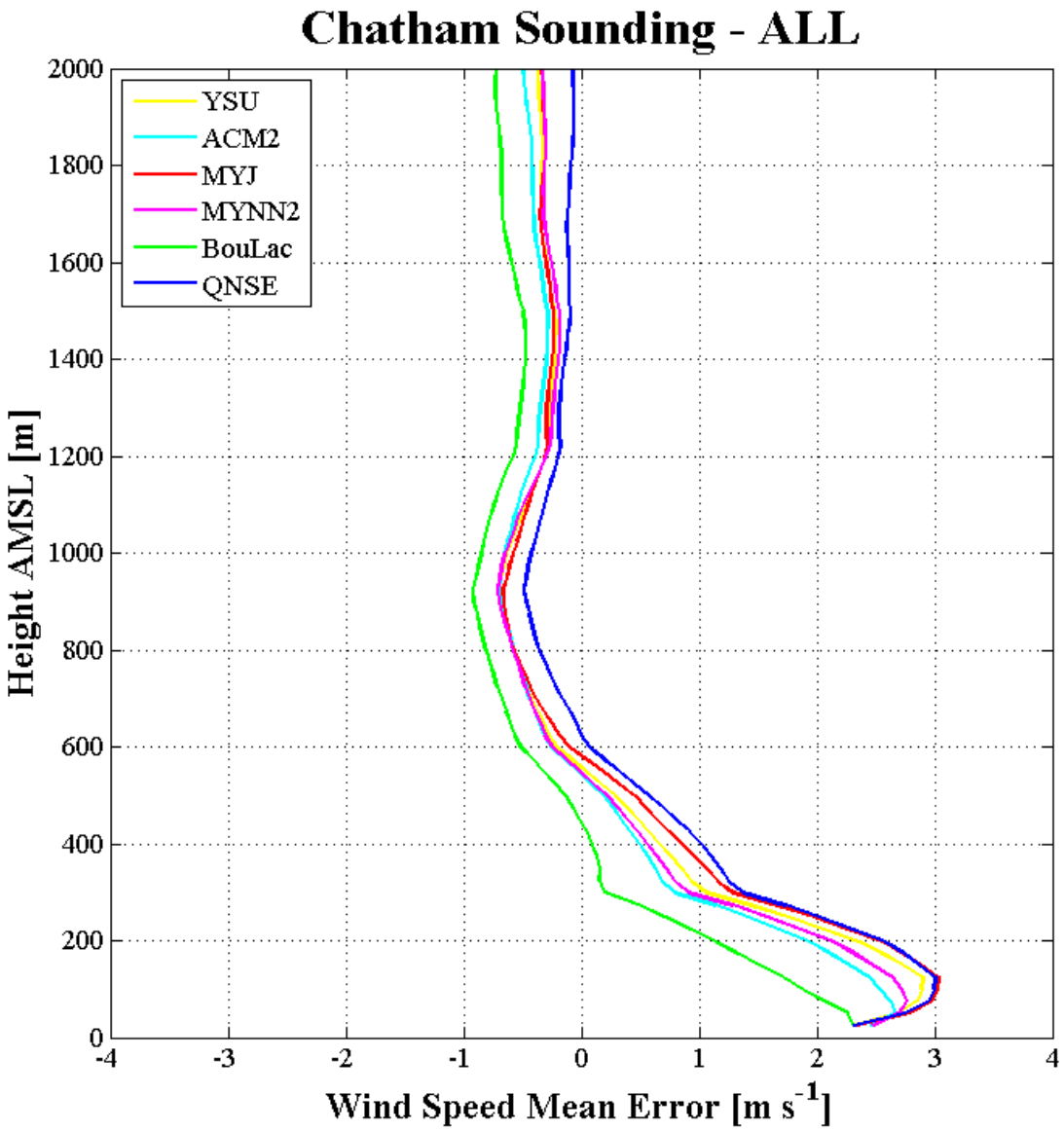

Figure 3.13. Wind speed mean error in m s-1 for each of the six WRF PBL schemes for CHH soundings. Wind speed mean error values were bin-averaged to every 25 m. Mean errors include all available soundings.

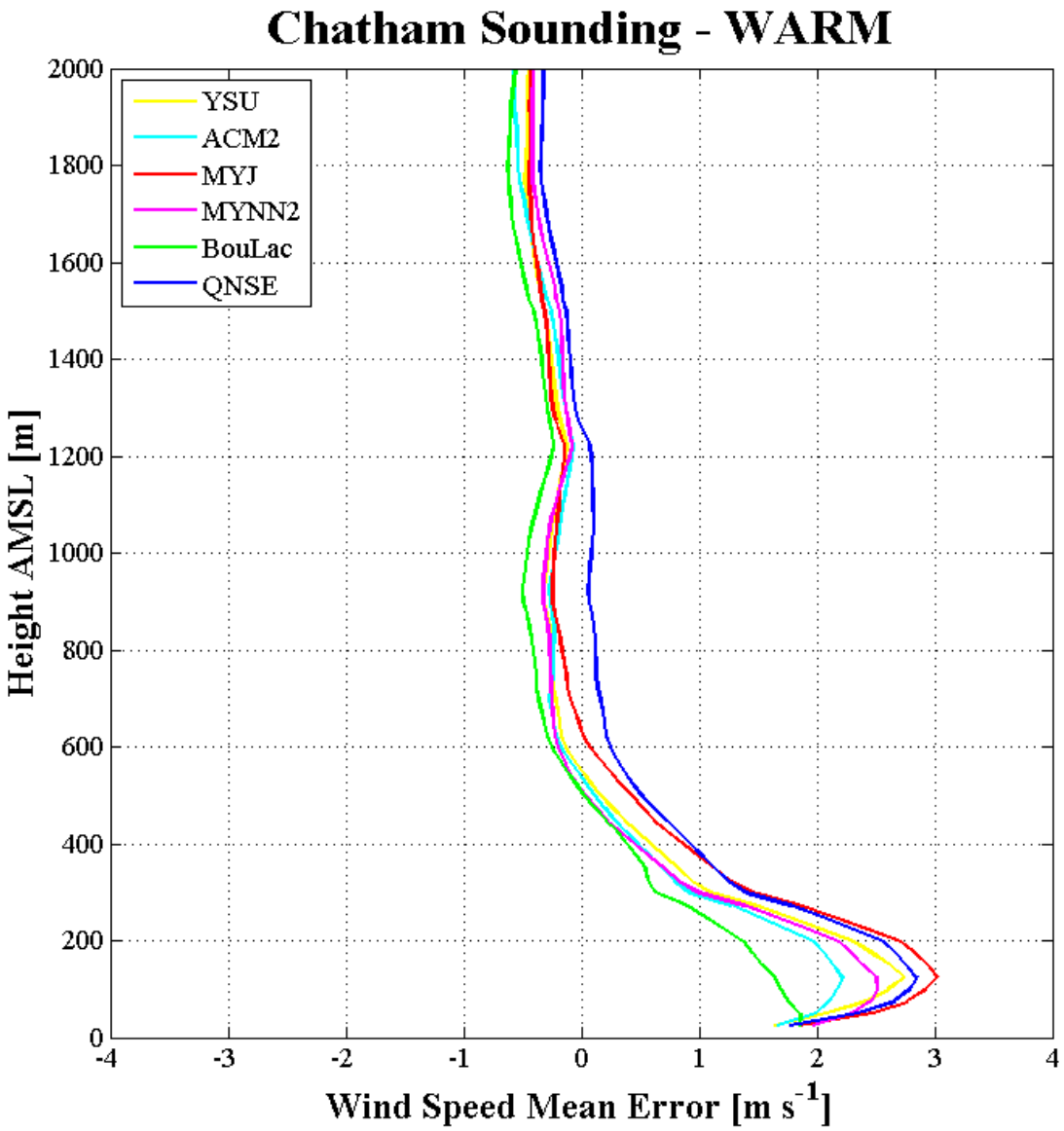

Figure 3.14. As in Fig. 3.13 but for the warm season (April to September) only.

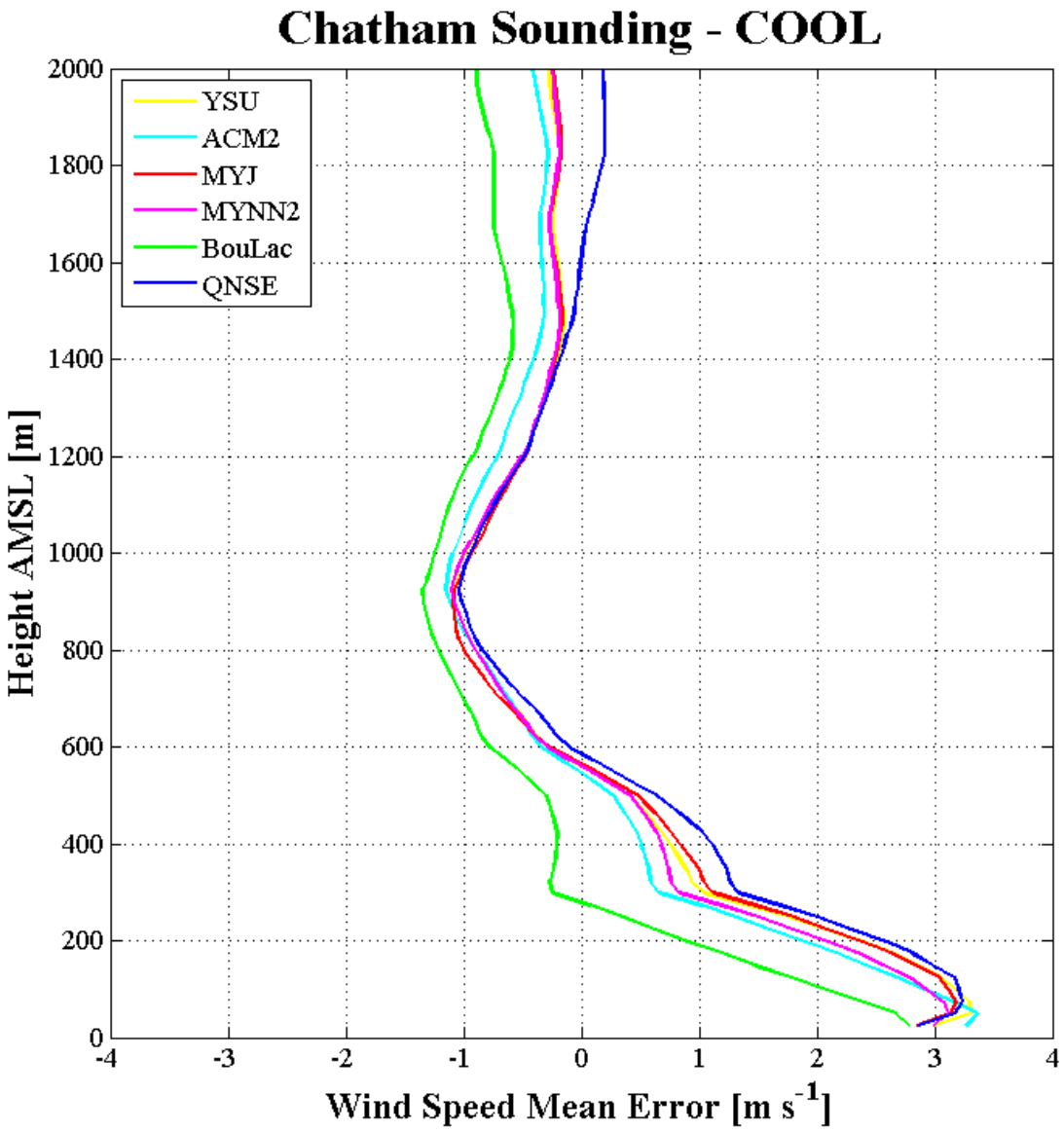

Figure 3.15. As in Fig. 3.13 but for the cool season (October to March) only.

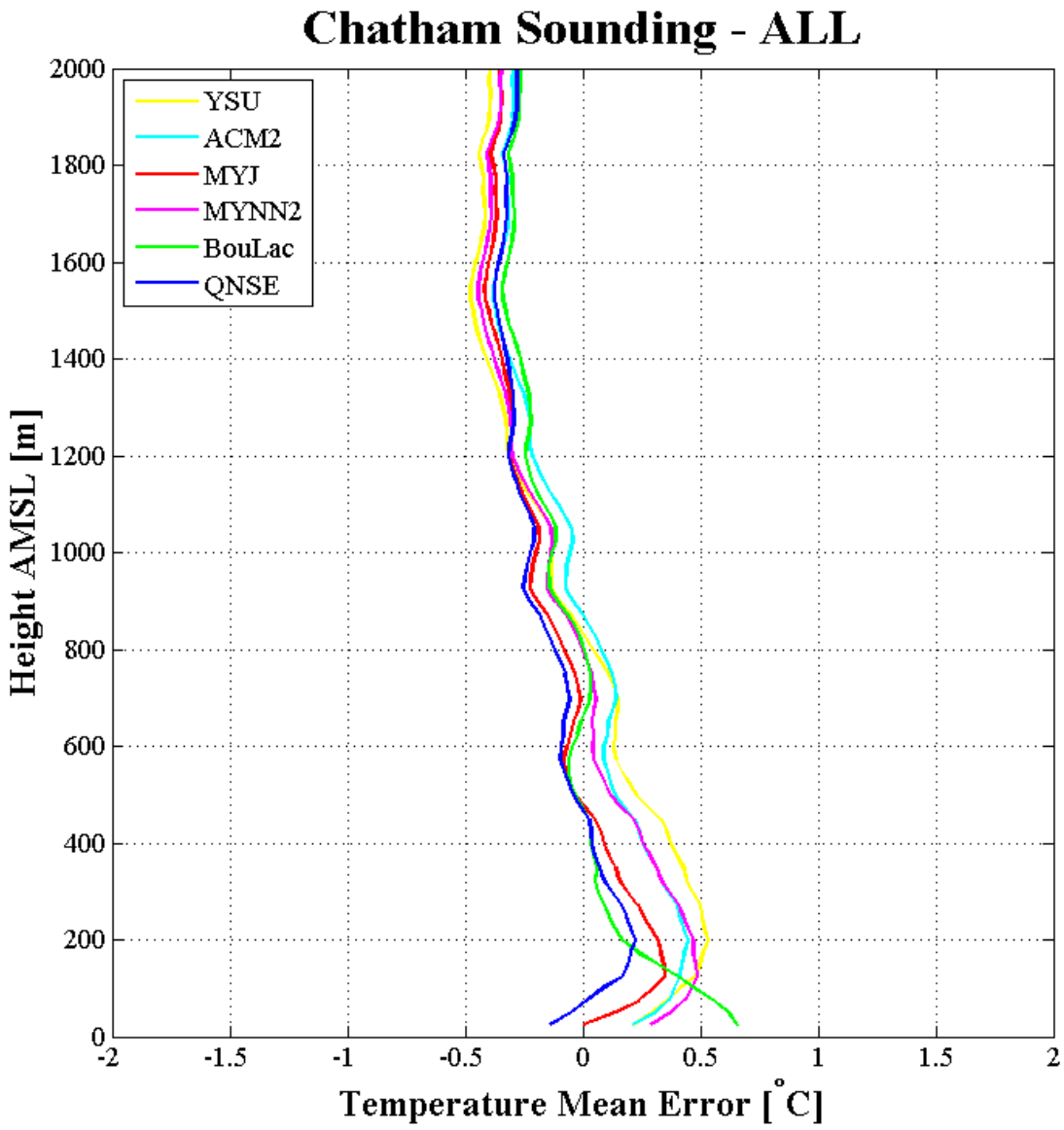

Figure 3.16. Temperature mean error in degrees Celsius for each of the six WRF PBL schemes for CHH soundings. Temperature mean error values were bin-averaged to every 25 m. Mean errors include all available soundings.

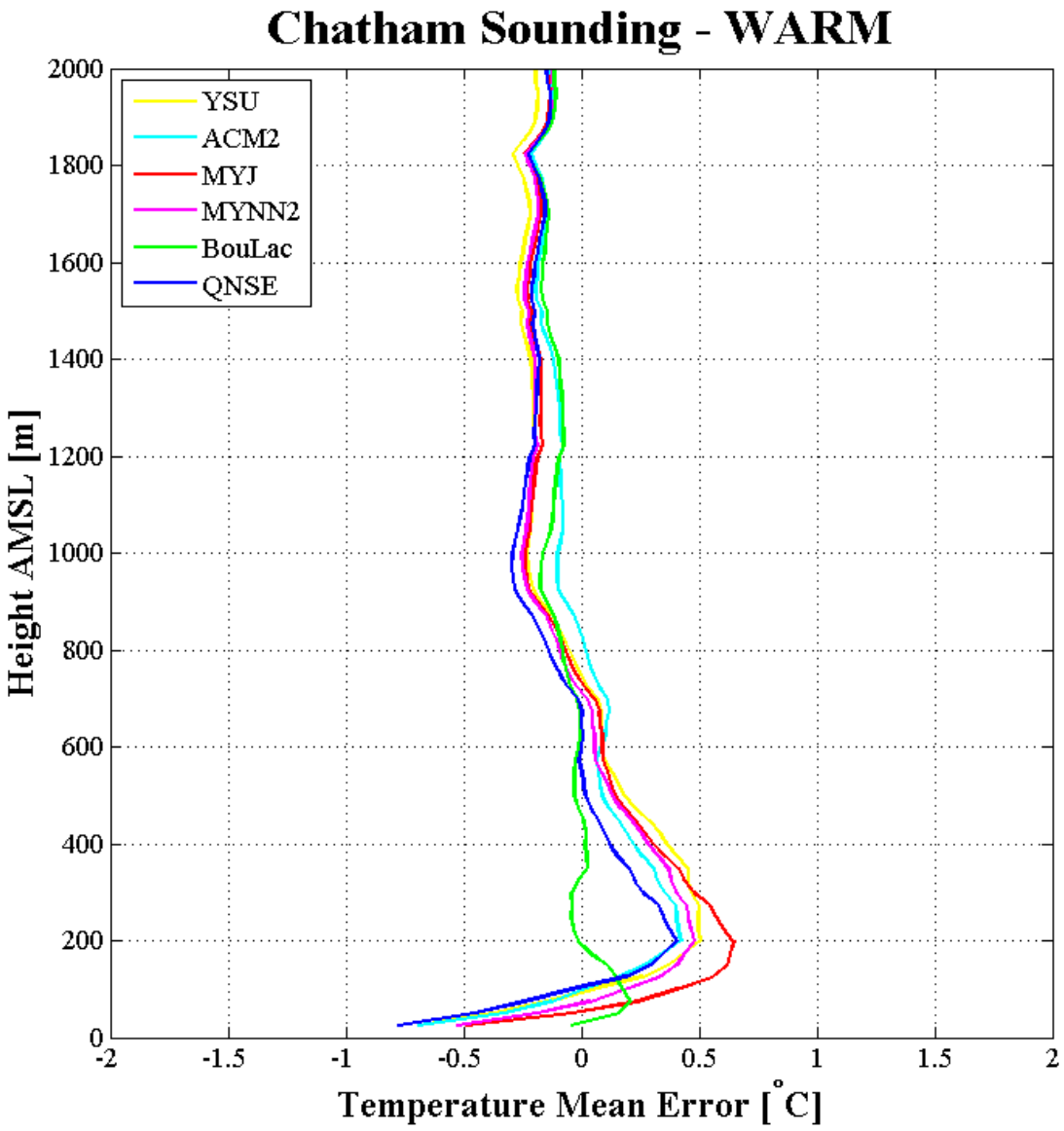

Figure 3.17. As in Fig. 3.16, but for the warm season (April to September) only.

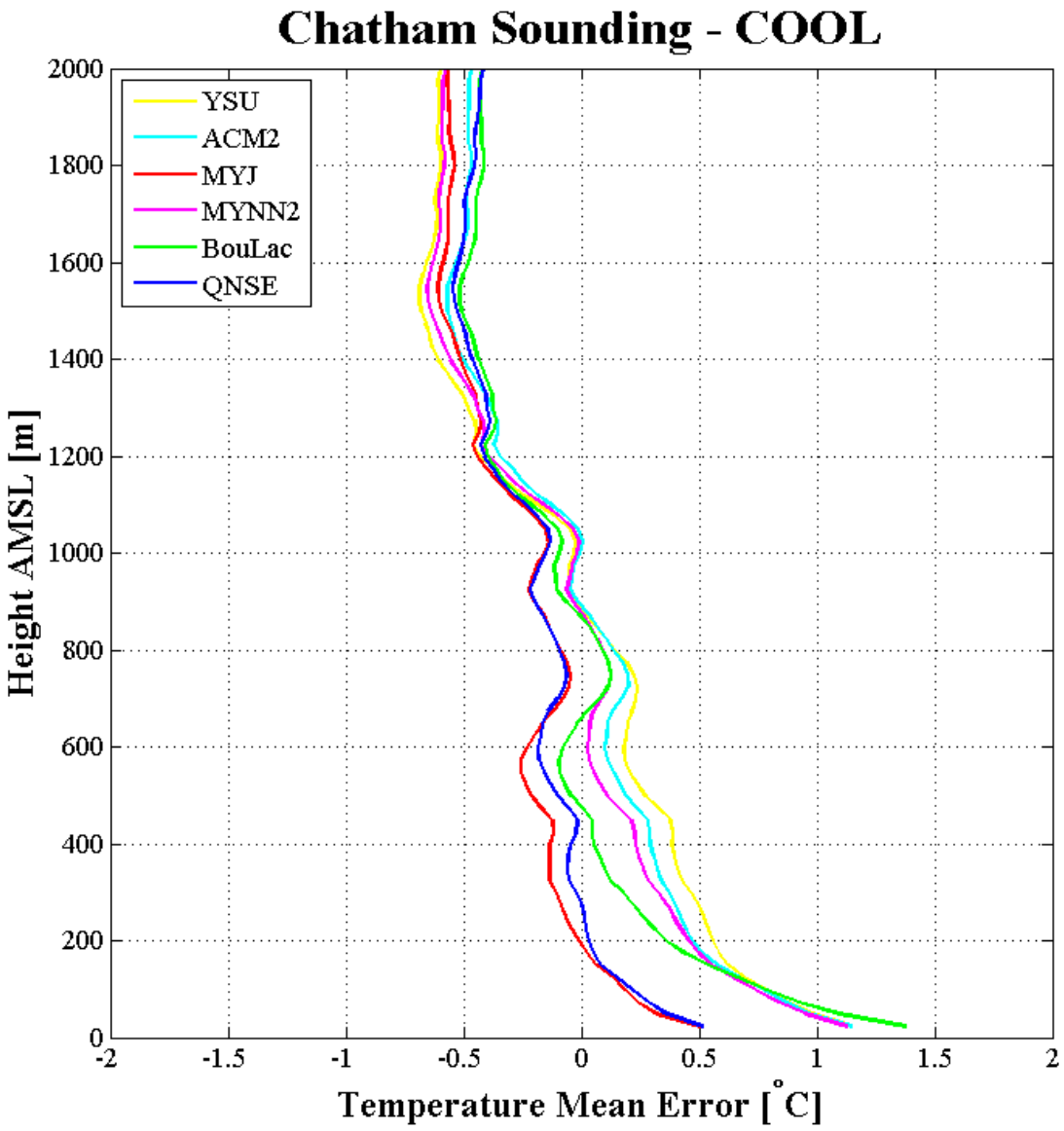

Figure 3.18. As in Fig. 3.16, but for the cool season (October to March) only.

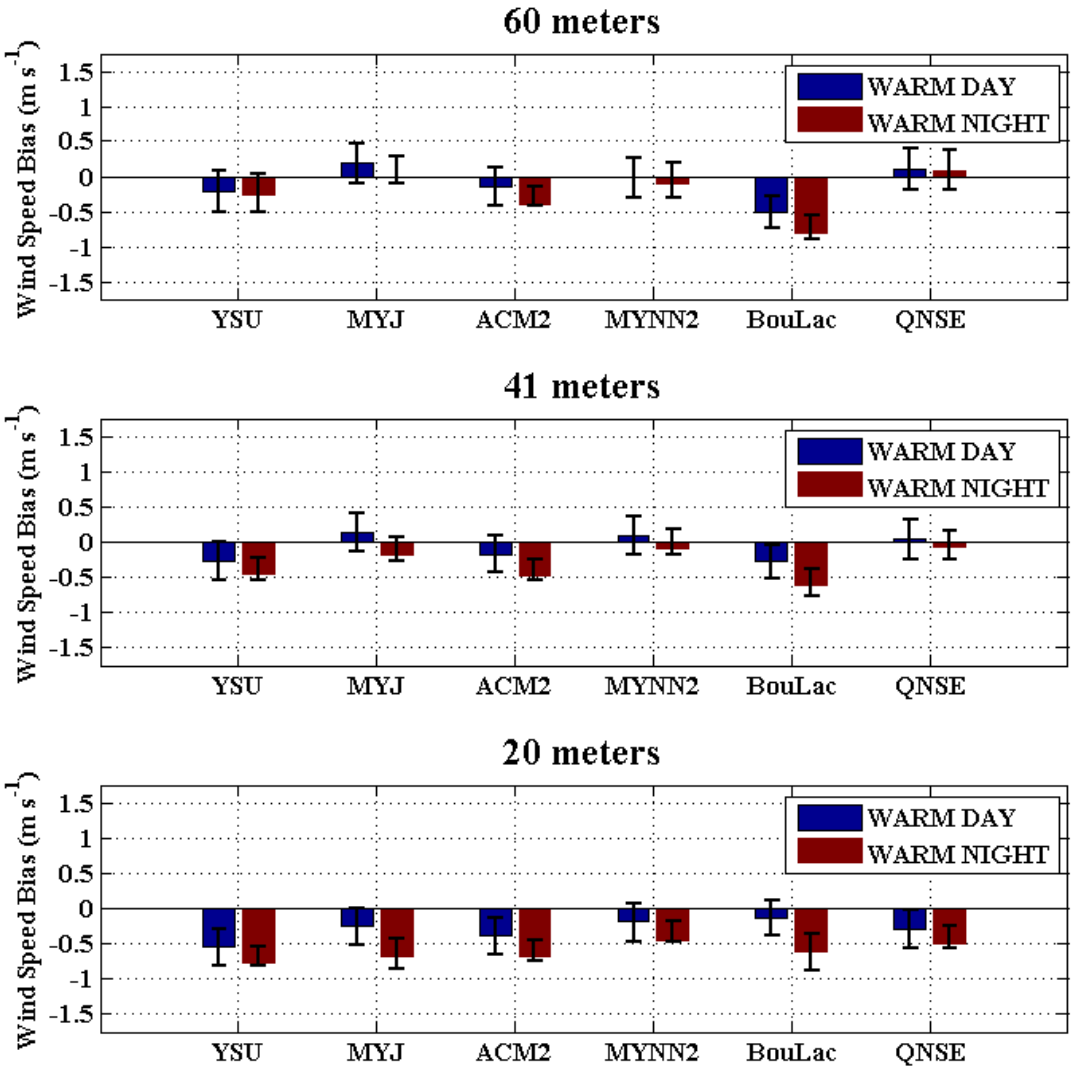

Figure 3.19. Warm season (April to September) wind speed mean error in m s^{-1} for each of the six WRF PBL schemes at (a) 60 m, (b) 41 m and (c) 20 m. Daytime (1200 UTC to 2300 UTC) is in blue and nighttime (0000 UTC to 1100 UTC) is in red. Black bars represent the bootstrap 95% confidence intervals.

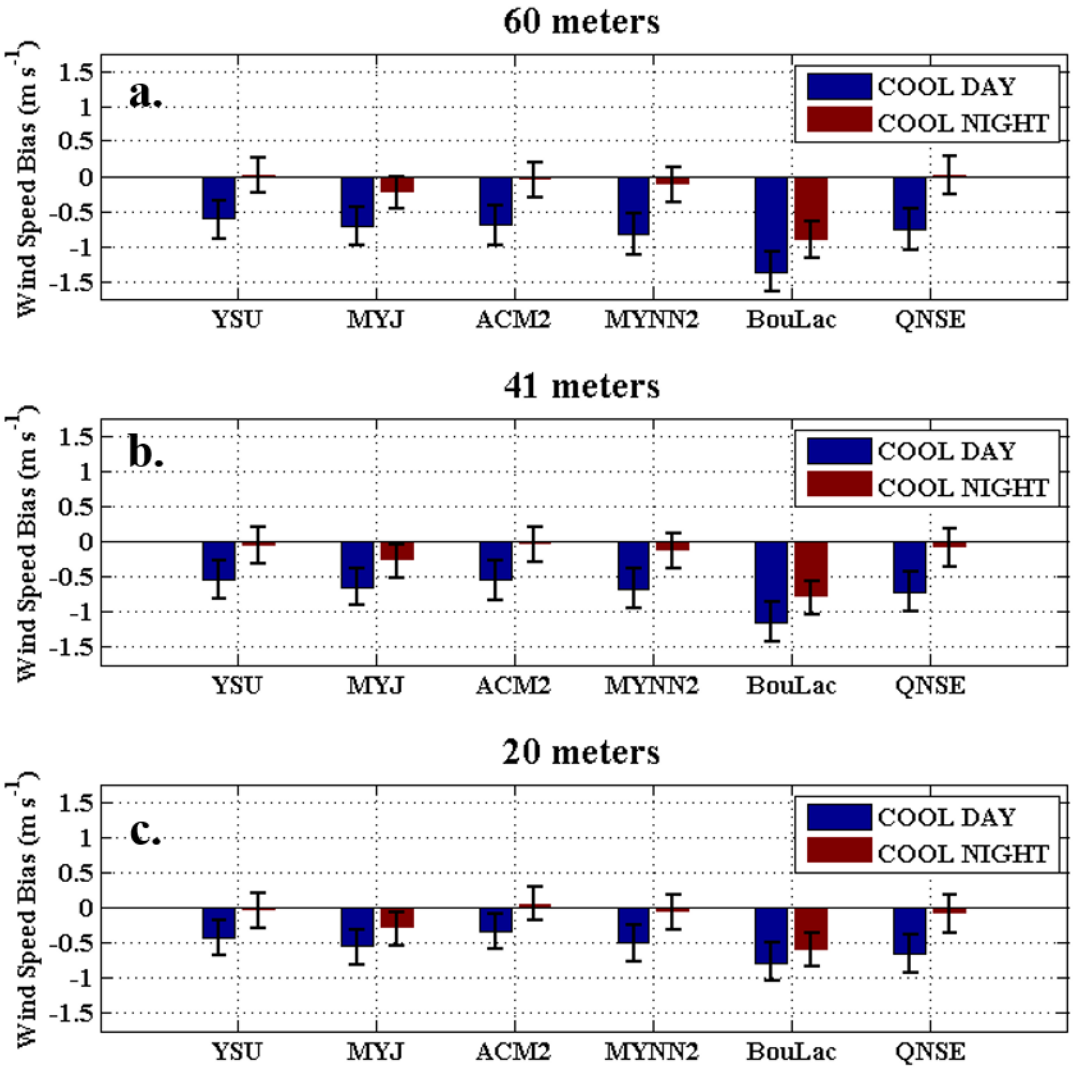

Figure 3.20. As in Fig. 3.19, but for the cool season (October to March).

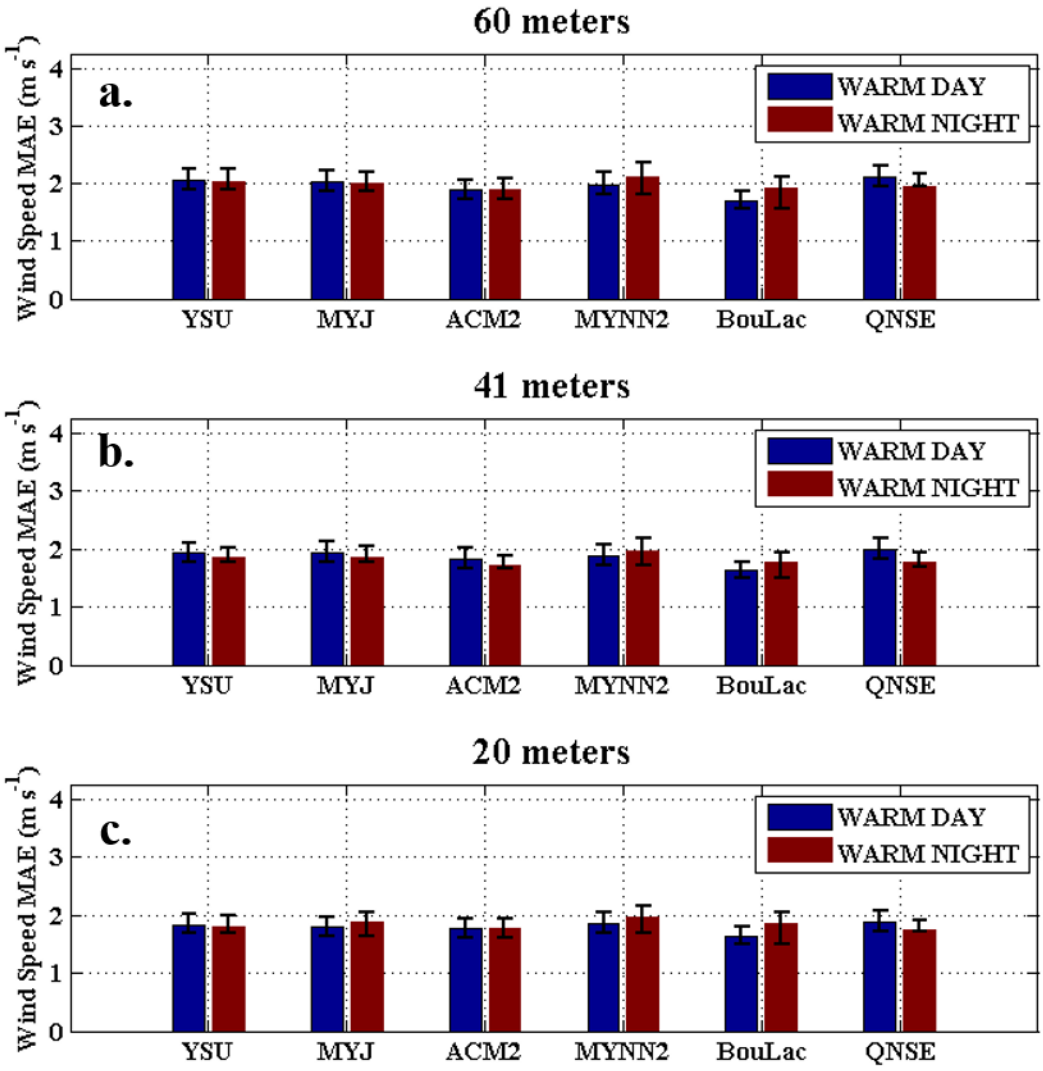

Figure 3.21. As in Fig. 3.19, but for mean absolute error in m s^{-1}.

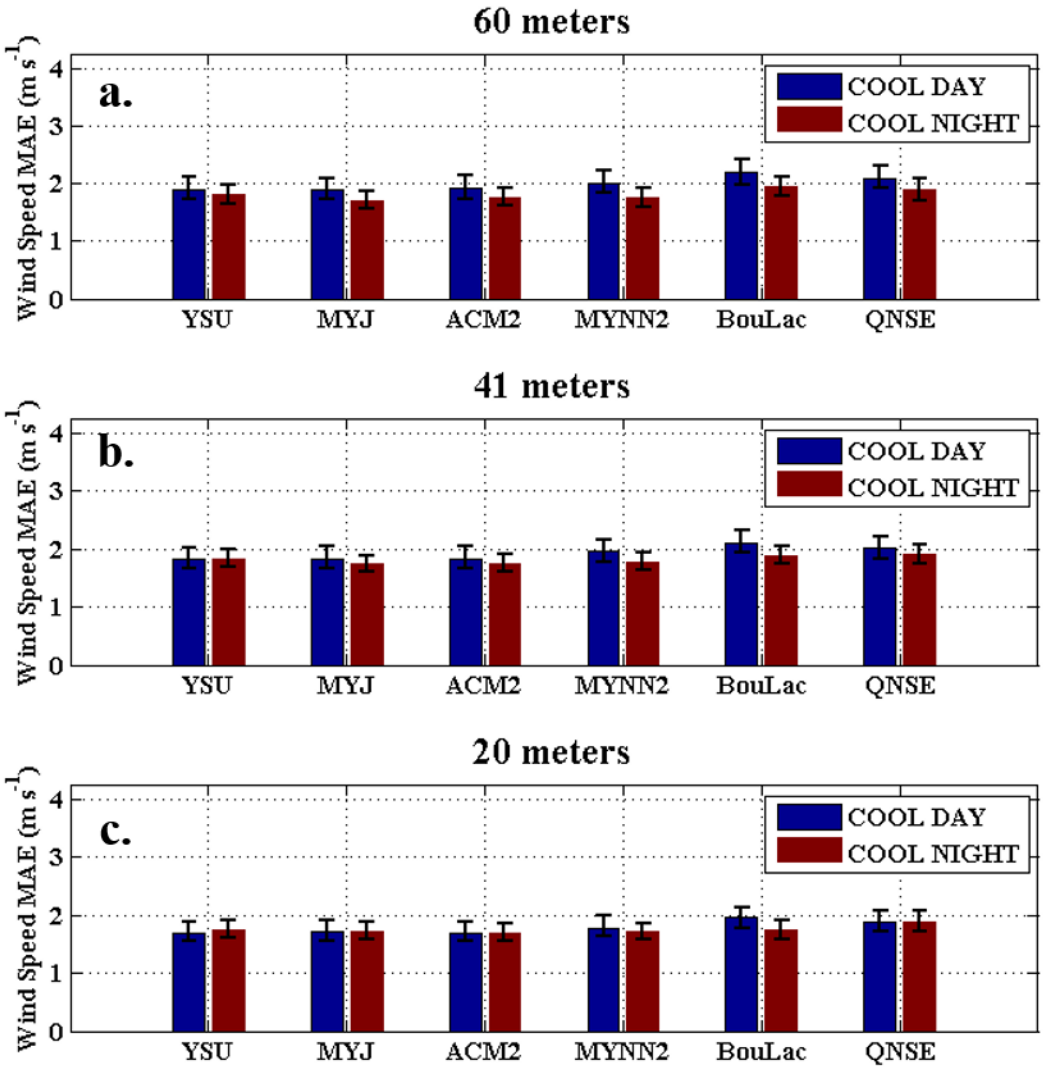

Figure 3.22. As in Fig. 3.21, but for the cool season (October to March).

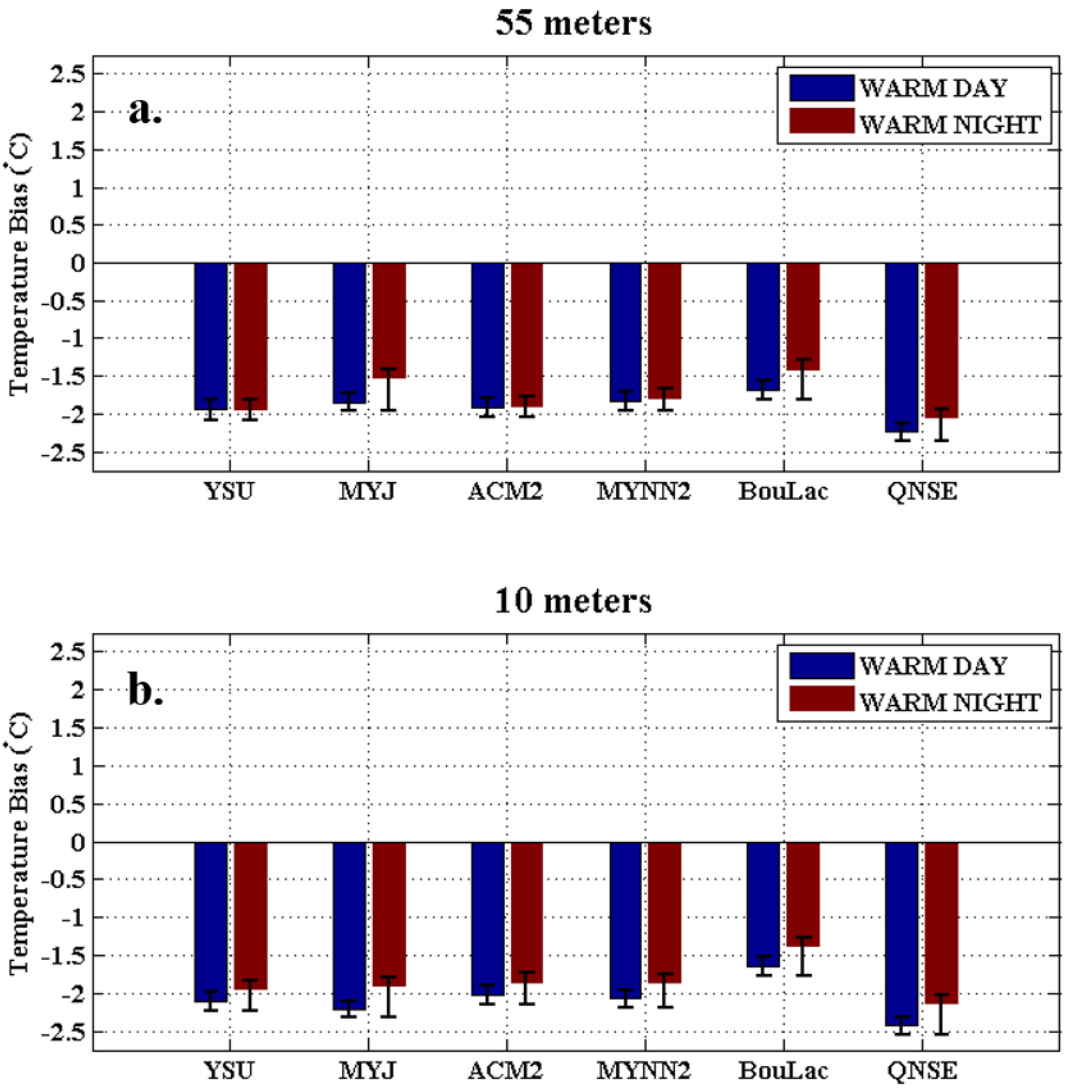

Figure 3.23. Warm season (April to September) temperature mean error in degrees Celsius for each of the WRF PBL schemes at (a) 55 m and (b) 10 m. Daytime (1200 UTC to 2300 UTC) is in blue and nighttime (0000 UTC to 1100 UTC) is in red. Black bars represent the bootstrap 95% confidence intervals.

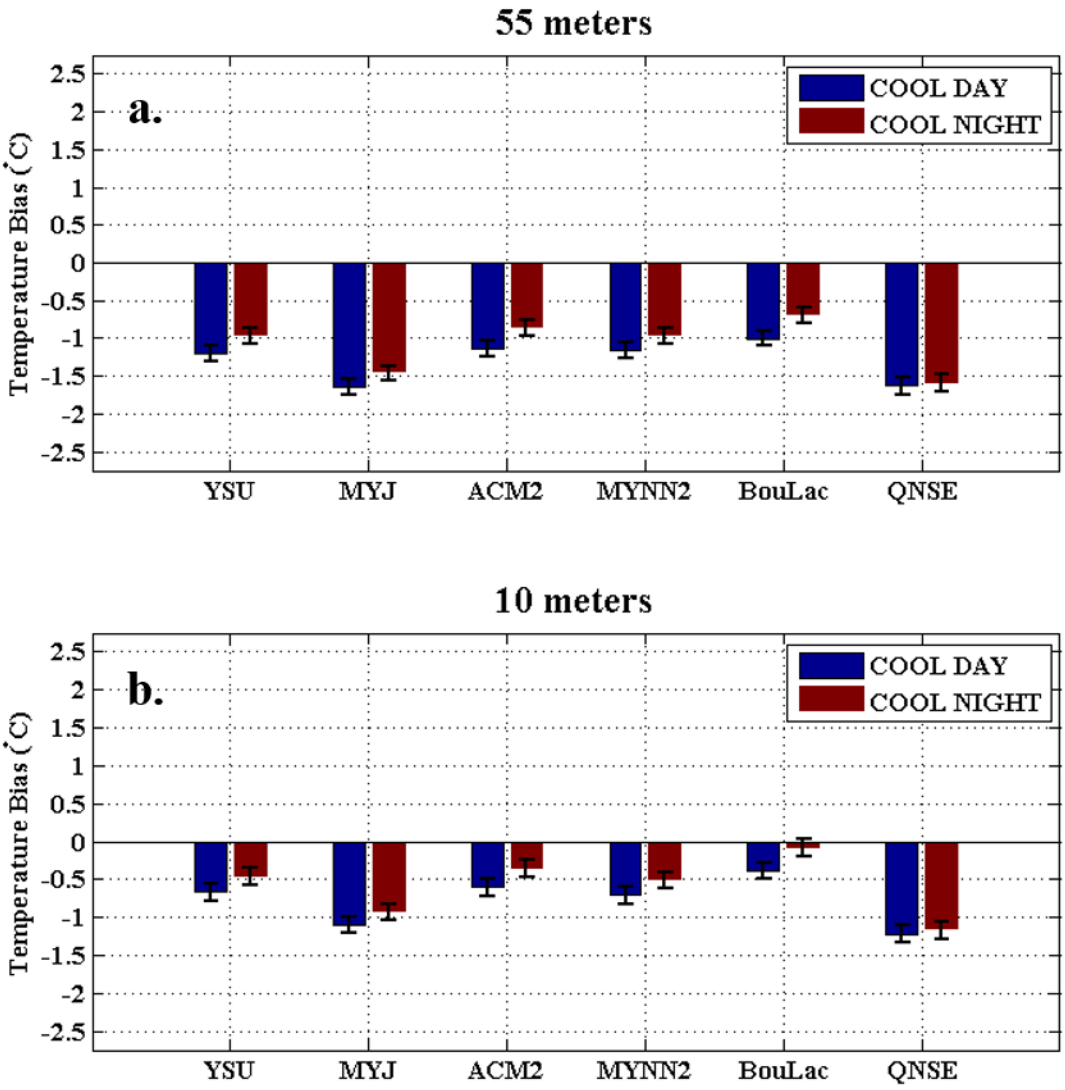

Figure3.24. As in Fig. 3.23, but for the cool season (October to March).

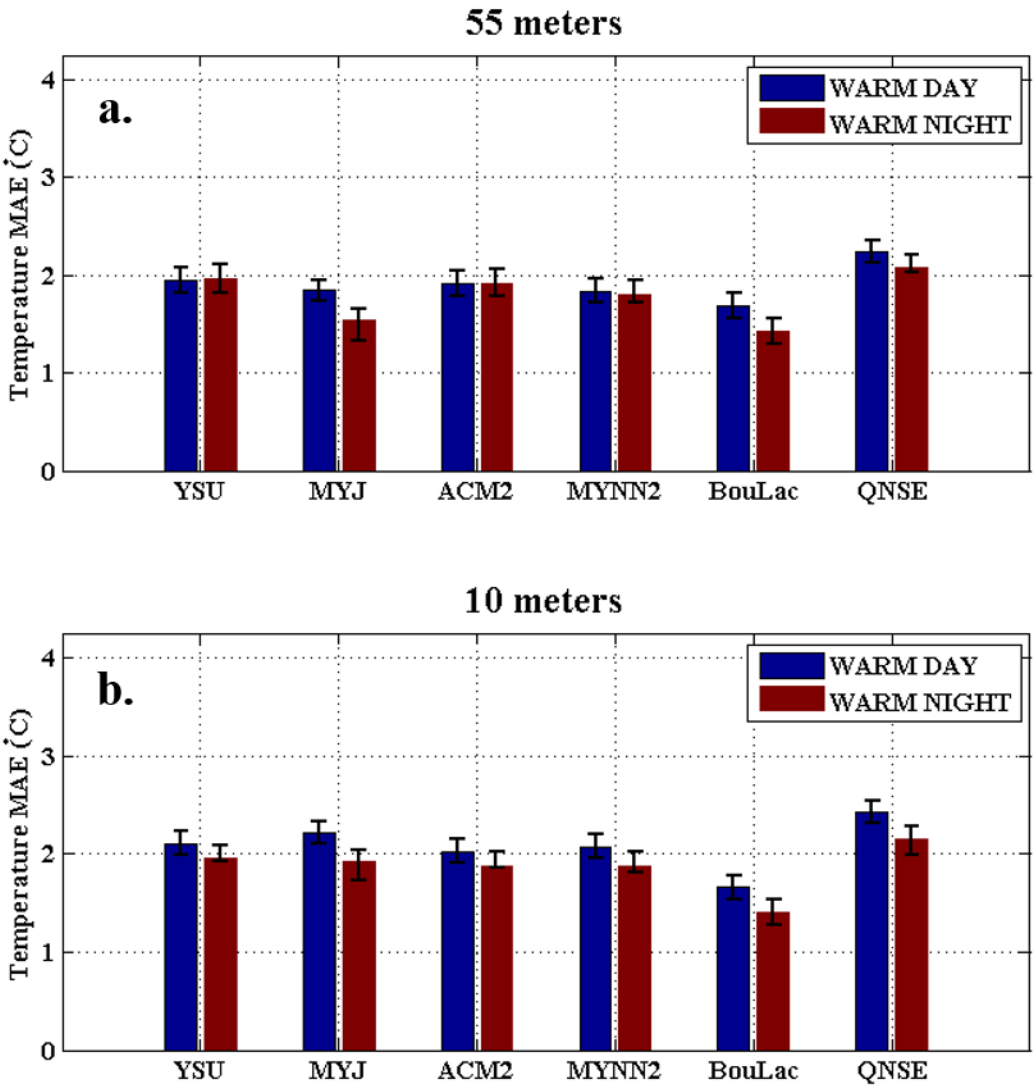

Figure 3.25. As in Fig. 3.23, but for mean absolute error in degrees Celsius.

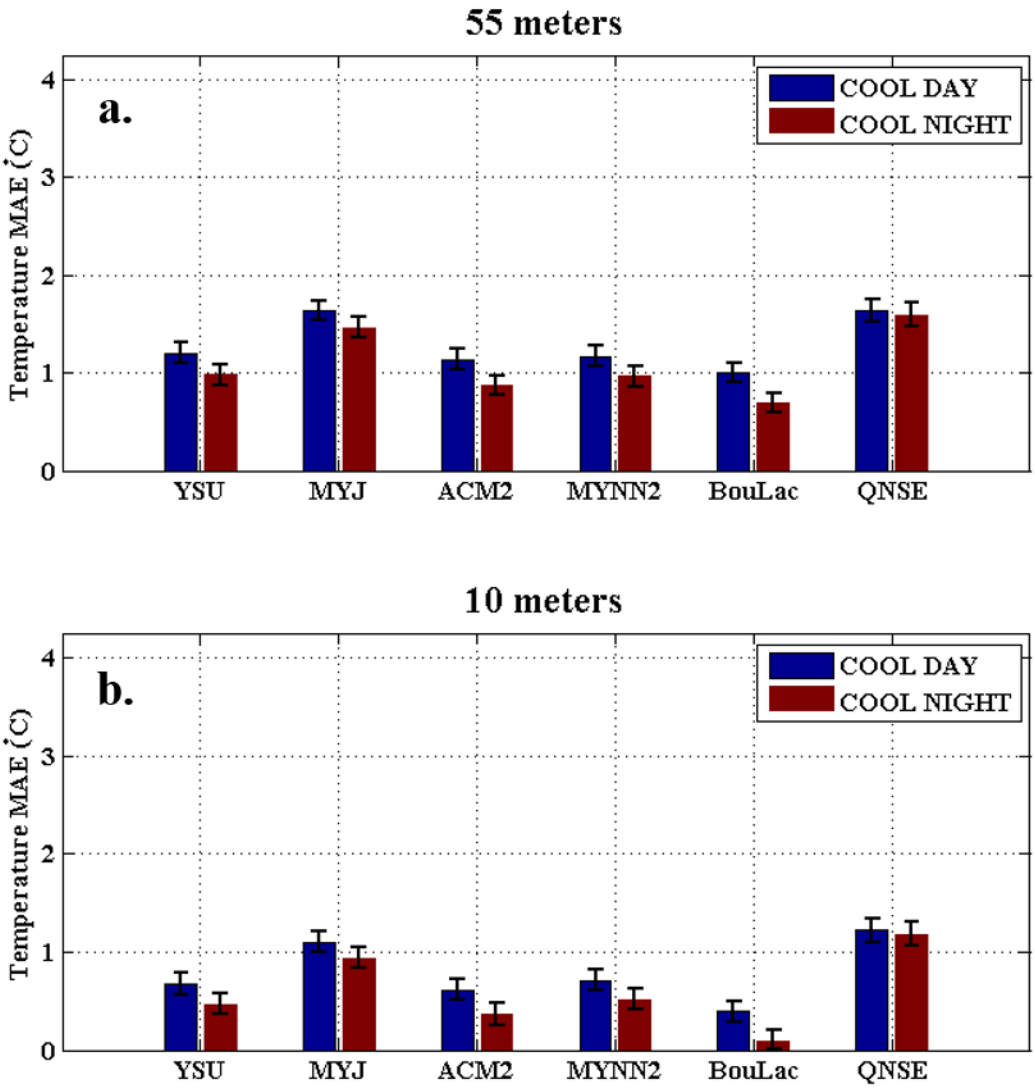

Figure 3.26. As in Fig. 3.25, but for the cool season (October to March).

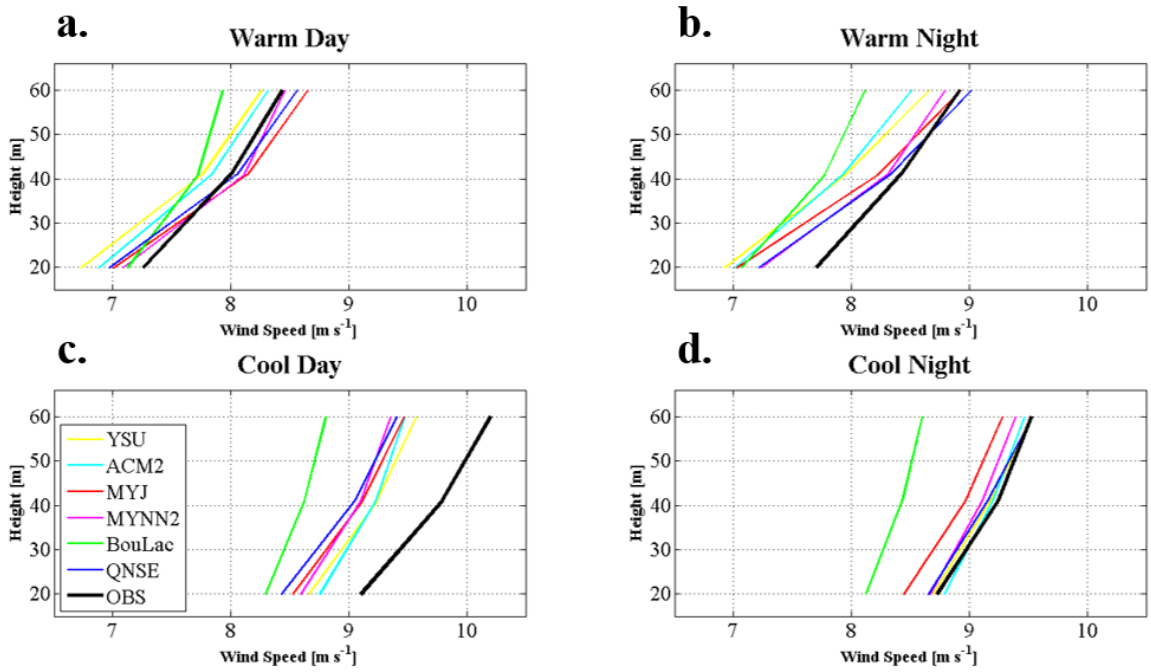

Figure 3.27. Composite profiles of potential temperature at the Cape Wind Meteorological Mast for observations and each of the six WRF PBL schemes for (a) the warm season daytime, (b) warm season nighttime, (c) cool season daytime and (d) cool season nighttime.

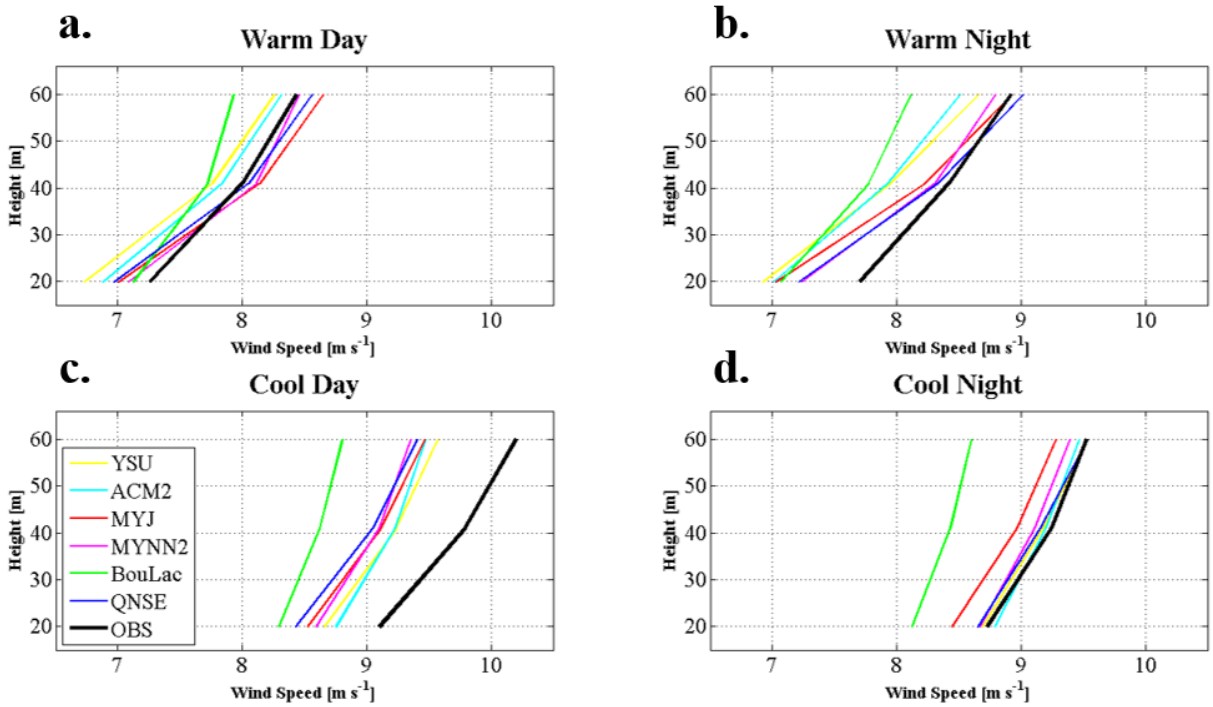

Figure 3.28. As in Fig. 3.27, but for wind speed in m s^{-1}.

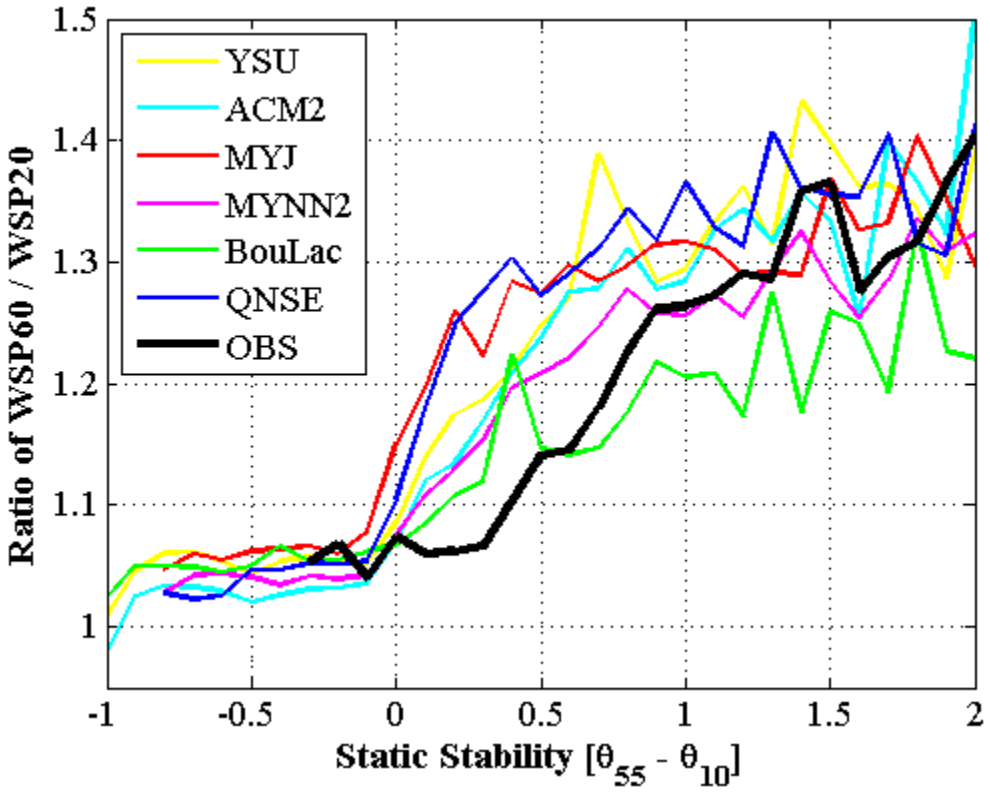

Figure 3.29. The ratio of 60-m wind speed to 20-m wind speed bin-averaged by static stability (potential temperature difference between 55 m and 10 m) for the tower observations and the six PBL schemes.

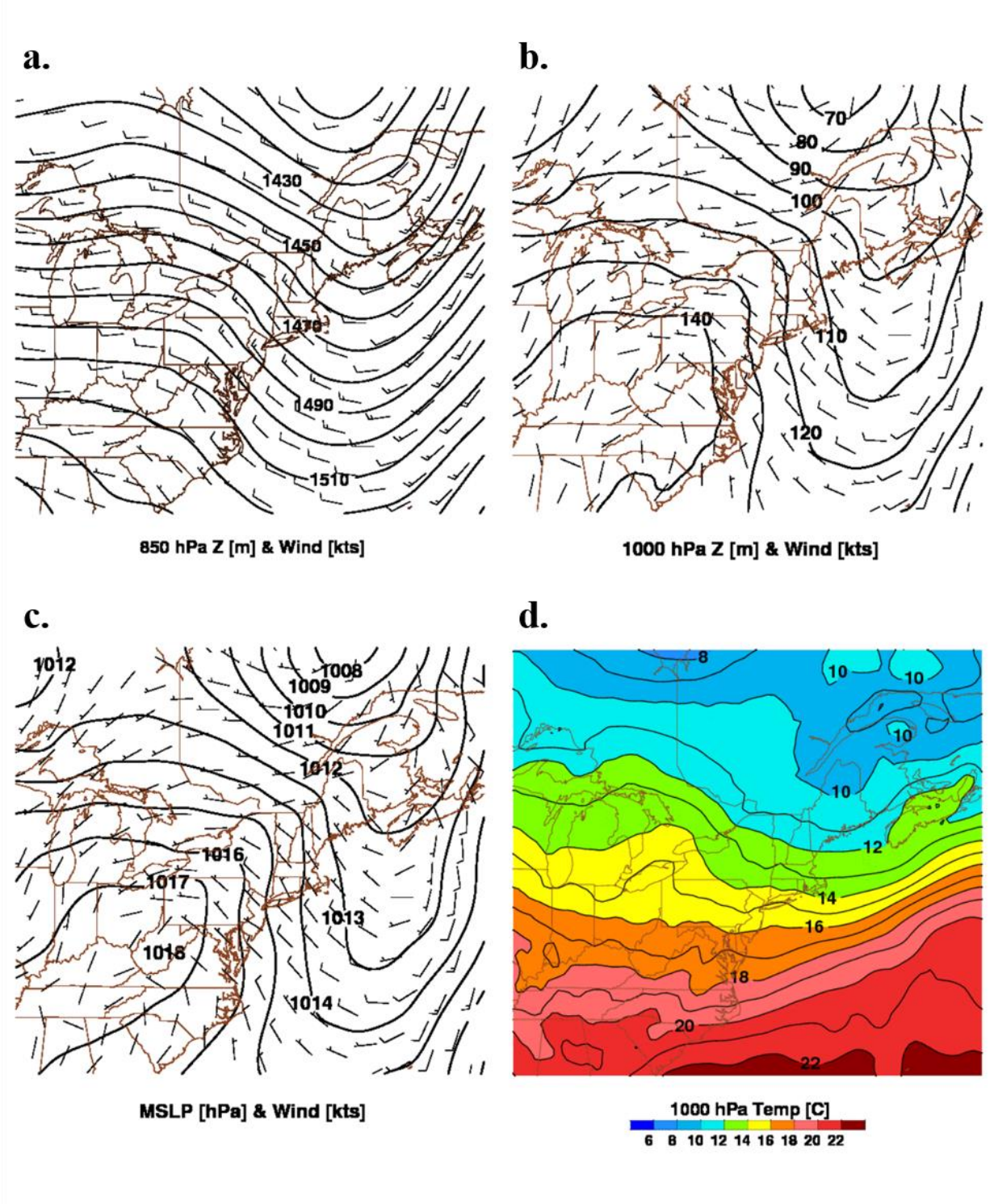

Figure 3.30. NARR composites for the 32 negative wind speed error cases for (a) 850 hPa geopotential heights and winds, (b) mean sea level pressure and 10-m winds, (c) 1000 hPa geopotential height and winds, and (d) 1000 hPa temperatures in Celsius.

Chapter 4: IMPOWR Flights 20-23 June 2013

4.1 Synoptic Overview

Three Long-EZ aircraft flights were conducted from 20-23 June 2013 as part of the IMPOWR field campaign. The goal of the flights was to retrieve targeted high-frequency observations of the marine atmospheric boundary layer off of the coast of southern New England and Long Island. The dates for flight operations were chosen based on favorable flow regimes for sampling of the MABL as well as potential diurnal coastal circulations. The synoptic regime over the four-day period was also representative of the ideal conditions during which offshore wind power generation could be maximized over the coastal waters of southern New England given the combination of high energy demand and a synoptically-enhanced flow regime.

A high pressure system moved across the region to a quasi-stationary position offshore of the Mid-Atlantic states on 20 June (Fig. 4.1a). Over the course of the next 3 days the high pressure system moved offshore of the southeast U.S. coast, resulting in prolonged southwesterly flow over the study region for the entire 4-day period (Fig. 4.1 b, c, d). Meanwhile, there was a series of weak cyclogenesis events in the lee of the Rocky Mountains along a frontal boundary extending from the Northern Plains through the Great Lakes and southern Ontario and Quebec.

4.2 IMPOWR Long-EZ Flights

Long-EZ flights were conducted out of eastern Long Island and lasted on average ~3 hours. The targeted areas included the coastal and offshore waters south of eastern Long Island to south of Martha's Vineyard and into Nantucket Sound, as well as Buzzard's Bay, northwest of Martha's Vineyard along the Massachusetts coast. The flights all took place between 1600 – 2300 UTC

(1200 – 1900 EDT) during the period of maximum diurnal heating. Since the flights occurred in the early summer, the water temperatures were still relatively cool (Fig. 4.2). Sea surface temperatures in the Gulf of Maine and over the New England Shelf were ~17 °C near the coast and approaching ~11 °C offshore. Figure 4.3 illustrates the land-sea air temperature differences throughout the time period, ranging from ~8 °C on 20 June to a maximum of ~13 °C on 23 June. The strong land-sea temperature differences had the effect of enhancing the low-level southwesterly synoptic flow through circulations resulting from differential heating and therefore differential pressures and the resulting gradient. Figure 4.4 shows observed wind speed and wind direction at 4 NDBC stations for the 5-day period of 20 – 24 June 2013. Peaks in wind speeds are visible in the late (1800 – 2300 UTC) hours of 20, 21 and 23 June at all stations, with 23 June showing the strongest winds of the 5-day period. Figure 4.5 shows the observed wind speeds at NDBC buoy 44020 in Nantucket Sound for the same 5-day period, along with the sea-level pressure difference between National Ocean Service (NOS) stations NTKM3 (Nantucket Island, MA) and BHBM3 (Boston, MA). Diurnal maximum SLP differences increased steadily from 3 hPa on 20 June to 4.5 hPa on 23 June, culminating in a maximum observed wind speed at 44020 of ~9.5 m s^{-1} that coincided with the maximum SLP difference.

4.2.1 20 June 2013

The Long-EZ flight on 20 June began at 1620 UTC with three north-south 25-km flight legs at low levels (< 300 m) before the aircraft headed for the south shore of Martha's Vineyard at an approximately constant altitude of 40 m. RAP analyses at 1800 UTC show a shallow high pressure system situated off of the Mid-Atlantic coast (Fig. 4.6e,f). Southwesterly winds at the coast near the surface become westerly (850 hPa) to northwesterly (500 hPa) with height to ~5 km

(Fig. 4.6a-d). Twenty-four hour backwards trajectories launched from the location of the Cape Wind tower in Nantucket Sound at 1800 UTC 20 June at multiple heights (50, 200, 500 m AGL) show that the air originated over the Gulf of Maine at low levels (Fig. 4.7; Draxler and Rolph 2014 http://www.arl.noaa.gov/HYSPLIT.php). The southwesterly winds at ~40 m along the 200-km flight leg increased from 3 m s^{-1} south of Long Island to 10 m s^{-1} in the vicinity of Martha's Vineyard (Fig. 4.8). Three 35-km flight legs were conducted in the Muskeget Channel between Martha's Vineyard and Nantucket to the Cape Wind tower at approximate altitudes of 40, 180 and 330 m. Winds were constantly southwesterly at all levels and variable between 6 and 11 m s^{-1}. A spiral was conducted around the Cape Wind tower at 1815 UTC from the water surface up to an altitude of 1000 m. Profiles of virtual potential temperature, mixing ratio and wind speed show a well-mixed layer below 230 m and a stable atmosphere above 230 m (Fig. 4.9). There was a wind maximum of ~10 m s^{-1} at an approximate altitude of 160 m. The aircraft then exited Nantucket Sound and retraced its route at altitudes below 60 m back to the waters south of Long Island (1820 – 1915 UTC). Winds along this last flight leg were also constantly out of the southwest and variable between 6 and 11 m s^{-1}.

4.2.2 21 June 2013

The second Long-EZ flight was conducted on 21 June beginning at 1730 UTC. A 300 hPa jet streak made its way southeast through Quebec, allowing a shortwave trough over northern New England to dig southward over the Gulf of Maine (not shown). RAP analyses at 1800 UTC show the trough extending down the New England coast and a tightened pressure gradient at 1000 hPa extending along the New England Shelf and through the Gulf of Maine, resulting in increased winds in these regions (Fig. 4.10e,f). The trough and enhanced winds also extend up to 500 hPa

(Fig. 4.10a-d). Backwards trajectories at 1800 UTC show that the air in Nantucket Sound originated over the waters southeast of the New England Shelf and did not interact with any land masses along their paths (Fig. 4.11). The aircraft followed a very similar flight path to the 20 June flight (Fig. 4.12). Along the initial flight leg at ~50 m from off of the south shore of Long Island to Martha's Vineyard the south-southwesterly winds were stronger than during the 20 June flight, increasing from ~5 m s^{-1} to over 13 m s^{-1}. Three 35-km flight legs were conducted from offshore waters to the south to the Cape Wind tower to the north at 40, 170 and 310 m. At the 40-m level the 10 m s^{-1} winds become more southerly and more turbulent heading into Nantucket Sound. Winds at 170 and 310 m are higher in Nantucket Sound (13 m s^{-1}) than to the south (10 m s^{-1}), and at 310 m the winds are noticeably more west-southwesterly than below, implying that the top of the MABL is below that level. Figure. 4.13 shows profiles of virtual potential temperature, mixing ratio and wind speed from an aircraft spiral around the Cape Wind tower at ~1923 UTC. A wind maximum of 14 m s^{-1} was observed above at ~180 m above a well-mixed layer in the lowest 150 m at the Cape Wind tower location. The flight legs extending to the south show that the MABL depth increases to the south. After departing the region, the aircraft performed shallow slant soundings (< 350 m) during the return trip to the south shore of Long Island. Wind speed, temperature and relative humidity were approximately constant above the MABL top at ~10 – 13 m s^{-1}, 20 °C and 40%, respectively. In the boundary layer, wind speed and temperature decreased to ~6 m s^{-1} and ~18.5 °C, respectively, while the relative humidity increased to 75% near the water surface.

4.2.3 23 June 2013

The third Long-EZ flight occurred on 23 June beginning at 2030 UTC. RAP analyses at 2100 UTC show intense diurnal heating in the Mid-Atlantic and southern New England exceeding 28 °C (Fig. 4.14f). The strong heating of the land surface, combined with a larger, deeper and more organized Bermuda high pressure system, resulted in tight pressure gradients and very strong southwesterly to west-southwesterly winds at 1000 and 925 hPa along the east coast (Fig. 4.14a-f). The low-level pressure gradient in southeastern New England was further increased by the southward movement into southern Vermont and New Hampshire of a weak frontal boundary associated with a low pressure system situated over the Great Lakes (Fig. 4.1).

Backwards trajectories show the air in Nantucket Sound at 2100 UTC originated offshore of the Delmarva Peninsula and did not flow over any land masses (Fig. 4.15). Aircraft slant soundings heading east from the south shore of Long Island and then north-northeast to the Cape Wind tower in Nantucket Sound revealed the presence of a shallow boundary layer (<240 m) with strong winds (15 – 20 m s^{-1}) at and above the boundary layer top (Fig. 4.16). Four 40-km flight legs were conducted between the Cape Wind tower and offshore waters to the south at altitudes of approximately 30, 180, 350 and 640 m. At the 30 m level the aircraft observations show wind speeds decreasing from 15 m s^{-1} to 10 m s^{-1} heading into Nantucket Sound, as well as temperatures decreasing from 20 °C to 18 °C. At 180 m and above the wind speeds and temperatures were approximately constant along the flight legs, ranging from 15 – 18 m s^{-1} and 21 – 22 °C, respectively. Above 180 m the wind directions noticeably veered to a more southwesterly direction than at the 30- and 180-m levels, implying that the MABL depth was less than 350 m.

Profiles of wind speed, mixing ratio and virtual potential temperature derived from an aircraft spiral sounding around the Cape Wind tower at ~2205 UTC confirmed the existence of a

stable layer below 260 m along with a wind maximum of 19 m s^{-1} at the top of the stable layer (Fig. 4.17). The aircraft then departed Nantucket Sound to the northwest and conducted a spiral sounding at the mouth of Buzzard's Bay followed by slant soundings in the lowest 700 m from Buzzard's Bay through Block Island Sound and back to the south shore of Long Island. The slant soundings showed the stable layer decreasing in depth from ~300 m to the northeast to ~200 m to the southwest along the flight track (Fig. 4.18a). At the top of the stable layer existed a >19 m s^{-1} low level jet that extended along the flight track to as far south as Montauk, NY (Fig. 4.18b).

4.3 WRF Simulations

WRF model simulations were performed for each of the 3 Long-EZ flights, using each of the 6 PBL schemes. NCEP Rapid Refresh hourly hybrid analyses were used as the initial and lateral boundary conditions, and the NCEP $1/12^{th}$ degree real-time global (RTG) SST was prescribed (initialized at 0000 UTC) and held constant for each run. A large outer 4-km domain covered most of New England and the Mid-Atlantic, as well as the associated offshore waters. A 1.33-km domain was one-way nested within the 4-km domain and situated over the flight operations area, extending from the New Jersey coast and New York Bight east past Cape Cod, MA. History files from the 4-km domain were output hourly, while history files for the 1.33-km domain were output every 5 minutes in order to aid in the interpolation of model variables to the aircraft flight track. Model runs were conducted out to 24 forecast hours beginning at 0000 UTC on the day of each flight.

4.3.1 20 June 2013

The 4-km domain output from the 6 PBL schemes were compared to surface observations for 20 June 2013 (Fig. 4.19). Observed wind speed at buoy 44020 show winds steadily increasing through the night and day from 1 – 8 m s^{-1}, whereas the models show a more diurnal trend in wind speed resulting in an under-prediction of ~2 m s^{-1} during the morning hours and slight over-predictions (0.25 – 1 m s^{-1}) during the time of the flight (1600 – 1900 UTC) (Fig. 4.19a). Observed and modeled sea-level pressure differences between Nantucket Island and Boston, MA are shown in Figure 4.19b. The models all show larger sea-level pressure differences (0.8 – 1.0 hPa) around the time of the flight. Land-sea surface temperature differences between buoy 44025 and BAF show the models exhibited larger temperature differences (2 – 3 °C) through the late morning and afternoon (1500 – 1900 UTC) (Fig. 4.19c).

Figure 4.20 shows aircraft and 1.33-km domain model profiles of virtual potential temperature, mixing ratio and wind speed for the aircraft spiral around the Cape Wind tower at ~1820 UTC. Where the aircraft observations show a stable atmosphere with a slight mixed layer below 210 m, the models show a very stable layer with a well-mixed layer above 210 m and a very shallow mixed layer near the surface (20 – 30 m). The MYJ scheme displays the most shallow near-surface mixed layer and the YSU and BouLac schemes show the deepest mixed layer. Figure 4.21 shows profiles of 1.33-km domain modeled and aircraft observed turbulent kinetic energy (TKE) for the spiral around the Cape Wind tower. Only the TKE-order PBL schemes are shown since the first-order schemes do not predict TKE. The MYJ scheme uses a minimum value of 0.1 m^2 s^{-2}. Observed TKE peaked at ~0.6 m^2 s^{-2} the top of the weak mixed layer (~210 m) and decreased linearly with height up through the stable layer. Modeled TKE was largest near the

surface (0.05 – 0.15 m^2 s^{-2}) and decreased to 0 m^2 s^{-2} at 200 m. This is consistent with the models being too stable below 210 m and thus resulting in weaker TKE and vertical mixing.

Figures 4.22a,b,c show observed and modeled winds (YSU and MYJ) along the flight track (20 – 60 m AGL) extending from the Cape Wind tower to the south shore of Long Island. Where the aircraft recorded 15 – 25 kt wind speeds along the entire flight track and strongest over open water and south of Block Island Sound and Long Island, all PBL schemes showed only 5 – 15 kt winds. While the YSU scheme exhibited weaker winds than the MYJ scheme south of Block Island Sound, both schemes under-predicted the low-level winds south of eastern Long Island by ~20 kts (~10 m s^{-1}). The weaker winds in the models in this region, along with the southeasterly flow shown in the observations compared to the southwesterly flow in the models, suggest the existence of a strong sea breeze circulation over eastern Long Island or a broader diurnal response that the models did not capture.

4.3.2 21 June 2013

The models were next compared for the second flight on 21 June. Model 4-km wind speeds in Nantucket Sound exhibited more variability around the time of the flight (1700 – 2000 UTC) with values ranging from 6.5 m s^{-1} (MYNN2) to 8 m s^{-1} (BouLac, QNSE) compared with observed values at 44020 of 7.5 – 8.2 m s^{-1} (Fig. 4.23a). The Nantucket to Boston SLP difference peaked at 1800 UTC in both the models and observations, as well as the 44025 to BAF surface temperature difference (Fig. 4.23b,c). Similar to 20 June the models displayed stronger temperature and SLP differences.

Along the low-level flight leg (30 – 50 m) from offshore of eastern Long Island to just south of Martha's Vineyard aircraft observations show south-southwesterly winds that increase

from 10 – 25 kts just south of Block Island Sound (Fig. 4.24a). Similar to the 20 June flight, the PBL schemes all under-predict the wind speeds in this region by 10 (MYJ) to 15 (YSU) kts (Fig. 4.24b,c).

Profiles of virtual potential temperature, mixing ratio and wind speed from an aircraft spiral around the Cape Wind tower at ~1920 UTC show a shallow mixed layer below 100 m in which wind speeds are approximately 9 – 11 m s^{-1} (Fig. 4.25). Similar to the 20 June flight the models display a shallower near-surface mixed layer (50 – 80 m) than the aircraft observations, with cooler θ_V values near the surface by ~1.5 K. This results in a sharper stable layer above the mixed layer as well as a lower and weaker jet in the models by approximately 1.5 – 4 m s^{-1}. The ACM2 scheme exhibited the deepest mixed layer (~80 m) as well as the highest mixing ratios (9.5 – 10 g kg^{-1}) and weakest wind speeds (7 – 10 m s^{-1}) within the mixed layer. The MYJ and QNSE schemes show the shallowest mixed layers (~50 m) with the strongest winds at the top of the mixed layer (~12 m s^{-1}). Above the mixed layer all schemes show wind speeds decreasing linearly with height up to approximately 800 m. The aircraft observations show a second wind maximum of ~13 m s^{-1} centered at ~400 m near the top of the strong stable layer. The models did not resolve this feature and all schemes under-predict the wind speeds above through and above the stable layer by up to 4 m s^{-1}. Figure 4.26 shows aircraft-derived and 1.33-km domain modeled TKE for the spiral around the Cape Wind tower. The aircraft observations display peaks of TKE of 1.2 and 1.1 m2 s-2 at 190 and 350 m, respectively. The peaks coincide with the low-level wind maximum and the height of the base of the higher wind maximum. The BouLac and MYNN2 schemes show peaks of 0.35 and 0.5, respectively, at ~25 m. All four TKE-prognostic schemes show TKE values decreasing to their minimum values above 200 m which is consistent with the presence of a strong stable layer in the models which acts to eliminate TKE.

4.3.3 23 June 2013

Land-sea surface temperature differences between the New England Shelf and internal New England were strongest on 23 June, peaking at 13 °C at 1900 UTC (Fig. 27c). The 4-km domain models lag behind in the heating of the land surface by 1 – 3 hours but generally agree well with the temperature contrast in the afternoon and evening (1200 – 2200 UTC) with the exception of the BouLac scheme which under-heats the land surface by ~2 °C. Maximum winds and Nantucket – Boston SLP gradients were observed later than 20 – 21 June from 2000 – 2200 UTC (Fig. 4.27a,b). The models still had the maximum SLP gradients coinciding with the diurnal heating showed stronger winds than observed after 2100 UTC by 2 – 4 m s^{-1}.

Heading east-northeast from the south shore of Long Island the aircraft performed a series of slant soundings below 800 m from 2036 – 2056 UTC that captured a shallow stable layer (<100 m) with 35 – 40 kt wind speeds above the stable layer (Fig. 4.28a). All model PBL schemes were 1.8 – 2 °C cooler than the observations near the surface resulting in a sharper stable layer (not shown). Wind speeds were 10 – 15 kts weaker above the stable layer in the models (Fig. 4.28b,c).

Figure 4.29 shows profiles of virtual potential temperature, mixing ratio and wind speed acquired from an aircraft sounding around the Cape Wind tower at ~2205 UTC. Near-surface θ_V were ~2.5 °C cooler in the models resulting in a cooler near-surface mixed layer and more stable layer above than in the observations. The BouLac scheme exhibited a deeper mixed layer (~200 m) than the other schemes. The two first-order PBL schemes (YSU and ACM2) show 175-m deep mixed layers and the remaining 3 TKE-order schemes show mixed layers of approximately 100 m. A sharp low level jet structure of 19 m s^{-1} was observed just above a shallow stable layer at 250 m, but all PBL schemes did not show such a sharp feature. However, most PBL schemes all over-

predicted the wind speeds below the jet structure by up to 2.5 m s^{-1} (MYJ). Possibly due to the cooler near-surface temperatures and sharper stable layers in the models, the all schemes except for the BouLac scheme under-predicted the height of the wind maximum by ~60 m. Figure 4.30 shows modeled and aircraft observed profiles of TKE for the spiral around the Cape Wind tower. Below 300 m the aircraft-derived TKE varies between 0.5 – 0.8 m^2 s^{-2}. Similar to the 20 – 21 June flights the four TKE-order schemes show TKE values that are less than observed and maximum near the surface (0.35 – 0.5 m^2 s^{-2}) that decrease to the minimum values above 200 m as the stable layer acts to eliminate TKE.

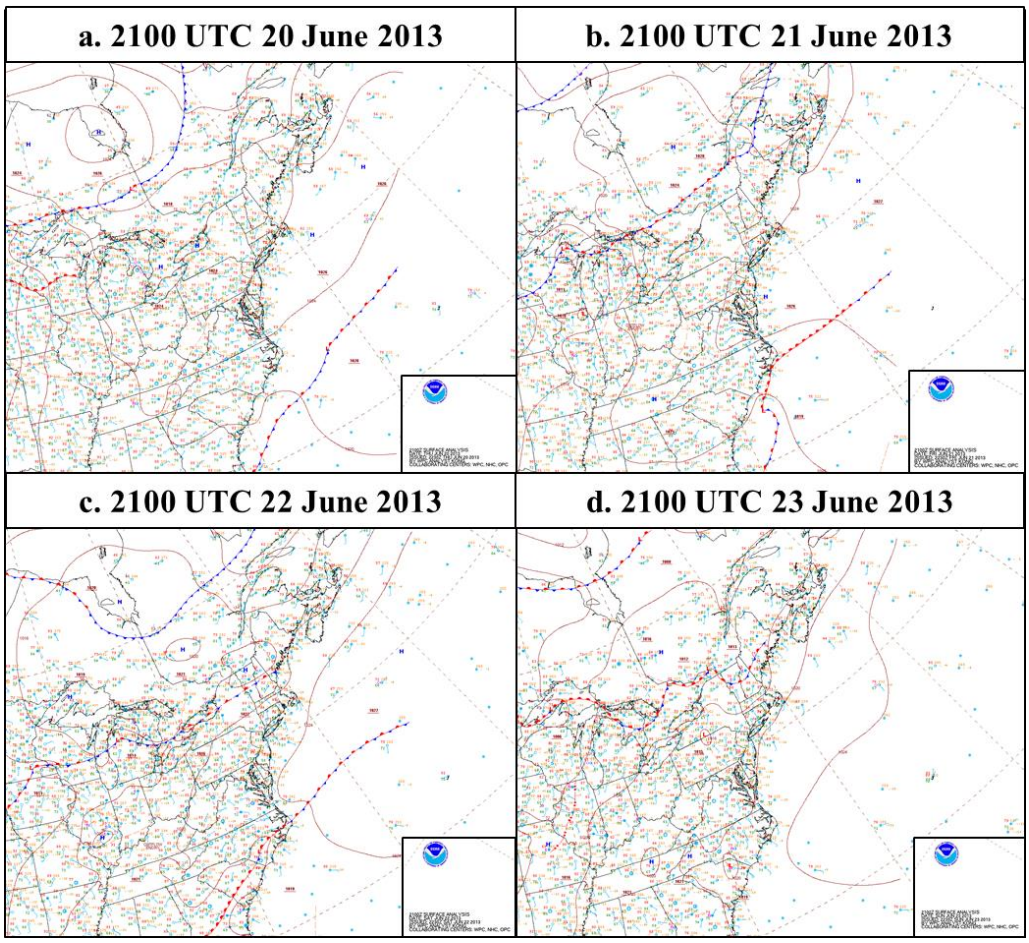

Figure 4.1. WPC surface analyses displaying the synoptic evolution over the 4-day period of Long-EZ flights for 2100 UTC (a) 20 June 2013, (b) 21 June 2013, (c) 22 June 2013, (d) 23 June 2013.

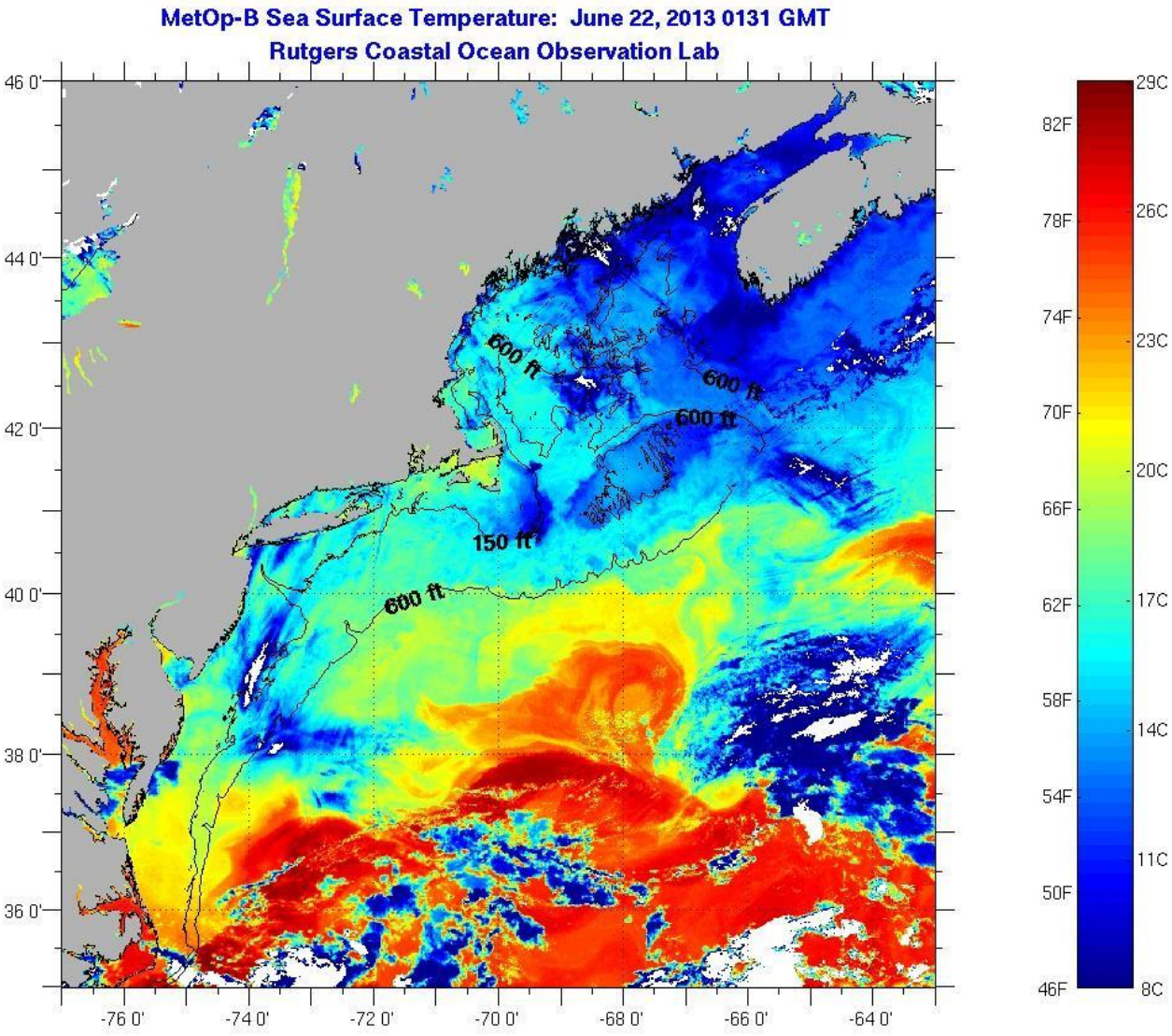

Figure 4.2. Satellite-observed sea surface temperatures for the NEUS coastal and offshore waters on 22 June 2013 from Rutgers University Coastal Ocean Observation Lab (http://marine.rutgers.edu/cool/sat_data/?nothumbs=0&product=sst).

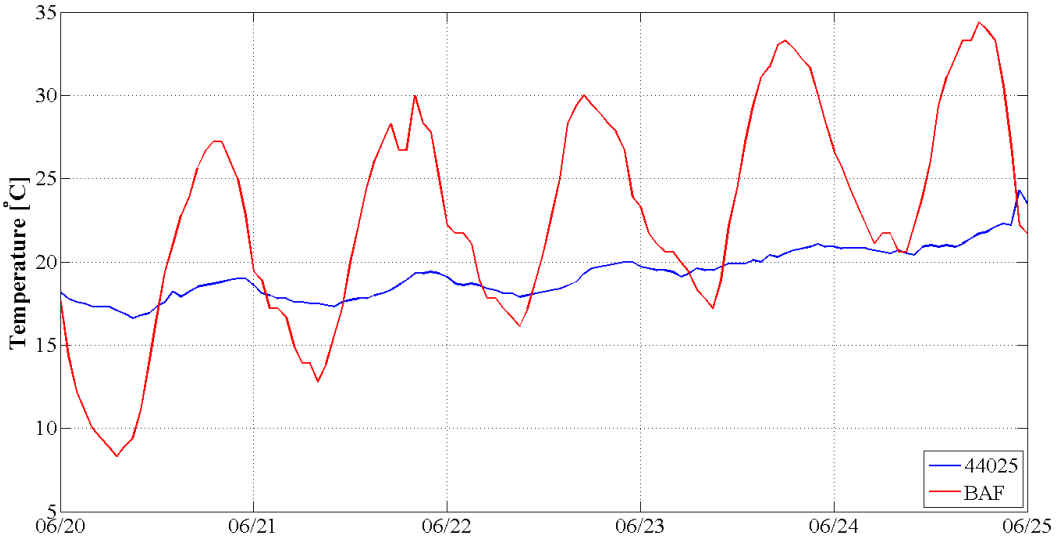

Figure 4.3. Observed surface temperatures (°C) for the 5-day period 20 – 24 June 2013 for ASOS station BAF (red) and buoy 44025 (blue).

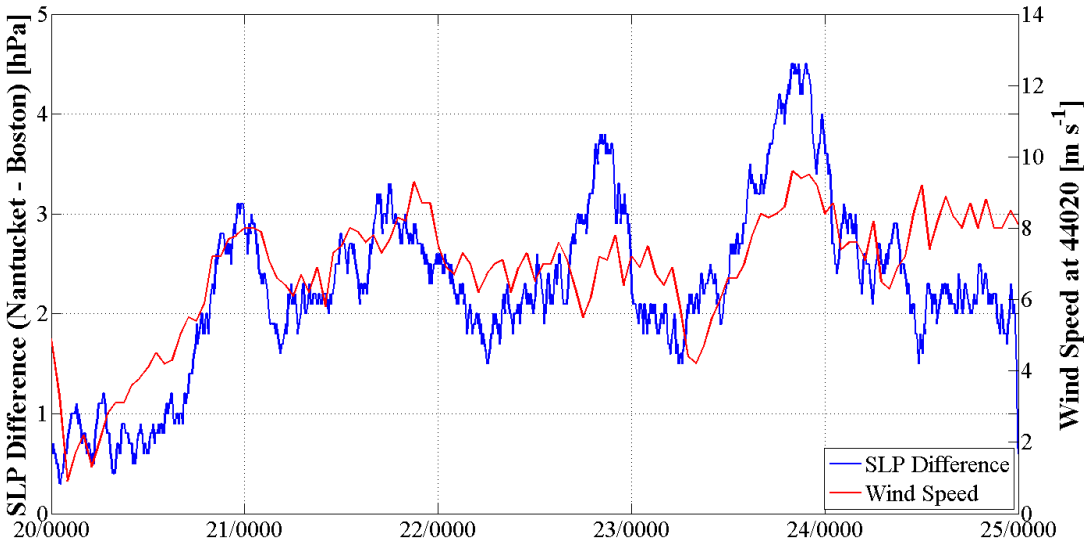

Figure 4.4. Observed sea-level pressure difference (hPa) between NOS station NTKM3 on Nantucket Island, MA and NOS station BHBM3 in Boston, MA for the 5-day period 20 – 24 June 2013 (blue) and the observed wind speed (m s^{-1}) at buoy 44020 in Nantucket Sound (red).

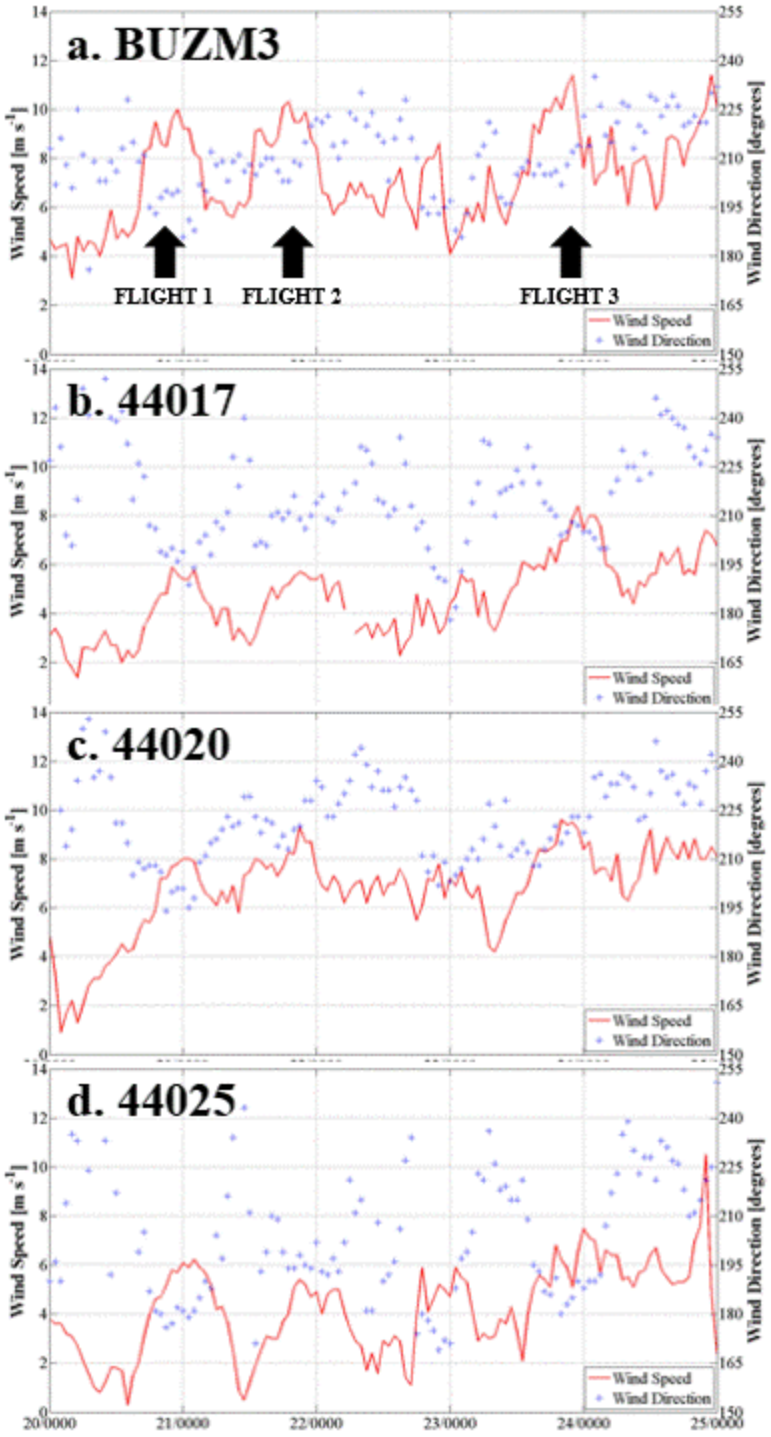

Figure 4.5. Observed wind speed (m s-1) (red) and wind direction (blue) for (a) C-MAN station BUZM3 in Buzzard's Bay, (b) buoy 44017, (c) buoy 44020, and (d) buoy 44025.

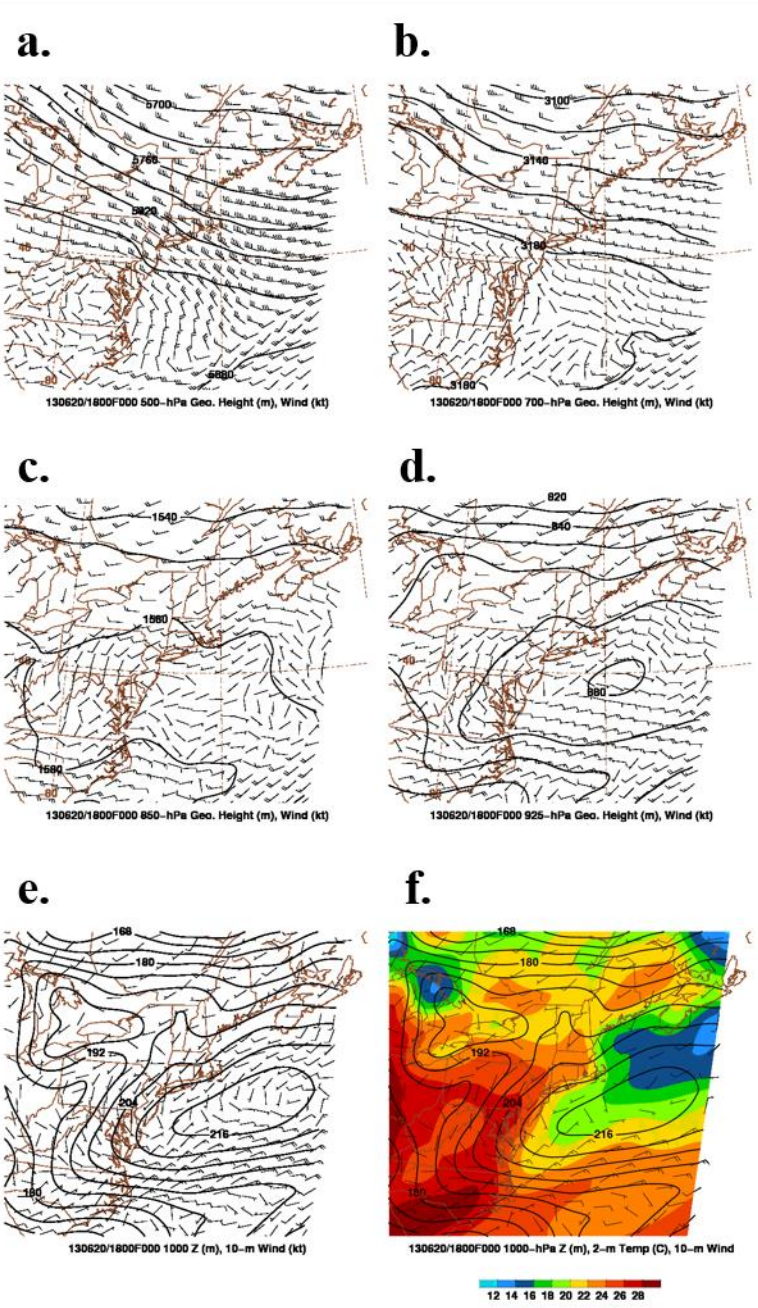

Figure 4.6. RAP analyses for 1800 UTC 20 June 2013 of (a) 500 hPa geopotential height (m, solid contours) and wind (kts, barbs), (b) 700 hPa geopotential height (m, solid contours) and wind (kts, barbs), (c) 850 hPa geopotential height (m, solid contours) and wind (kts, barbs), (d) 925 hPa geopotential height (m, solid contours) and wind (kts, barbs), (e) 1000 hPa geopotential height (m, solid contours) and wind (kts, barbs), and (f) 1000 hPa geopotential height (m, solid contours), 2-m temperature (°C, shaded contours) and 10-m wind (kts, barbs).

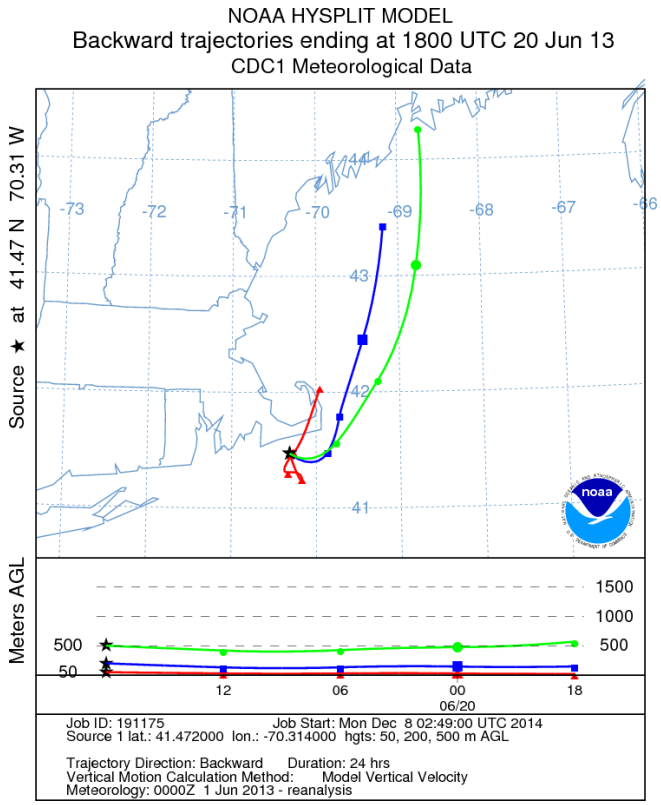

Figure 4.7. NOAA HYSPLIT Model backwards trajectories ending at 1800 UTC 20 June 2013 at the Cape Wind tower location in Nantucket Sound for 50 m (red), 200 m (blue), and 500 m (blue).

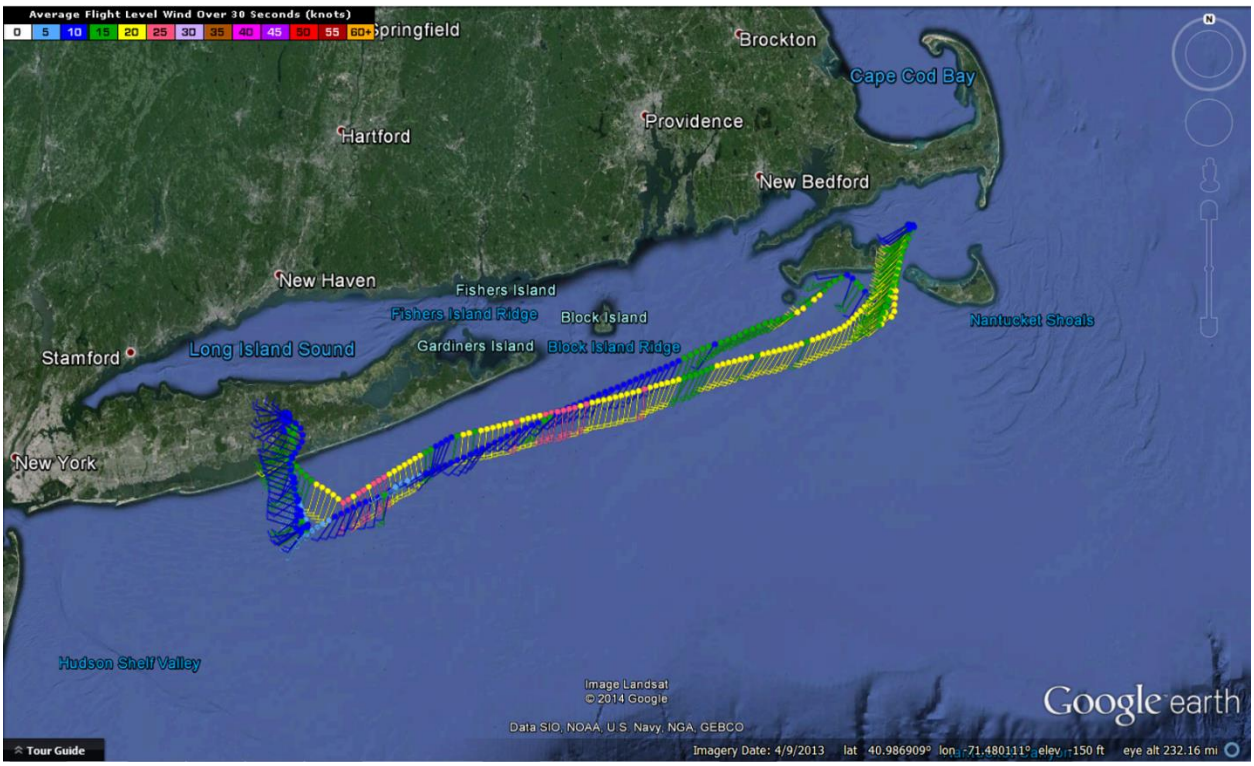

Figure 4.8. Map showing winds (kts, barbs) along the aircraft flight track for the Long-EZ flight on 20 June 2013.

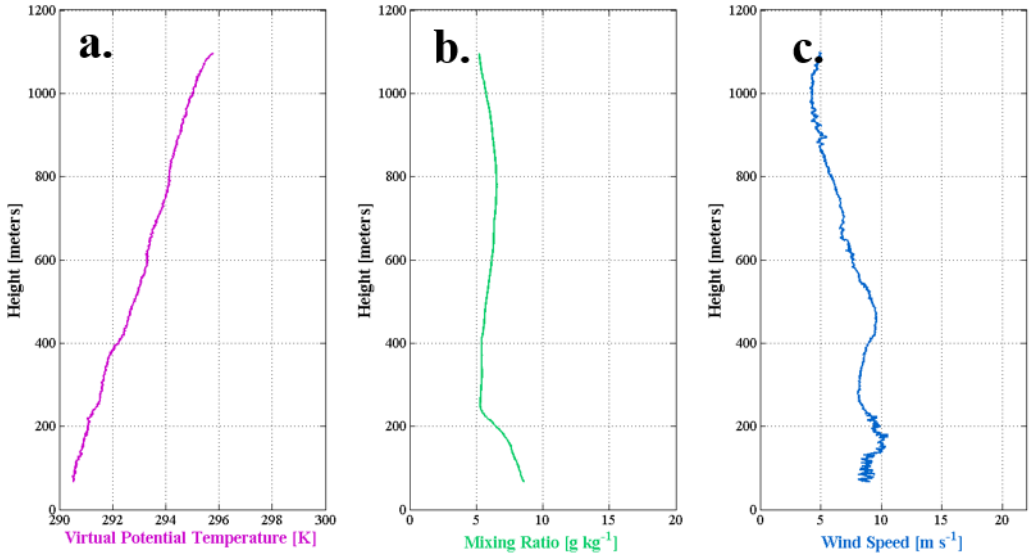

Figure 4.9. Aircraft-derived profiles of (a) virtual potential temperature (K), (b) mixing ratio (g kg^{-1}), and (c) wind speed (m s^{-1}) for the aircraft spiral around the Cape Wind tower at ~1820 UTC 20 June 2013.

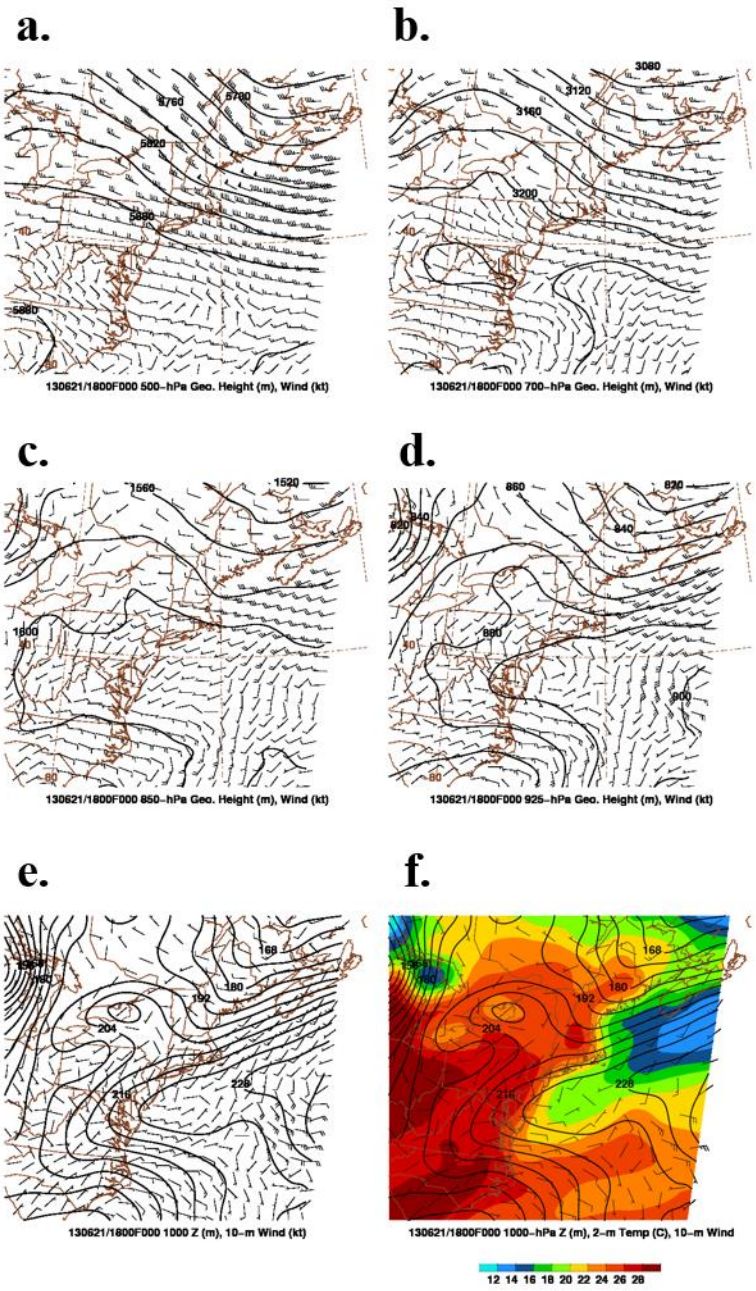

Figure 4.10. As in Fig. 4.6 but for 1800 UTC 21 June 2013.

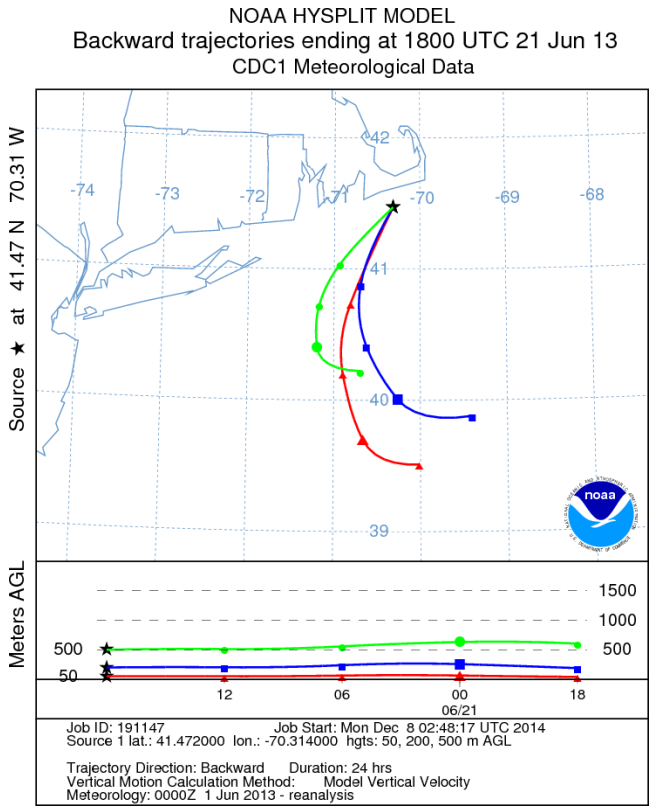

Figure 4.11. As in Fig. 4.7 but ending at 1800 UTC 21 June 2013.

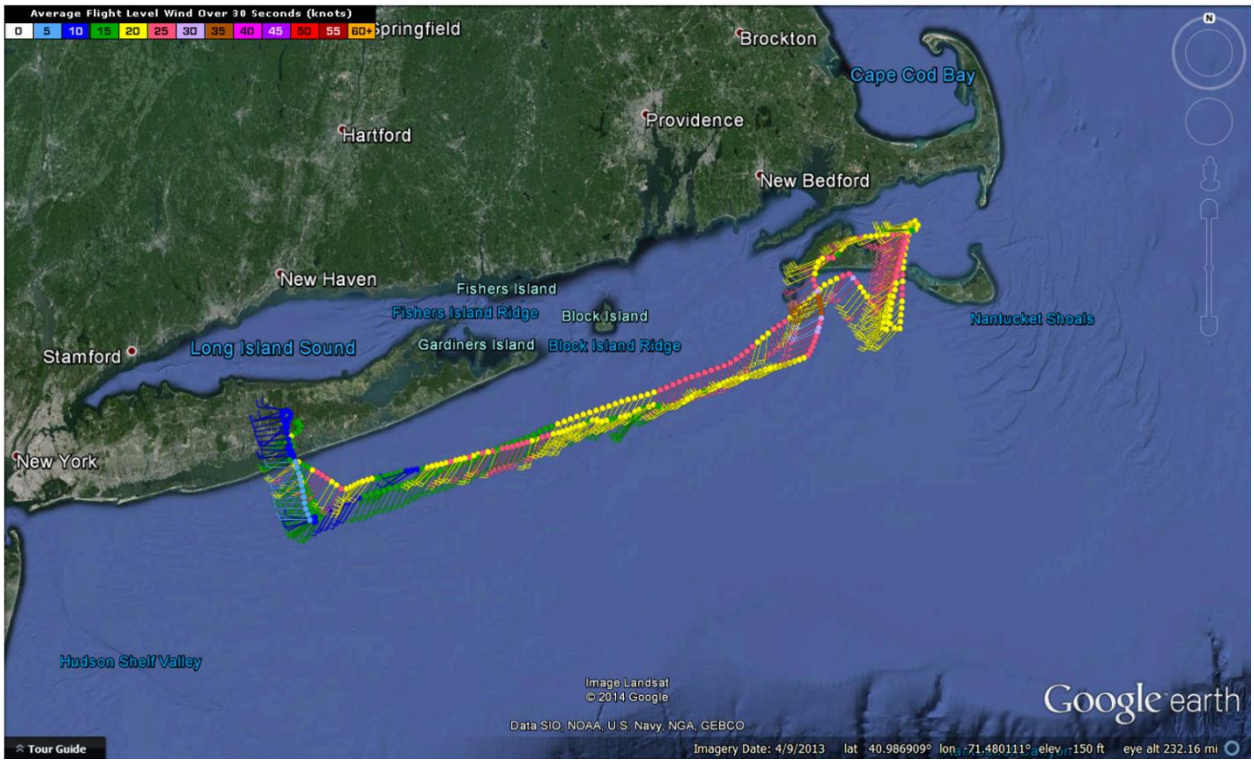

Figure 4.12. As in Fig. 4.8 but for the aircraft flight on 21 June 2013.

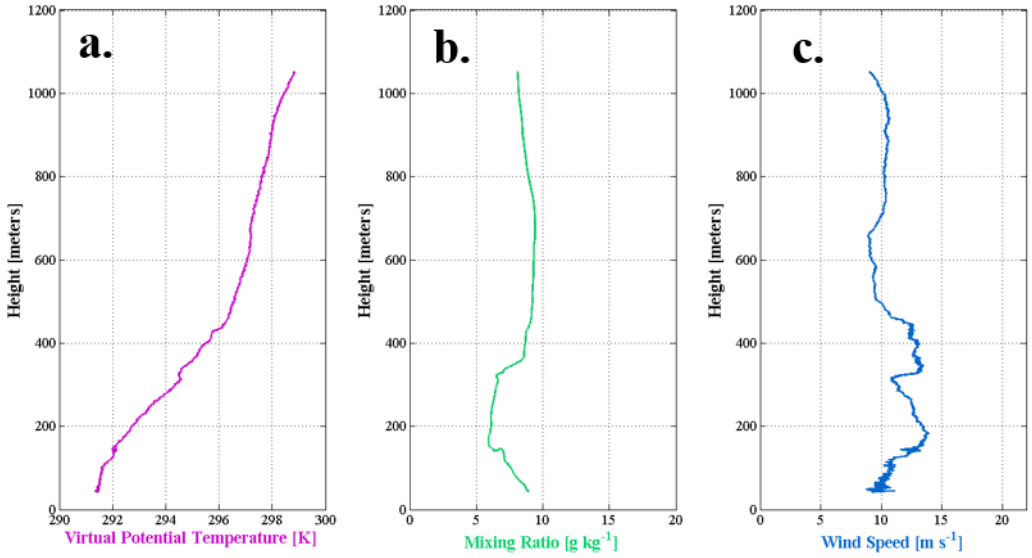

Figure 4.13. As in Fig. 4.9 but for the aircraft spiral around the Cape Wind tower at ~1925 UTC 21 June 2013.

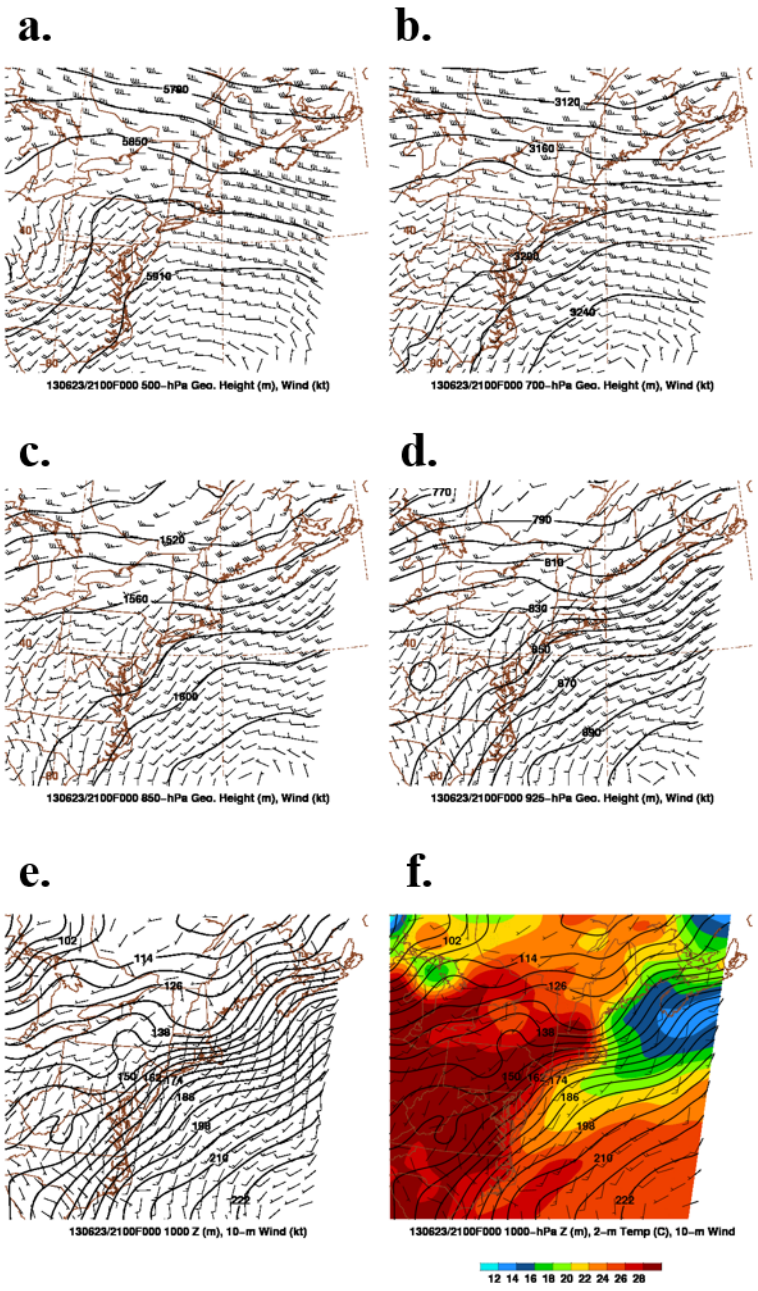

Figure 4.14. As in Fig. 4.6 but for 2100 UTC 23 June 2013.

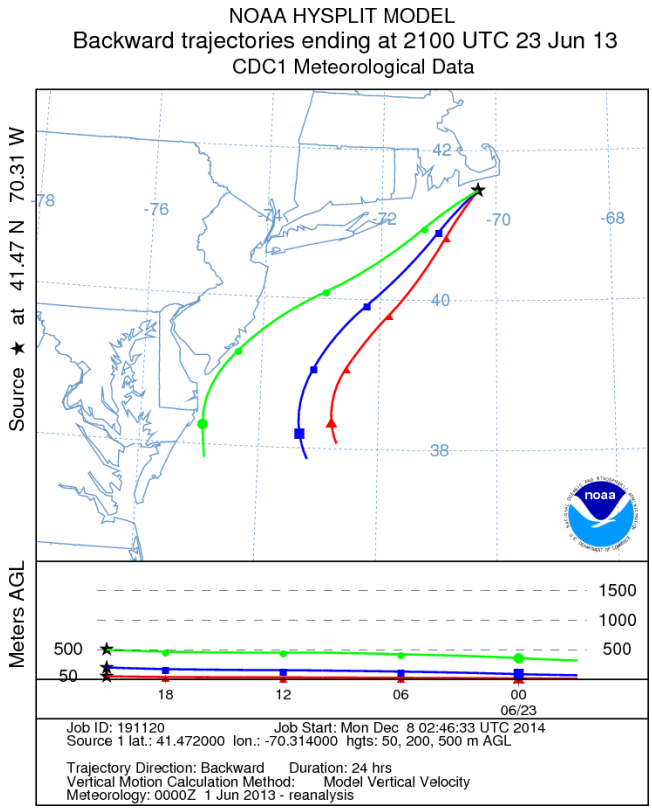

Figure 4.15. As in Fig. 4.7 but ending at 2100 UTC 23 June 2013.

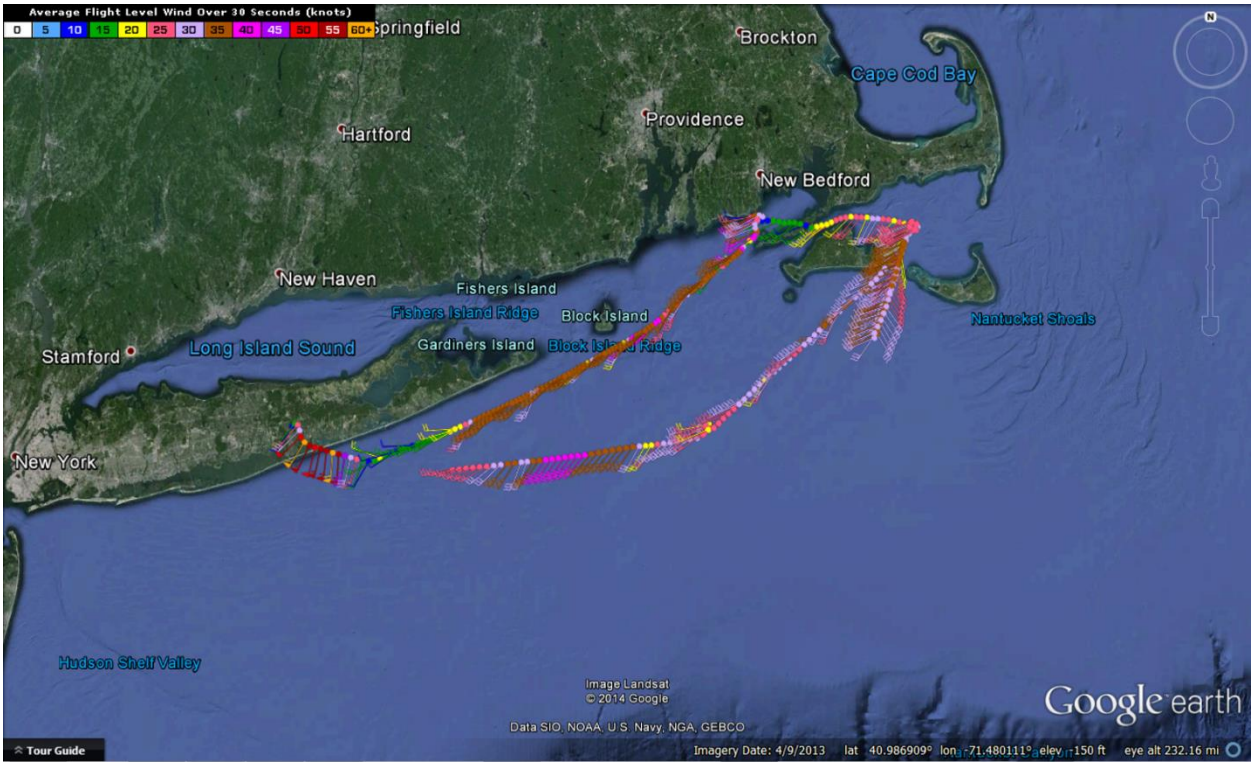

Figure 4.16. As in Fig. 4.8 but for the Long-EZ flight on 23 June 2013.

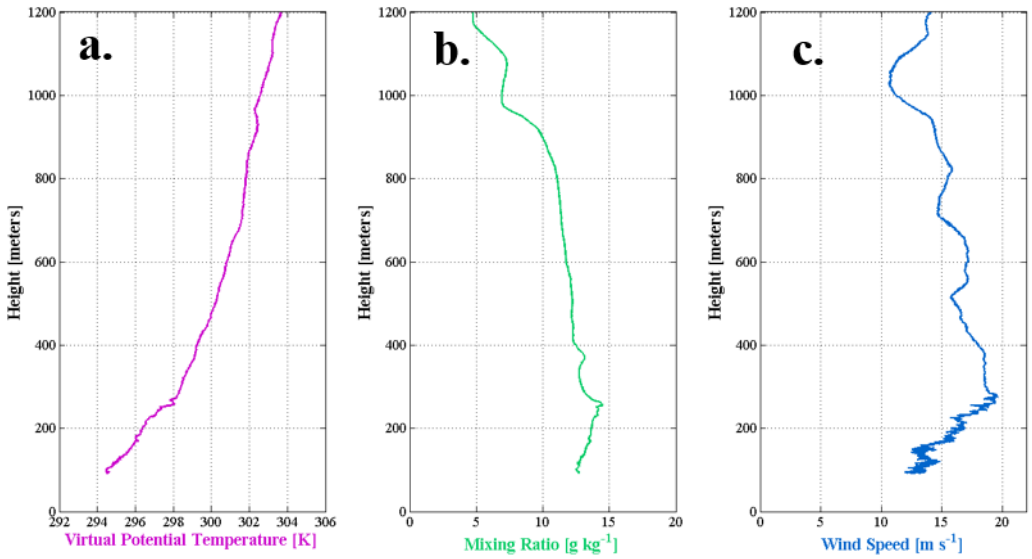

Figure 4.17. As in Fig. 4.9 but for the aircraft spiral around the Cape Wind tower at ~2205 UTC 23 June 2013.

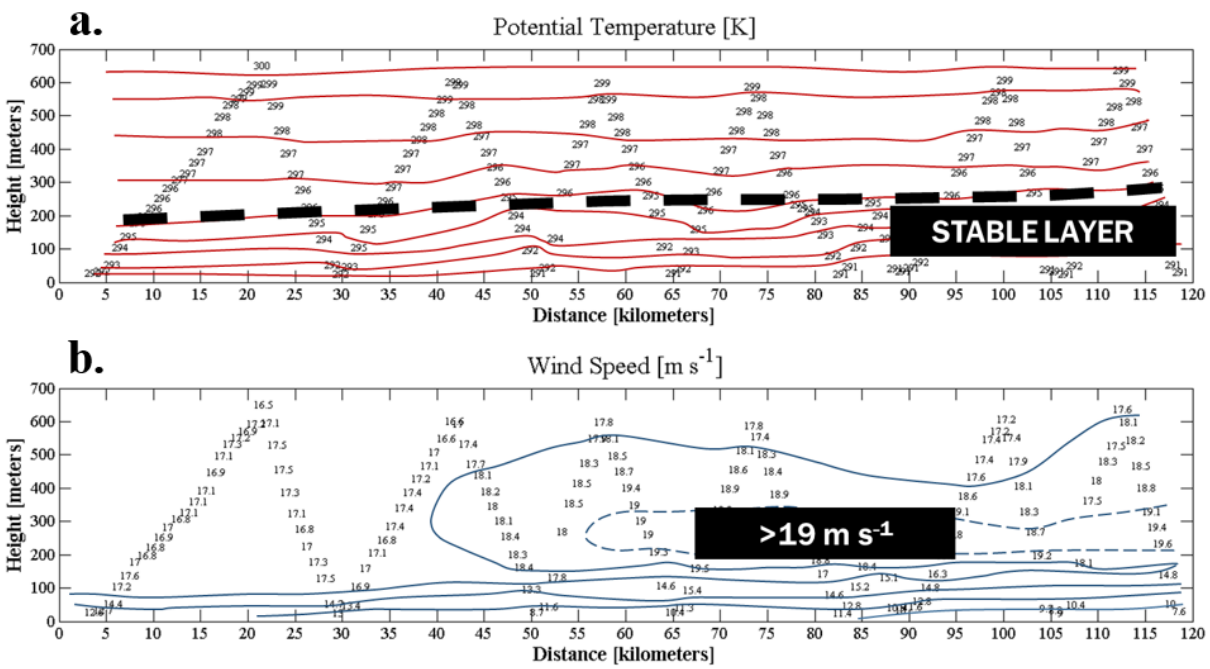

Figure 4.18. Analyses of aircraft-observed (a) potential temperature (K) and (b) wind speed (m s^{-1}) along the 120-km slant-soundings flight leg extending from Buzzard's Bay to the south shore of Long Island on 23 June 2013. Numbers represent 3-second averaged values.

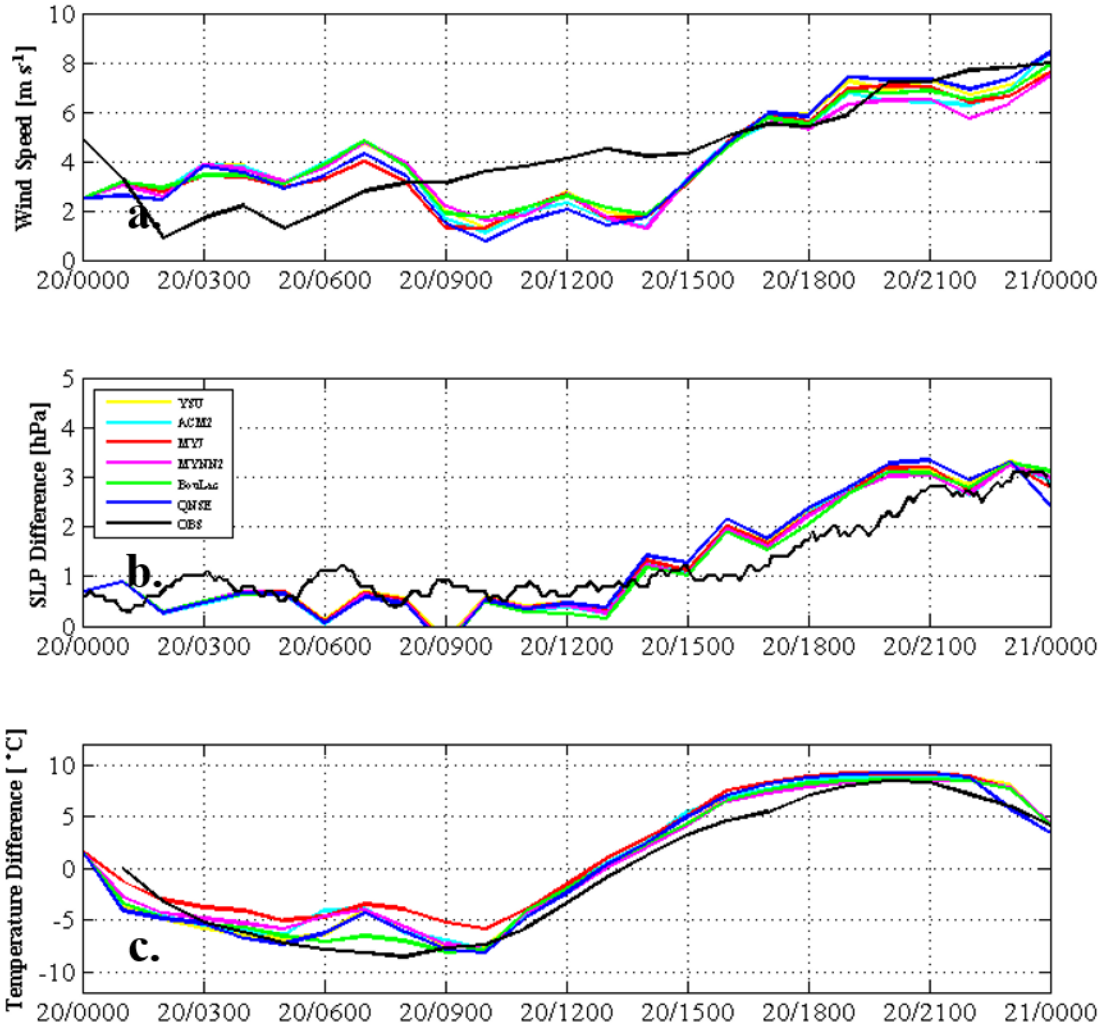

Figure 4.19. (a) Time-series of model 10-m winds vs. observed wind speed (m s^{-1}) at buoy 44020 in Nantucket Sound, (b) modeled and observed sea-level pressure difference (hPa) between Nantucket Island, MA and Boston, MA and (c) the modeled and observed temperature difference (°C) between BAF and buoy 44025 for 20 June 2013.

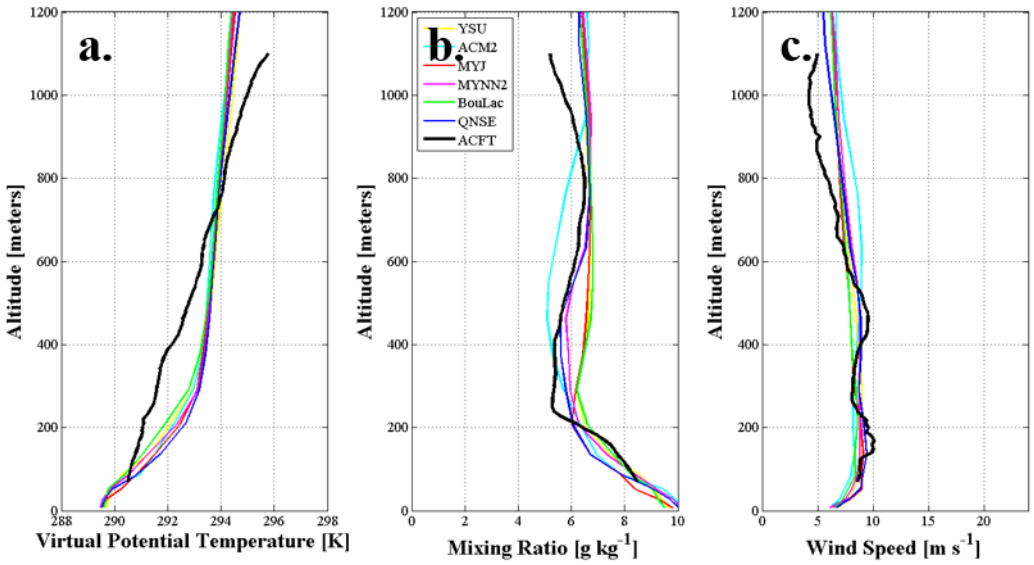

Figure 4.20. Modeled and observed profiles of (a) virtual potential temperature (K), (b) mixing ratio (g kg^{-1}) and (c) wind speed (m s^{-1}) for the aircraft spiral around the Cape Wind tower at ~1820 UTC 20 June 2013.

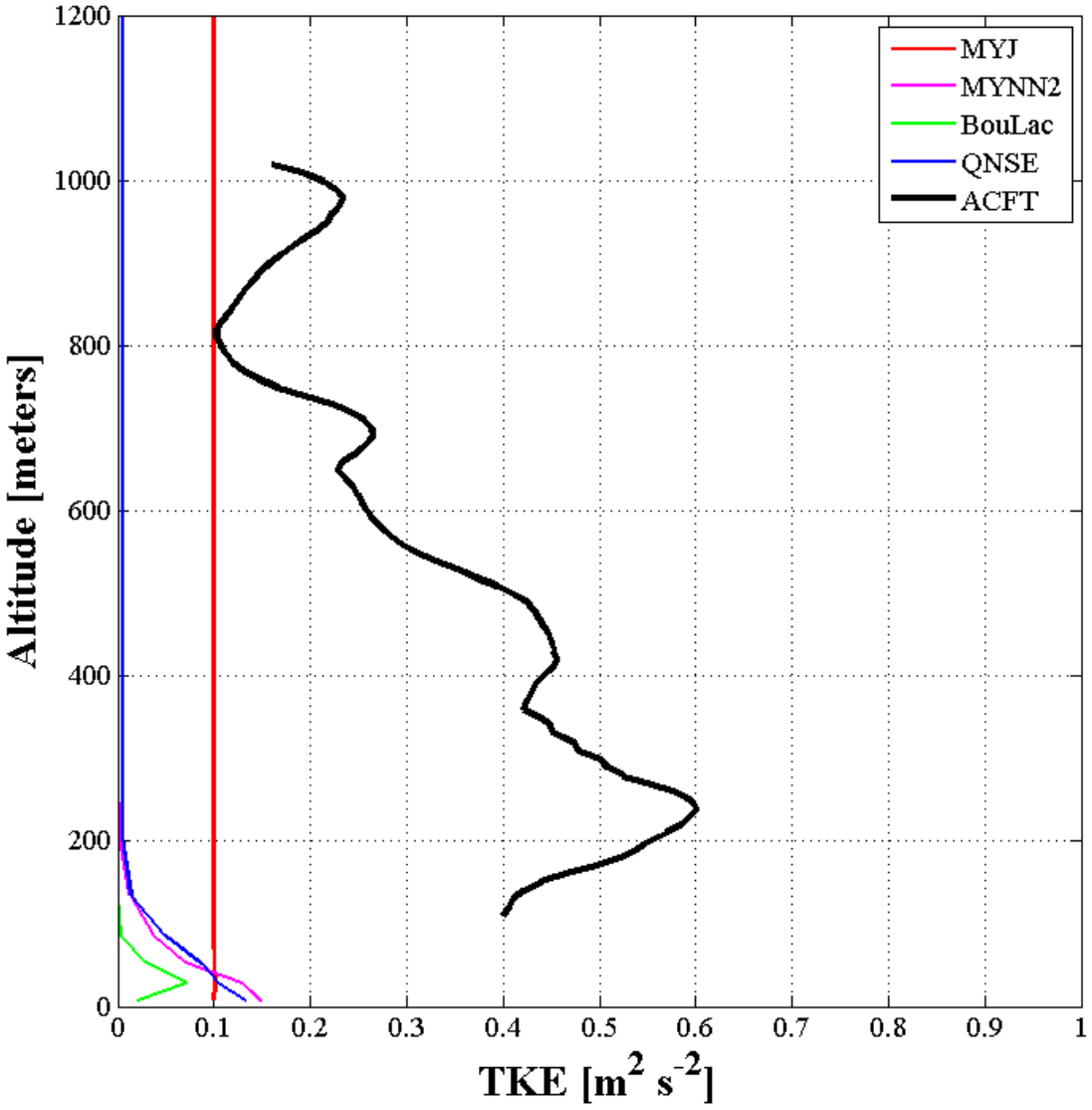

Figure 4.21. Profiles of modeled and observed turbulent kinetic energy ($m^2 s^{-2}$) for the aircraft spiral around the Cape Wind tower at ~1820 UTC 20 June 2013.

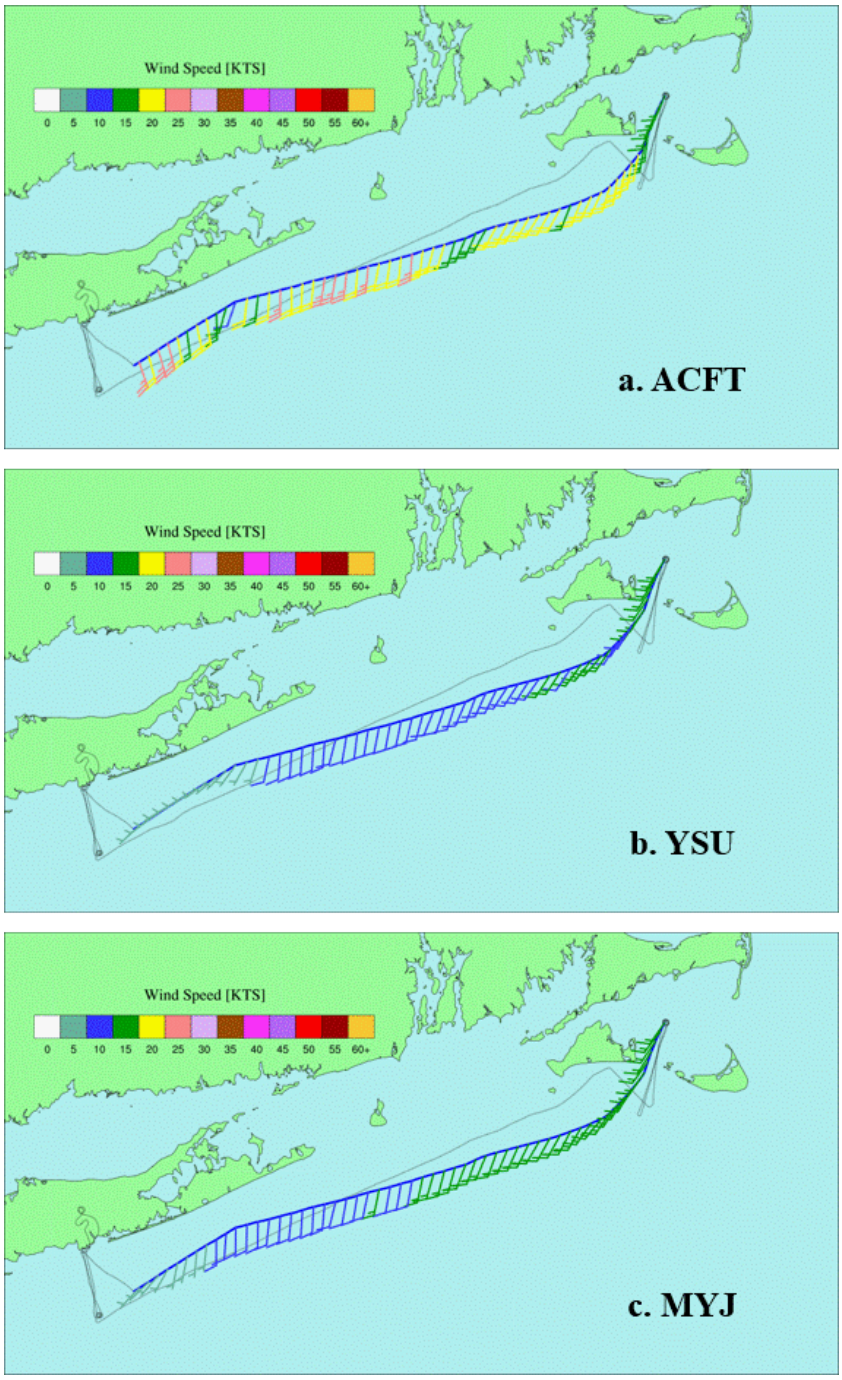

Figure 4.22. Winds (kts, barbs) along the low-level (20 – 60 m) flight track heading from Nantucket Sound to the south shore of Long Island for 1820 – 1916 UTC 20 June 2013 for (a) aircraft observations, (b) YSU PBL scheme, and (c) MYJ PBL scheme.

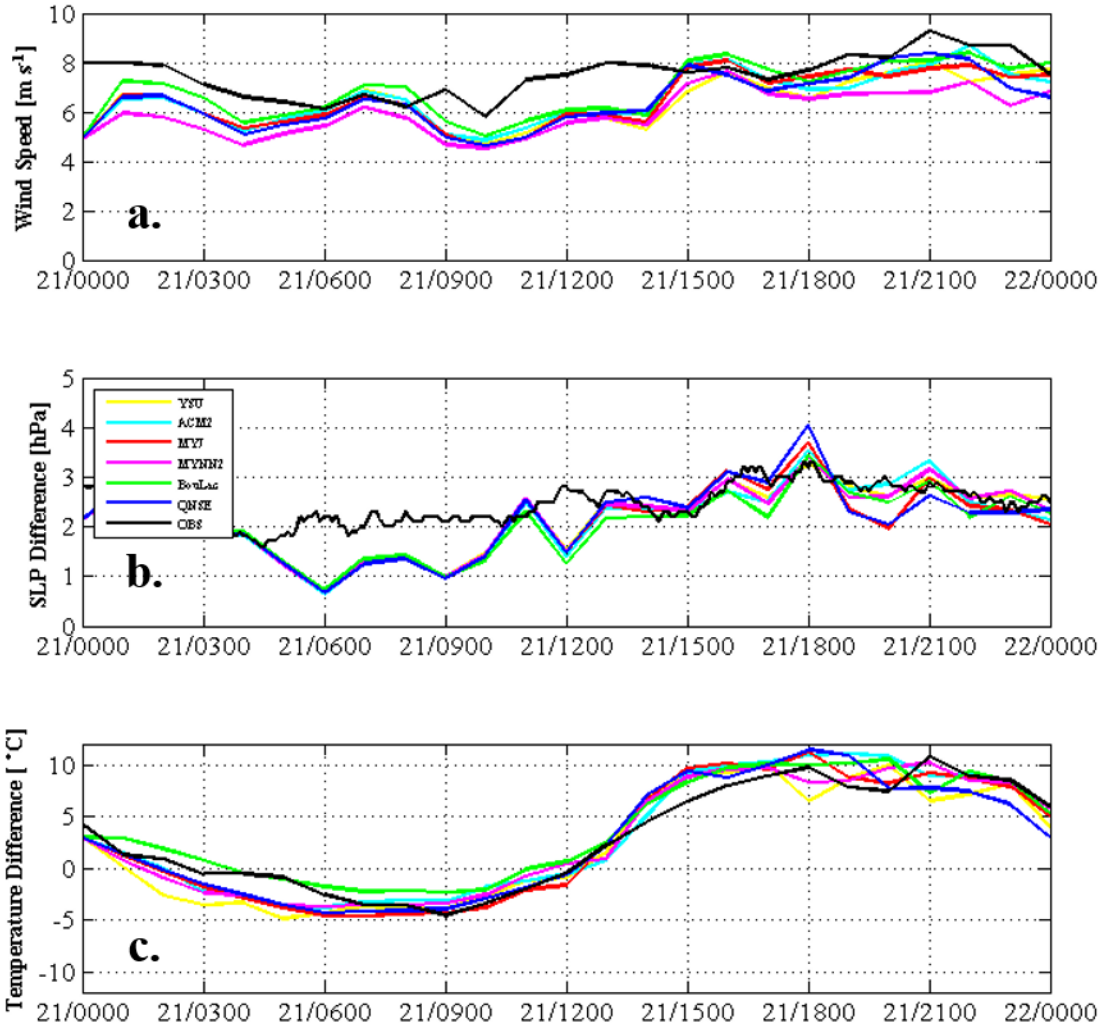

Figure 4.23. As in Fig. 4.19 but for 21 June 2013.

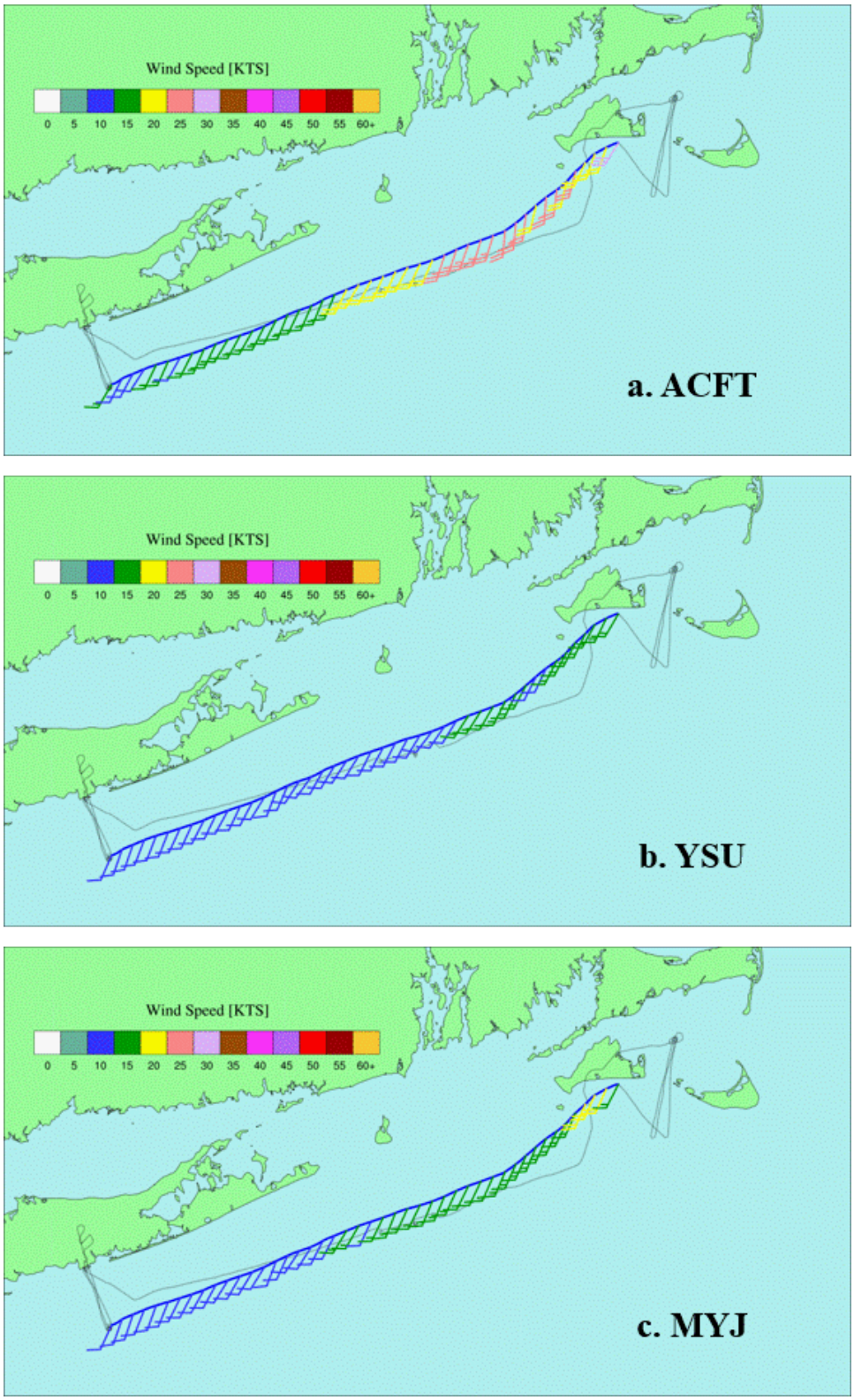

Figure 4.24. Winds (kts, barbs) along the low-level flight track from 1802 – 1846 UTC 21 June 2013 for (a) aircraft observations, (b) the YSU PBL scheme, and (c) the MYJ PBL scheme.

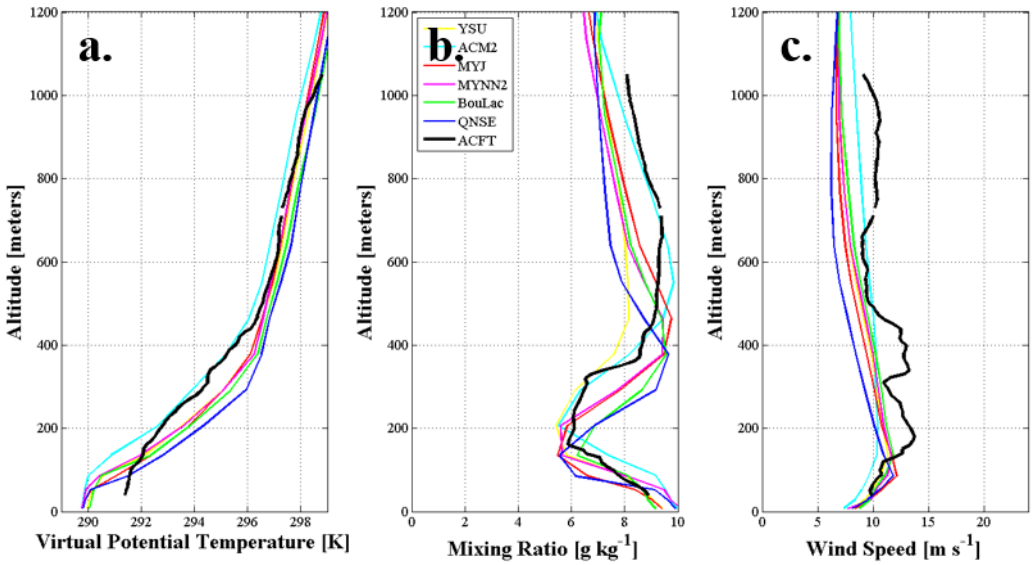

Figure 4.25. As in Fig. 4.20 but for the aircraft spiral around the Cape Wind tower at ~1925 UTC 21 June 2013.

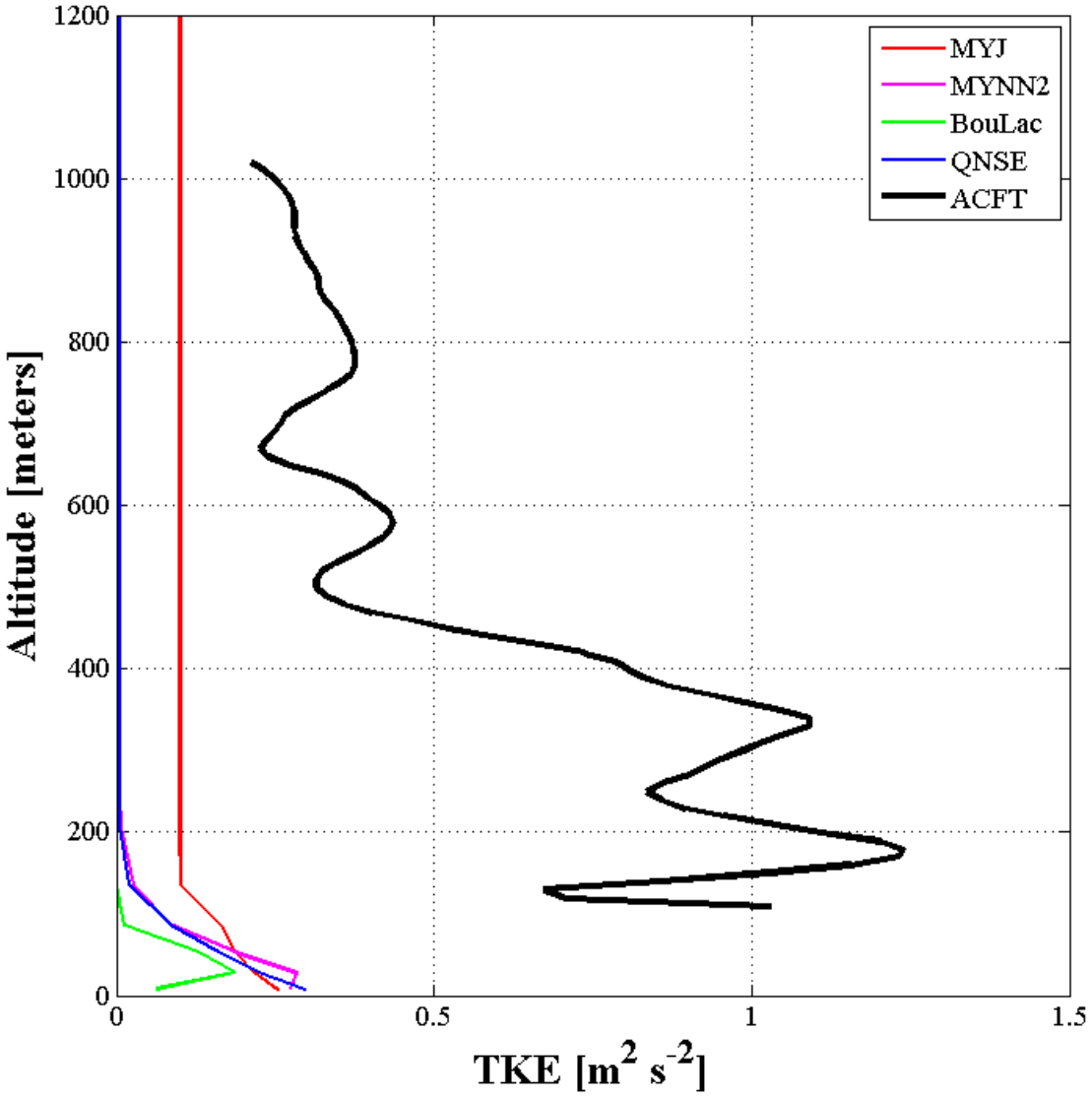

Figure 4.26. As in Fig. 4.21 but for the aircraft spiral around the Cape Wind tower at ~1925 UTC 21 June 2013.

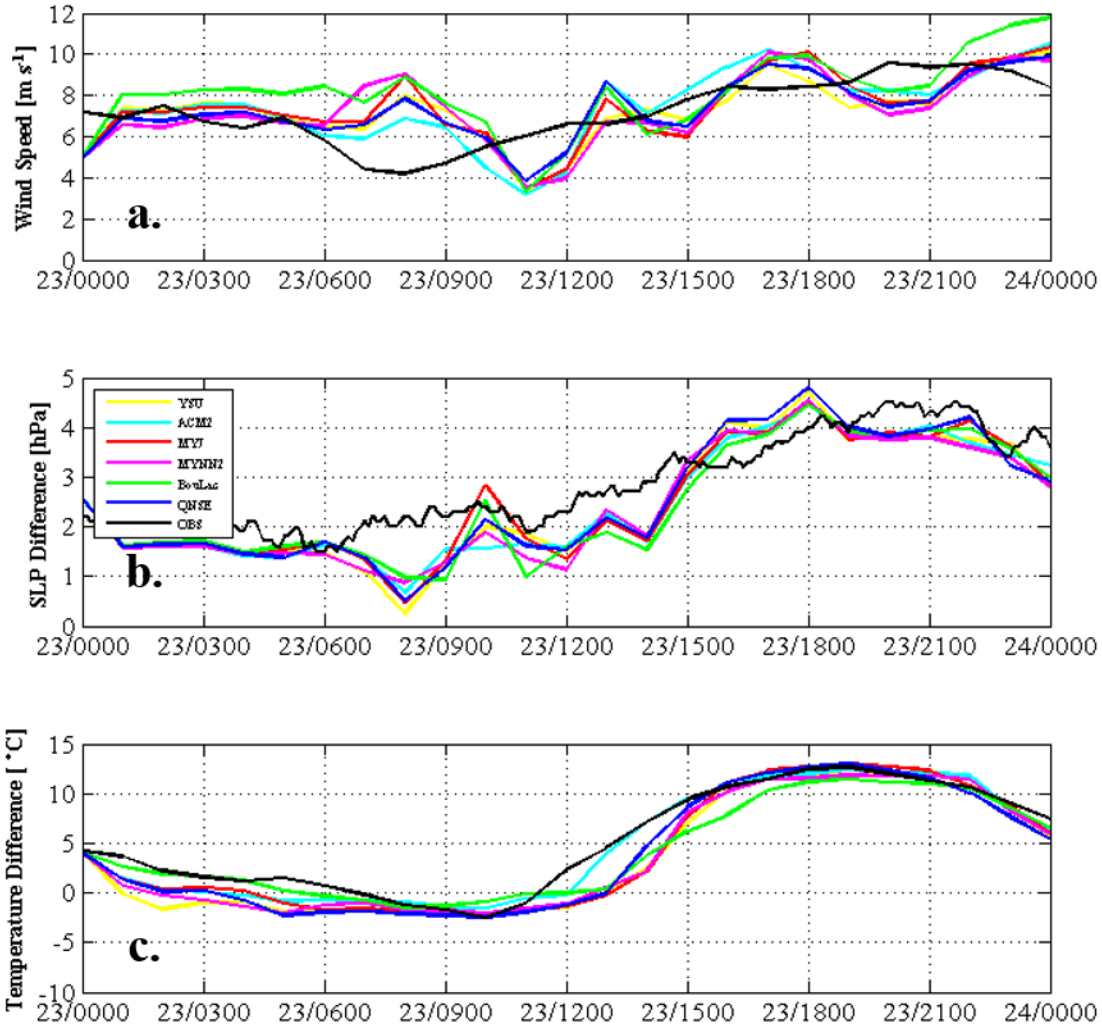

Figure 4.27. As in Fig. 4.19 but for 23 June 2013.

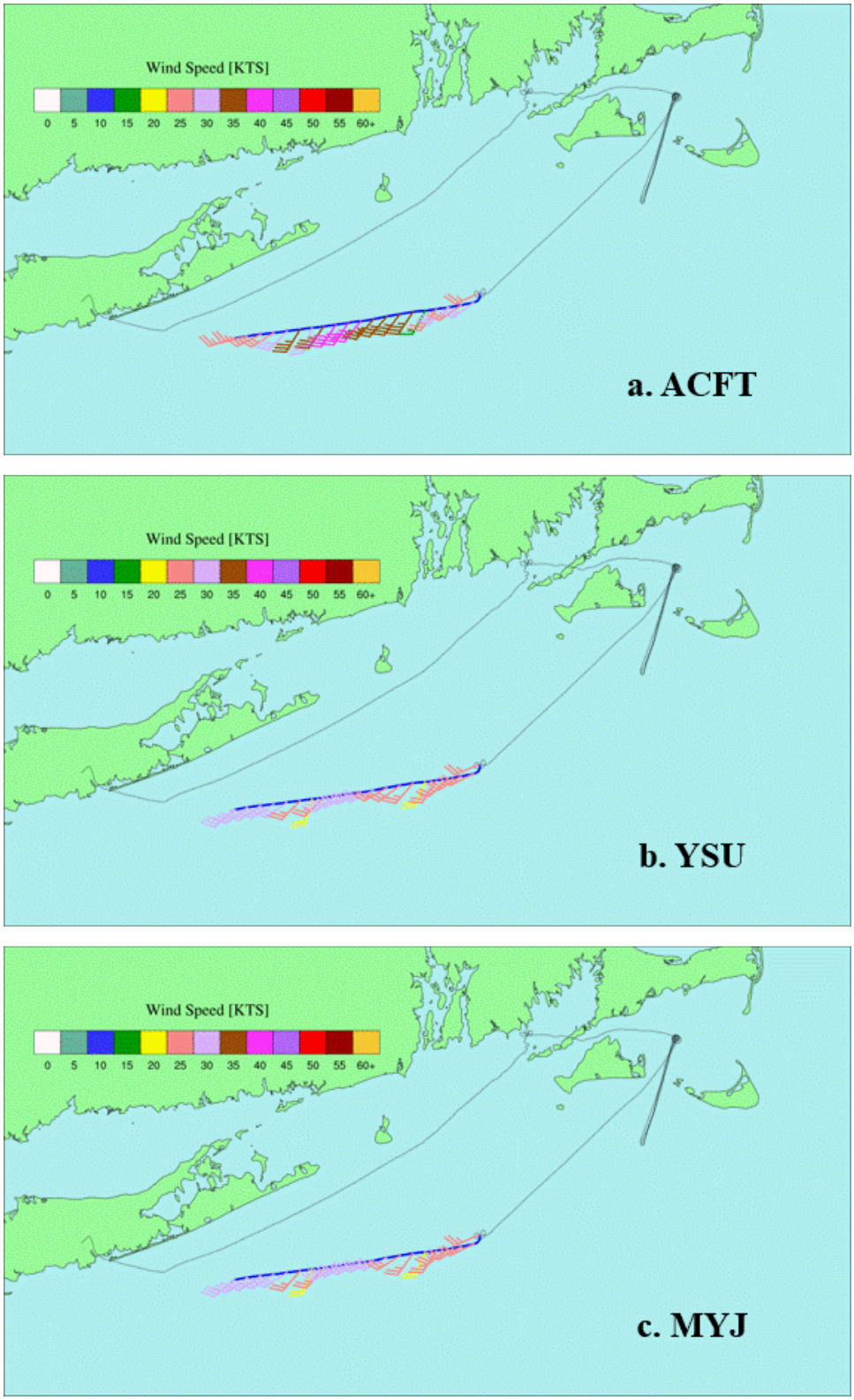

Figure 4.28. Winds along the slant-sounding flight track (30 – 800 m) from 1836 – 1856 UTC 23 June 2013 for (a) aircraft observations, (b) the YSU PBL scheme, and (c) the MYJ PBL scheme.

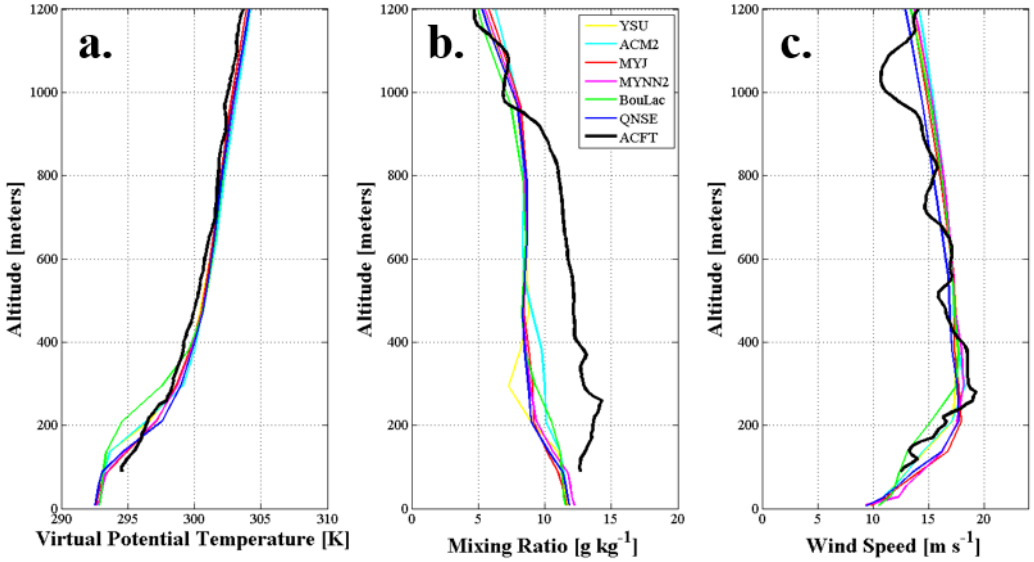

Figure 4.29. As in Fig. 4.20 but for the aircraft spiral around the Cape Wind tower at ~2205 UTC 23 June 2013.

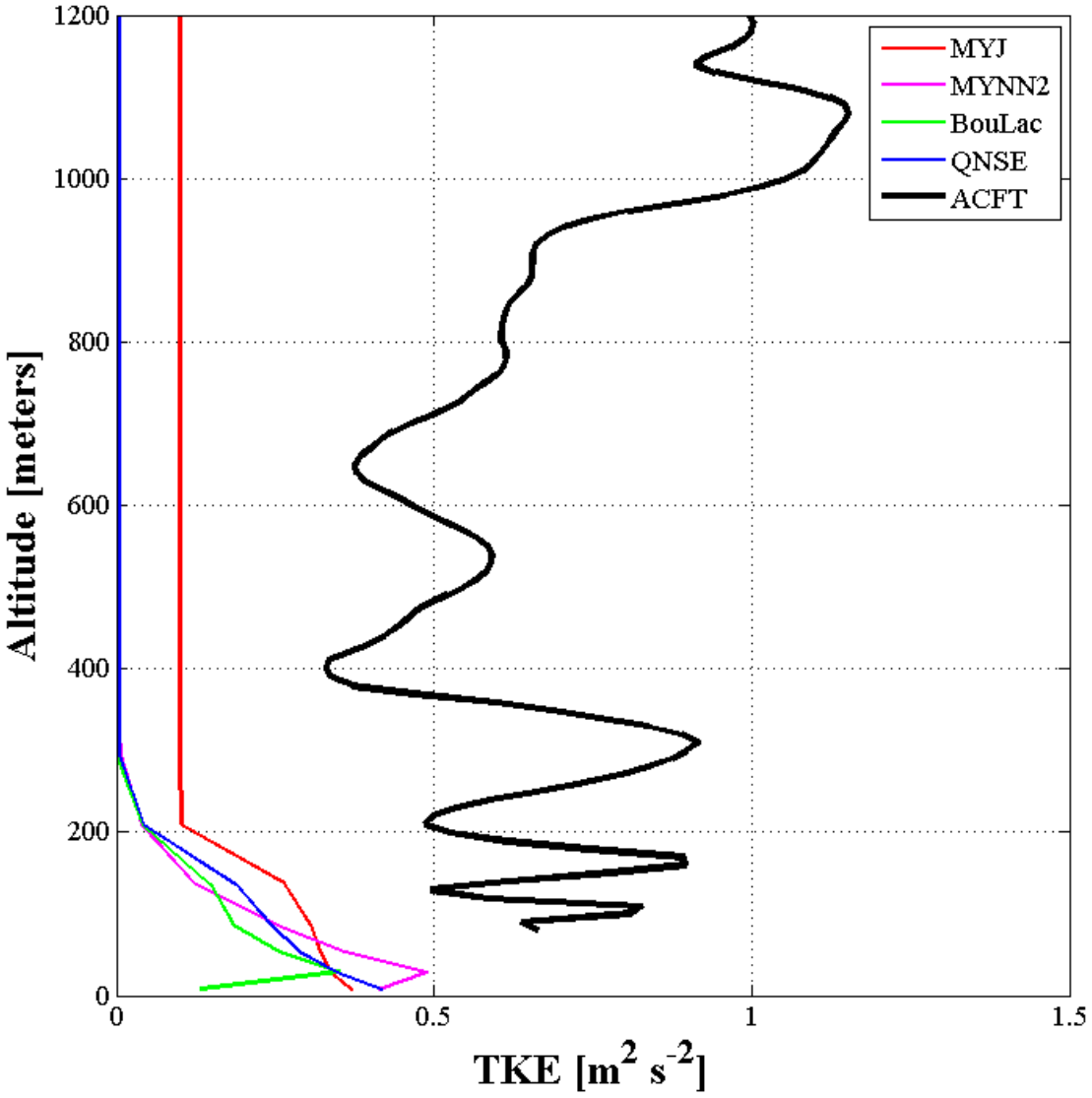

Figure 4.30. As in Fig. 4.21 but for the aircraft spiral around the Cape Wind tower at ~2205 UTC 23 June 2013.

Chapter 5: WRF MABL Sensitivity to SST Field and Initial/Boundary Conditions

5.1 Overview

To assess the relative contributions of factors other than the PBL schemes to the model MABL structure, several sensitivity tests were performed. First, the sensitivity to the SST field was assessed by performing two separate experiments that perturbed the prescribed SST field using two different numerical techniques. Second, several initial and lateral boundary condition options were chosen to force the model in order to investigate the effects of different analyses on the model simulations. Third, the model forecast lead time was increased by 48 hours. All studies focused on the 23 June flight and used only the model 4-km outer domain.

5.2 Sensitivity to Sea Surface Temperature Field

Since all schemes displayed somewhat similar errors for wind shear, stability, temperature, etc. it was hypothesized that the sea surface temperature field in the model may be a leading cause of the errors. Nantucket Sound is a shallow body of water that is susceptible to solar heating, so the concern was that the coarse, daily products may have led to errors in SST due to large diurnal and seasonal swings in observed SST. The products are expected to be several degrees too cold in the warm season and several degrees too warm in the cool season.

So far for this study two SST products have been used; the National Center for Environmental Prediction (NCEP) 0.5 x 0.5 degree daily SST product was prescribed for each of the 90 WRF historical runs, and the $1/12^{th}$ degree daily SST product (beginning in 2005) was used for the IMPOWR flight cases. To quantify the errors in these SST products in the vicinity of the Cape Wind tower, a study of the performance of the two SST products at NDBC buoy 44020 in

Nantucket Sound was conducted for the five-year period of 2009-2013. Fig. 5.1 shows mean error by month for both products. The products are too cool during the warm season with the errors peaking in August at -1.17 and -1.89 °C for the 1/12th and 0.5 degree products, respectively. During the cool season the products are too warm; 1.23 °C error for the 1/12th degree product in December and 1.57 °C error for the 0.5 degree product in January. It is worth mentioning that buoy 44020 is located about 20 km east of the Cape Wind tower in a region that is dominated by semidiurnal tidal mixing of much cooler water that has made its way south from the Gulf of Maine, so the SST biases are most likely larger in the vicinity of the Cape Wind tower. Similar temperature mean error seasonal trends were found at the Chatham, MA sounding location but not at adjacent buoy locations in Massachusetts Bay to the north and further offshore to the south and west, further supporting the idea of large localized SST errors in Nantucket Sound resulting in localized wind speed and temperature biases near the surface.

5.2.1 SST Perturbation Experiment #1

To test how sensitive the low-level (< 300 m) wind field in the models is to the SST field, a perturbation field was devised that aimed to warm the waters in western Nantucket Sound and cool the waters to the east in order to better represent the SST field in Nantucket Sound. A piecewise function (Eq. 5.1) centered around 17.7 °C was applied to the SST field that had the desired effect in Nantucket Sound as well as slightly cooling the waters offshore of Rhode Island and southeastern Massachusetts which would increase the land-sea temperature contrast in southeastern New England and possibly increase the boundary layer winds (Fig. 5.2). Offshore regions to the south were warmed by a maximum 1.5 °C while the Gulf of Maine, Nantucket Shoals and Georges Bank regions were cooled by 1.5 °C. The benefit of using a piecewise

continuous function is that the SST field remains continuous and no false SST fronts are added to the model simulation which would result in undesired thermal boundaries.

$$\text{Eq. 5.1} \quad f(x) = \begin{cases} -1.5, & if\ x < 16.1292 \\ 1.5\sin(x - 17.7), & if 16.1292 \leq x \geq 19.2702 \\ 1.5, & if\ x > 19.2702 \end{cases}$$

Figure 5.3 shows 4-km domain model and observed time-series of wind speed in Nantucket Sound, north-south sea-level pressure differences and land-sea temperature contrasts for the control (CTL) and SST perturbation (PERT) simulations for the YSU and MYJ schemes. While the surface temperatures show an expected (1 – 2 °C) decrease in the land-sea temperature contrast throughout the afternoon and evening (1500 – 0000 UTC), there is no visible change in surface winds in Nantucket Sound or the Nantucket – Boston sea-level pressure gradient. At 2200 UTC the effect of the SST perturbation is visible in the 2-m temperature field, with slight cooling in the northeast quadrant of the domain and warming along the New Jersey coast (Fig. 5.4a,b). Similarly there is a small increase (decrease) in PBL depth over the areas of SST warming (cooling) (Fig. 5.4c,d). However, there remains no discernible difference in the jet-level (300 m AGL) winds at 2200 UTC or throughout the simulation (Fig. 5.4e,f). Profiles of virtual potential temperature, mixing ratio and wind speed at the Cape Wind tower at 2200 UTC show a decrease in the MABL depth for the YSU scheme (~50 m) and slight warming in the MYJ scheme (< 1 °C) as well as increases in MABL mixing ratios for both schemes (~1 g kg^{-1}) (Fig. 5.5). The SST perturbations also showed a small increase in wind speed (~1 m s^{-1}) from 100 – 200 m AGL. The stable layer in the models (100 – 200 m) appears to cap the effects of the perturbed SST, resulting in minimal changes in atmospheric structure above the inversion.

5.2.2 SST Perturbation Experiment #2

In order to bound the impacts of the magnitude of the sea surface temperature field, a simple perturbation experiment was devised where +1.5 °C and -1.5 °C perturbations were added across the entire field. Time-series of surface variables for the positive (POS) and negative (NEG) SST perturbations are shown in Fig. 5.6. As to be expected, the negative SST perturbation shows a larger land-sea surface temperature contrast (~3 °C) which results in a larger north-south SLP gradient (~0.2 hPa) during the early afternoon (1600 – 1800 UTC) (Fig. 5.6b,c). Despite the larger SLP gradient in the negative perturbation simulations, the positive perturbation simulations showed stronger winds (2 – 3 m s^{-1}) in Nantucket Sound throughout the afternoon and evening, suggesting that the warmer SST field allows for more mixing of higher momentum to the surface from above. The warmer (cooler) 2-m temperature fields for the positive (negative) perturbation simulations at 2200 UTC are visible in Fig. 5.7(a,b). Similarly the increase (decrease) in MABL depth for the positive (negative) perturbations is shown in Fig. 5.7(c,d). Slight increases in wind speed at jet-level (300 m) are visible over eastern Long Island Sound and over the Gulf of Maine for the negative perturbation (Fig. 5.7e,f). At the Cape Wind tower at 2200 UTC the warmer SST field translates to a warmer and moister (~2.5 g kg^{-1}) MABL with a weaker inversion at the top of the MABL (Fig. 5.8). Stronger winds below ~80 m are shown for the positive perturbation simulations but the negative perturbation simulations show stronger winds between 100 – 200 m which further suggests more mixing within MABL due to warmer sea surface temperatures.

5.3 Varying Initial and Lateral Boundary Conditions

Various analyses use different data assimilation techniques as well as different horizontal and vertical resolutions and model physics. Dissimilar soil moisture fields in the analyses may

result in altered diurnal heating of the land surface in the WRF simulations, which may in turn affect sea breeze circulations and low-level pressure, momentum, thermal and moisture fields. Differences in the position, strength and timing of synoptic systems such as the Bermuda high pressure system or frontal systems may also play a role in altering the atmospheric structure at various levels throughout the troposphere and boundary layer. In order to assess the impact of varying the initial and lateral boundary conditions on the LLJ event of 23 June, the 4-km WRF simulations were conducted using hourly RAP analyses, 3-hourly NAM analyses, 3-hourly GFS analyses and 3-hourly NARR analyses.

Time-series of model surface variables for the 4 sets of simulations (YSU PBL scheme) are shown in Fig. 5.9. While most simulations show fair agreement with the land-sea surface temperature contrast in the afternoon and evening, the RAP-WRF simulation lags behind in the diurnal heating of the land surface by ~2 hours. The NARR-WRF simulation is 1 – 2 °C cooler over the land during the afternoon, resulting in weaker wind speeds (2 – 4 m s^{-1}) in Nantucket Sound during this period compared with observations. The NAM-WRF and GFS-WRF simulations show the strongest winds from 1700 – 2000 UTC while RAP-WRF and NAM-WRF show the strongest winds at the end of the forecast period (2200 – 0000 UTC). Most simulations show a peak in the SLP gradient at ~1800 UTC, while the GFS-WRF agrees better with observations and shows the peak SLP gradient a couple hours later (1900 – 2000 UTC). The GFS-WRF also agrees best with wind speed observations following the peak pressure gradient (2000 – 0000 UTC).

Spatial plots of 2-m temperature for all initial and boundary condition options using the YSU PBL scheme are shown for 2200 UTC in Fig. 5.10. The RAP-WRF simulation shows the strongest surface heating throughout New England and the Mid-Atlantic states. The GFS-WRF

shows strong heating in New England, but the coolest temperatures over New Jersey and Pennsylvania. Both the GFS-WRF and the RAP-WRF show closed SLP contours associated with the heating over southeastern New Hampshire. The NARR-WRF shows cooler inland New England temperatures and the weakest SLP pressure gradient across southeastern New England out of the four simulations. This translates to a shallower PBL over inland New England in the NARR-WRF simulation and ultimately weaker wind speeds aloft (Figs. 5.11-12). At 300 m AGL the RAP-WRF and NAM-WRF simulations show the strongest winds (> 22 m s^{-1}) offshore of Massachusetts, as well as strong winds over Block Island Sound (>18 m s-1). The RAP-WRF also extends these strong winds westward over eastern Long Island which agrees well with aircraft observations taken during a slant-sounding flight leg at ~2300 UTC (Fig. 4.18).

The weaker winds (~2 m s^{-1}) within the MABL for the NARR-WRF simulation are also visible in profiles at the Cape Wind tower (Fig. 5.13). The warmer MABL and weaker inversion in the NARR-WRF simulation do not translate to stronger winds near the surface compared with the other simulations, since the NARR-WRF does not show stronger winds aloft that could mix down to the surface. The other simulations show fair agreement in wind speed below 200 m. At the observed LLJ level of ~300 m both the GFS-WRF and NAM-WRF agree well with observations. The RAP-WRF and the NARR-WRF are too weak by 2.5 and 4.5 m s^{-1}, respectively.

5.4 Varying Forecast Lead Time

In order to assess how the forecast lead time affects the model simulation around the time of the 23 June aircraft flight, a separate 72-hour NARR-WRF simulation was conducted beginning at 0000 UTC on 21 June and running to 0000 UTC 24 June. The results were compared with the NARR-WRF simulation initialized at 0000 UTC 23 June. Time-series of 4-km domain model

surface variables for both the 24-hour (NARR24) and 72-hour (NARR72) simulations are shown in Fig. 5.14. The 72-hour simulations show a warmer land surface during the night (0300 – 1000 UTC) that results in a stronger land-sea temperature contrast during the afternoon (1800 – 2100 UTC). However, the stronger heating of the land surface does not translate to a stronger north-south SLP gradient, and wind speeds during the afternoon are 1 – 2 m s^{-1} weaker than in the 24-hour simulations.

Spatial plots of 2-m temperature, PBL height, and 300-m wind speed verifying at 2200 UTC 23 June 2013 for both sets of simulations using the YSU PBL scheme are shown in Fig. 5.15. The 72-hour simulation (forecast hour 70) shows cooler temperatures over the New England Shelf compared with the 24-hour simulation, but the PBL height and 300-m wind speed plots are very similar. The structure of the LLJ east of Massachusetts is retracted southwards slightly in the 72-hour simulation, but the magnitude and spatial extent remain very similar.

Profiles of virtual potential temperature, mixing ratio, and wind speed at the Cape Wind tower at 2200 UTC 23 June show that the majority of the differences between the two sets of simulations are in the MABL (Fig. 5.15). The 72-hour simulations are cooler (~2 °C) and drier (~1 g kg^{-1}) in the MABL. The resulting stronger stability between 100 – 200 m leads to weaker winds by ~1 m s^{-1} below 100 m. Above the MABL the two sets of simulations appear nearly identical. This sensitivity test to forecast lead time shows that model differences in thermal and momentum profiles are largely confined to the boundary layer.

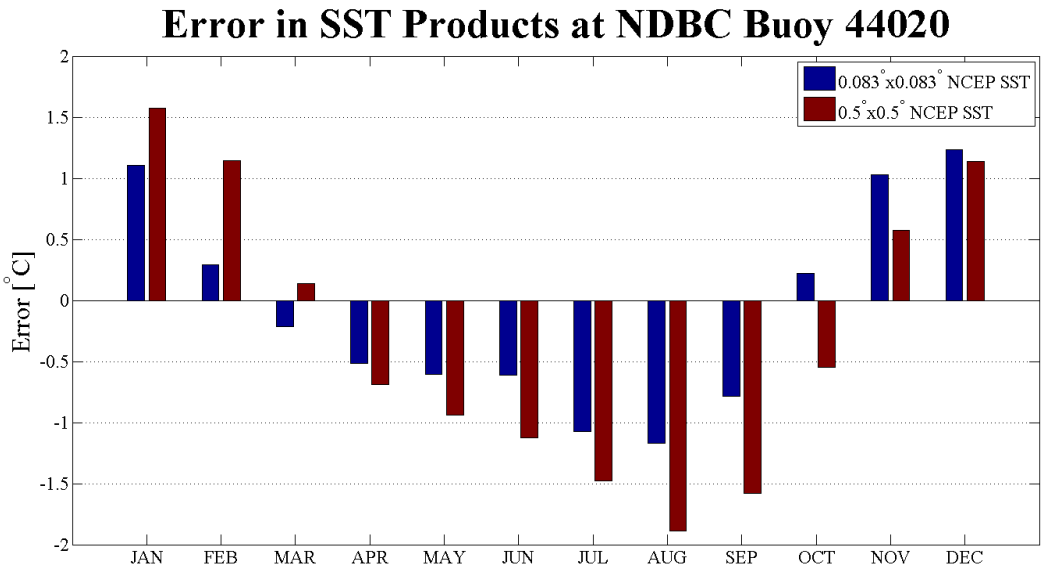

Figure 5.1. Mean error (°C) by month for the 1/12th degree (blue) and 0.5 degree daily SST products compared against observed water temperatures at buoy 44020 in Nantucket Sound for the 5-year period 2009 – 2013.

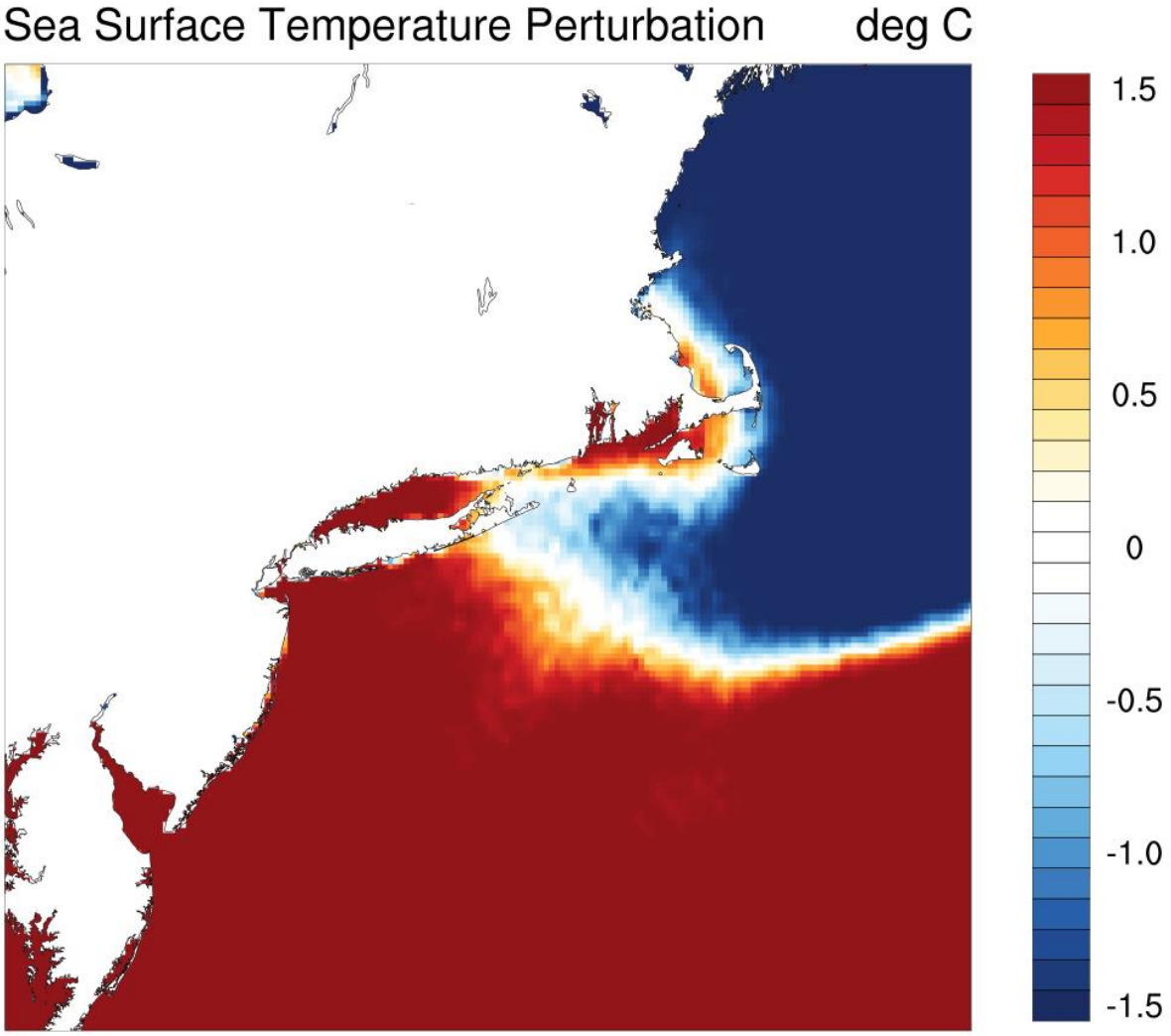

Figure 5.2. Map showing the perturbation field added to the prescribed sea surface temperature field (°C).

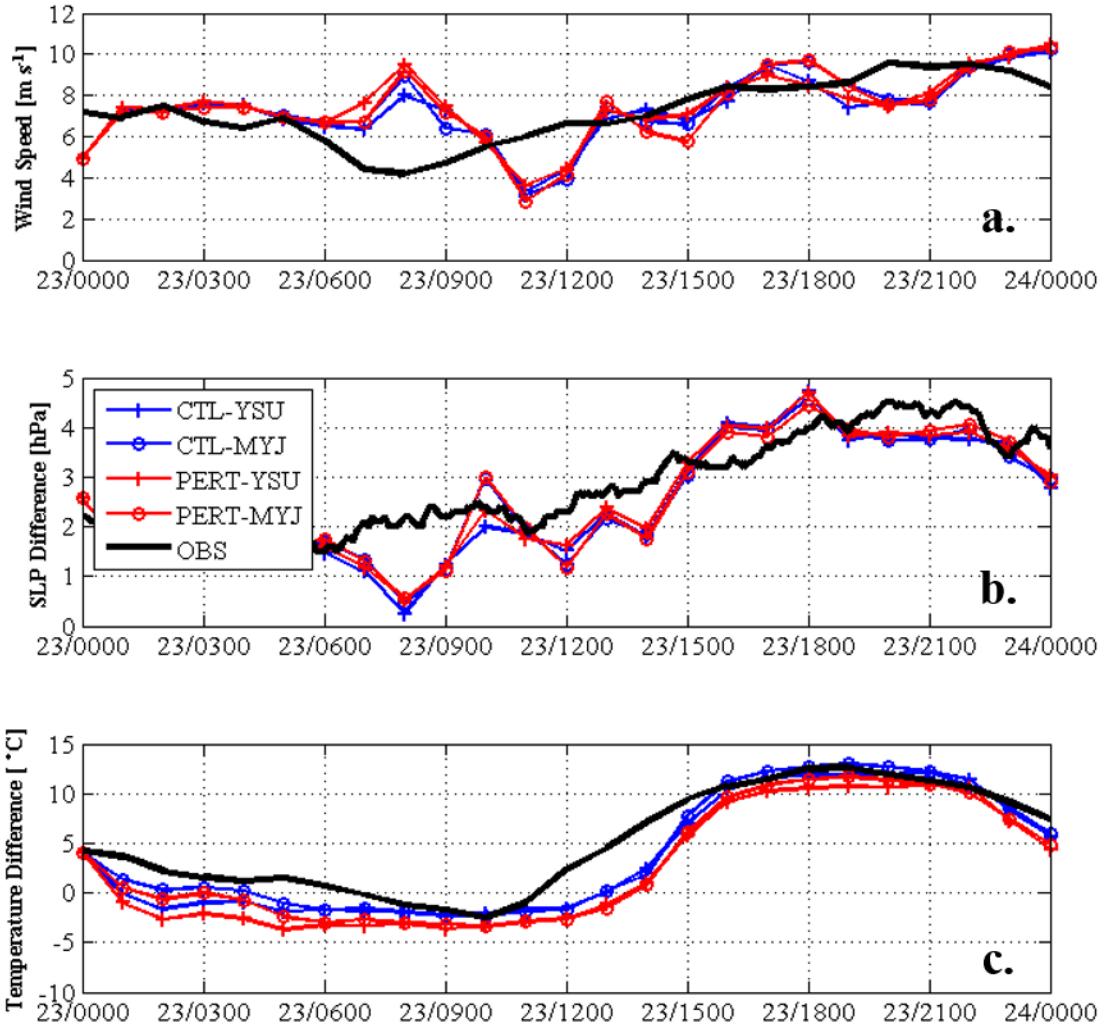

Figure 5.3. (a) Time-series of 4-km domain model 10-m winds vs. observed wind speed (m s^{-1}) at buoy 44020 in Nantucket Sound, (b) modeled and observed sea-level pressure difference (hPa) between Nantucket Island, MA and Boston, MA and (c) the modeled and observed temperature difference (°C) between BAF and buoy 44025 for 20 June 2013. The YSU (+) and MYJ (o) schemes for the control and SST perturbation model runs are shown blue and red, respectively.

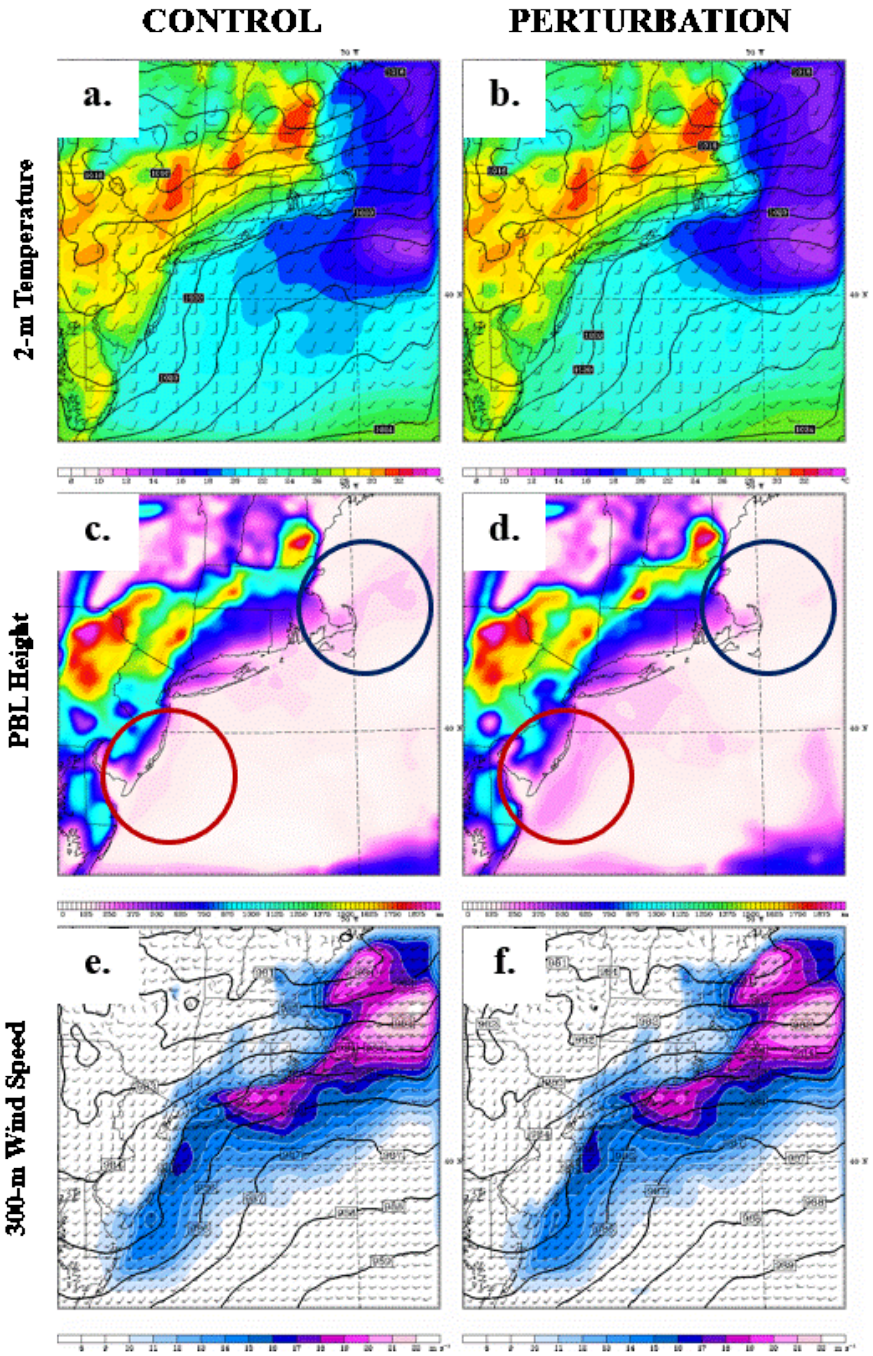

Figure 5.4. Spatial plots of 4-km domain model control (a) 2-m temperature (°C, shaded contours), sea level pressure (hPa, black contours), and 10-m wind (kts, barbs), (c) PBL height (m, shaded contours), and (e) 300-m wind speed (m s-1, shaded contours), 300-m pressure (hPa, black contours). (b,d,f) same as in (a,c,e) but for the SST perturbation run. All plots are for forecast hour 22 valid at 2200 UTC 23 June 2013. Red circles denote area of increased PBL heights in PERT compared with CTL. Blue circles denote area of decreased PBL heights in PERT compared with CTL. All plots are for the YSU PBL scheme.

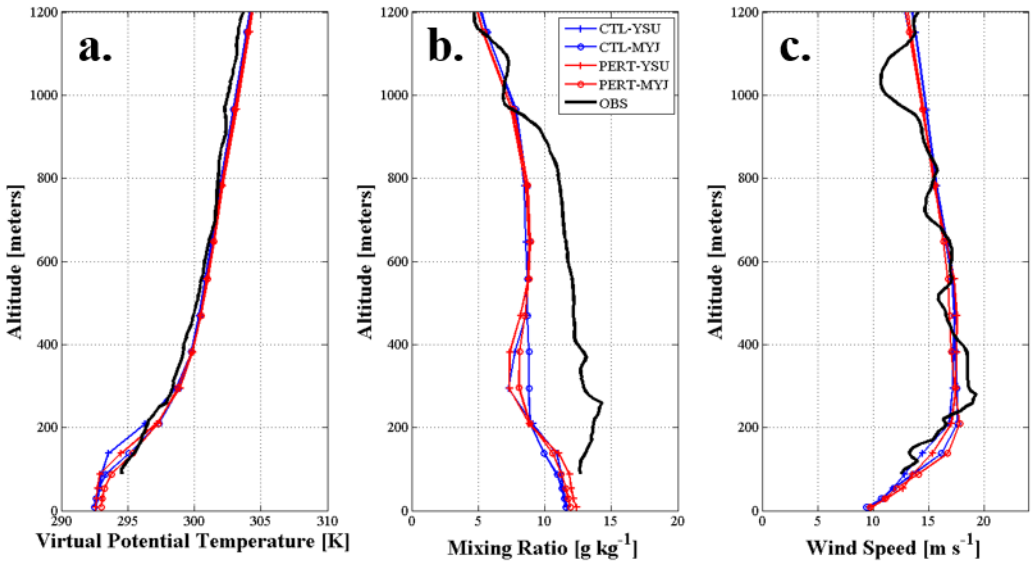

Figure 5.5. Aircraft observations (black lines) of (a) virtual potential temperature (K), (b) mixing ratio (g kg^{-1}), and (c) wind speed (m s^{-1}) collected during a spiral around the Cape Wind tower at ~2205 UTC 23 June 2013. Model 4-km domain profiles valid at 2200 UTC 23 June 2013 for the control (CTL) and SST perturbation (PERT) are shown in blue and red, respectively, for the YSU (+) and MYJ (o) schemes.

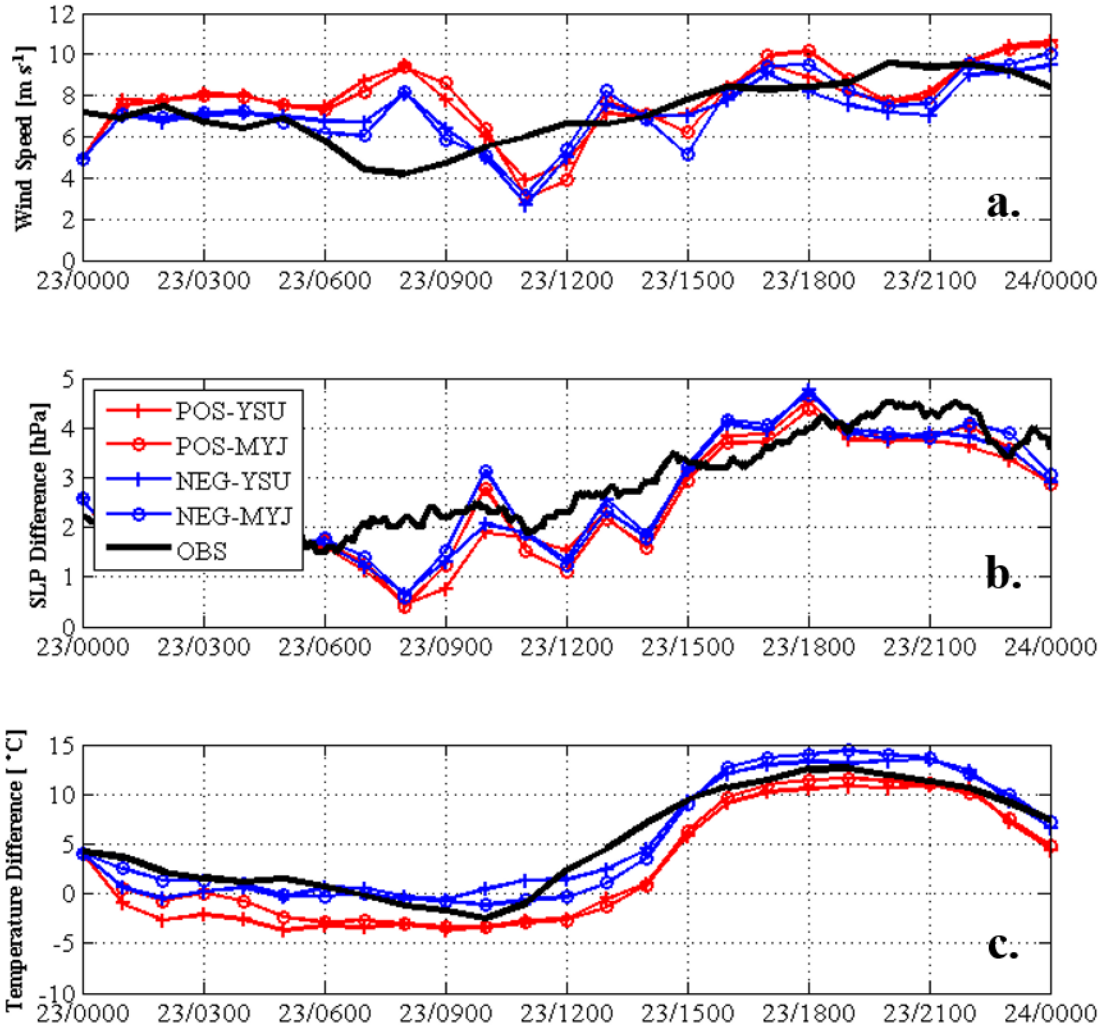

Figure 5.6. As in Fig. 5.3 but for the positive (POS) and negative (NEG) SST perturbation 4-km domain model runs.

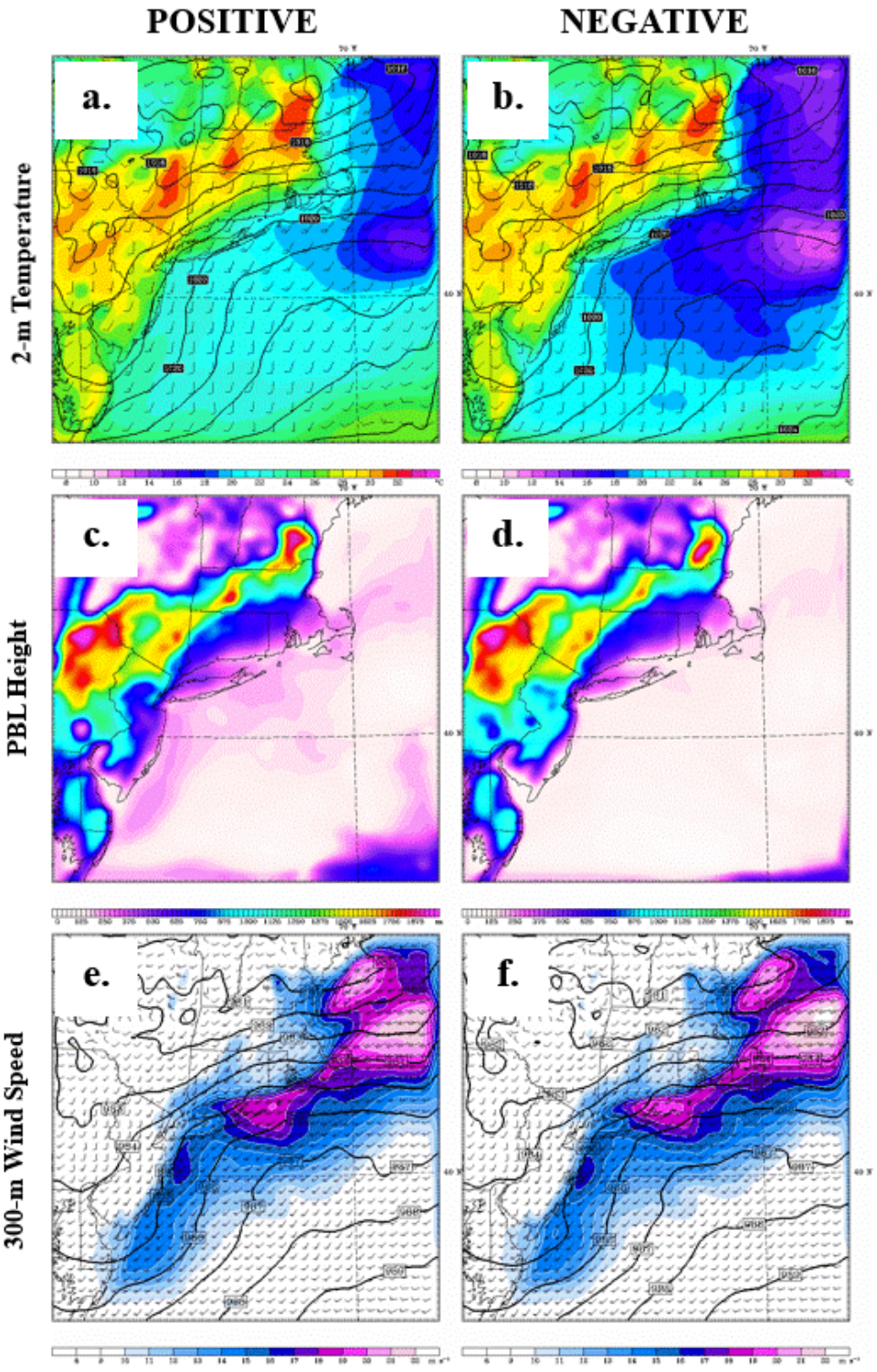

Figure 5.7. As in Fig. 5.4 but for the positive (a,c,e) and negative (b,d,f) SST perturbation 4-km domain model runs.

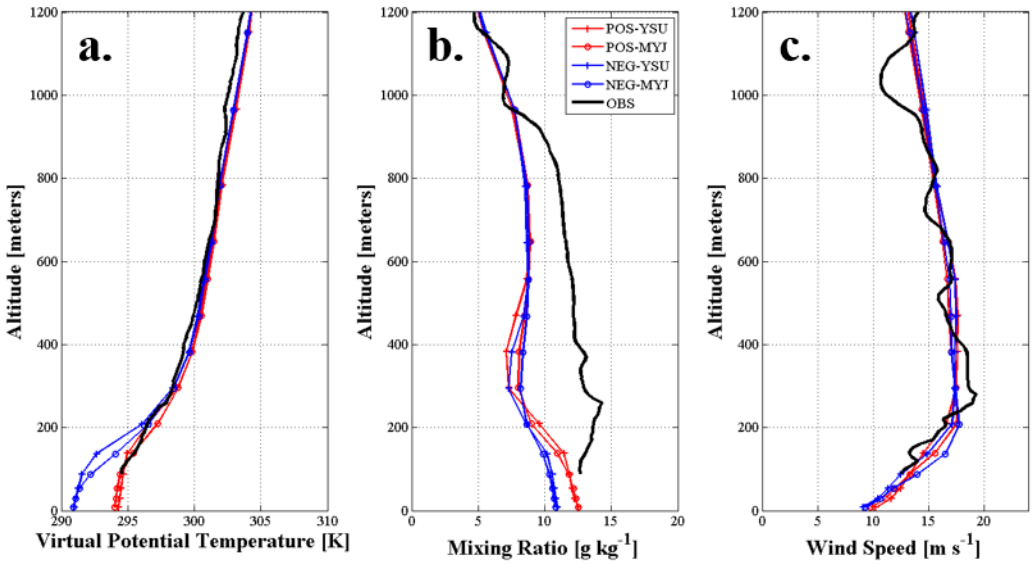

Figure 5.8. As in Fig. 5.5 but for the positive (POS, red) and negative (NEG, blue) SST perturbation 4-km domain model runs.

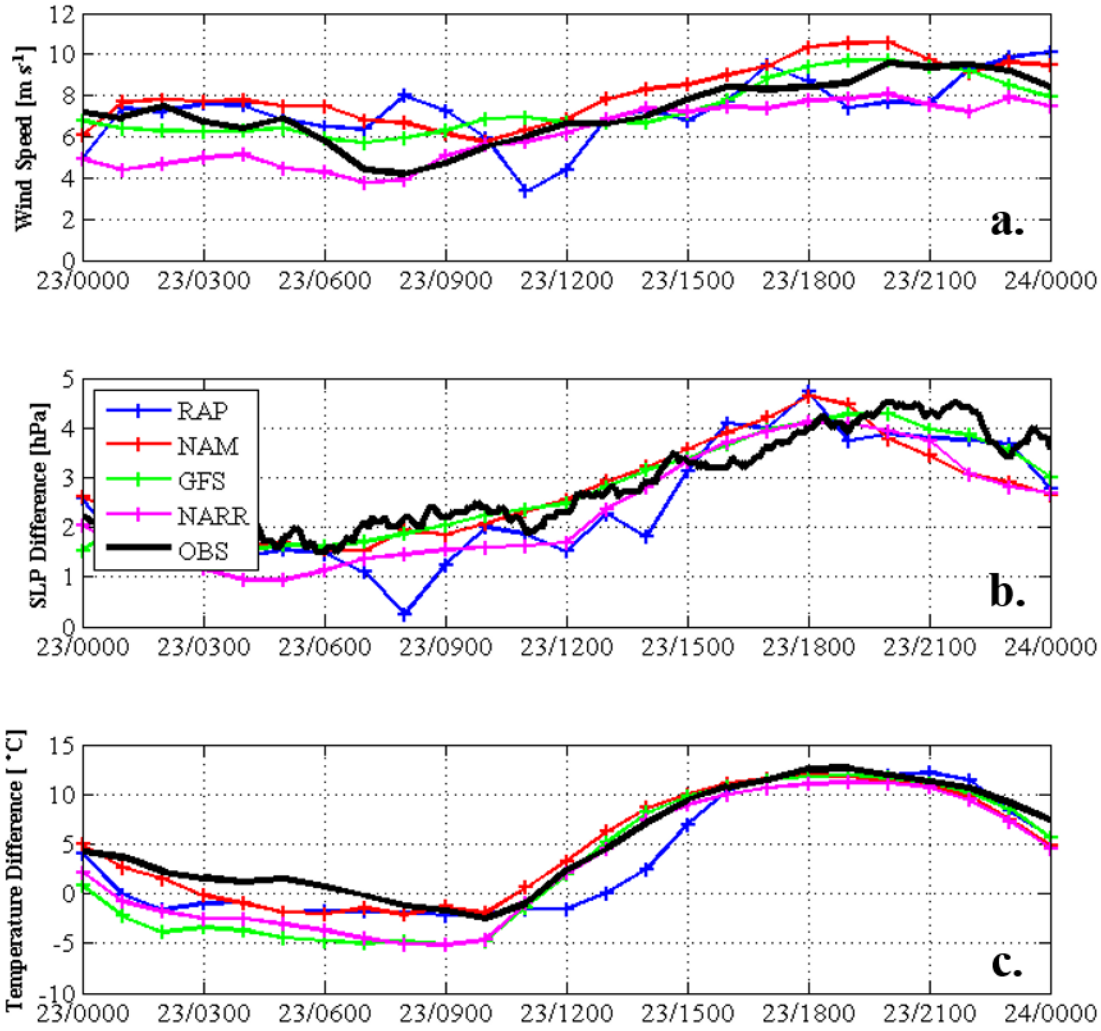

Figure 5.9. As in Fig. 5.3 but for the RAP (blue), NAM (red), GFS (green), and NARR (magenta) analysis initial and lateral boundary condition runs.

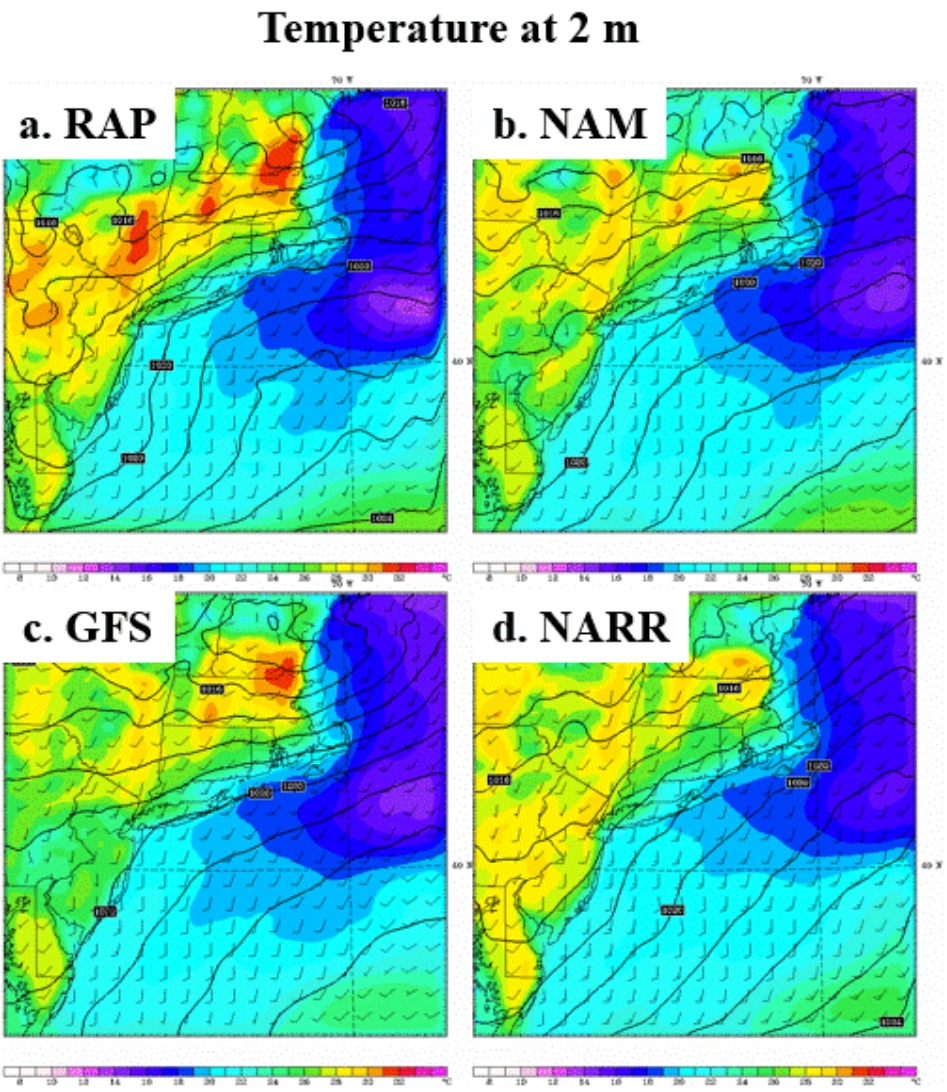

Figure 5.10. Spatial plots of 4-km domain model PBL height (m) for forecast hour 22 valid at 2200 UTC 23 June 2013 for (a) RAP, (b) NAM, (c) GFS, and (d) NARR analysis initial and lateral boundary conditions.

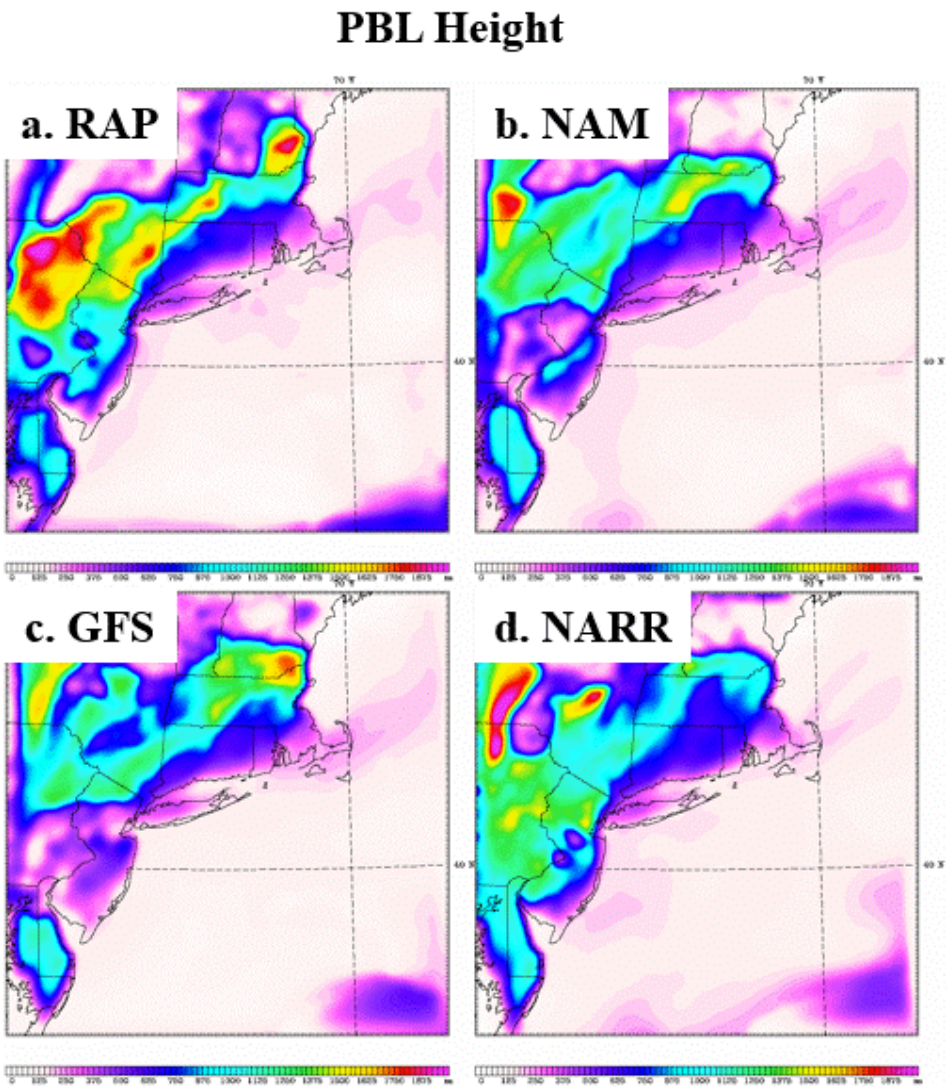

Figure 5.11. As in Fig. 5.10 but for PBL height (m).

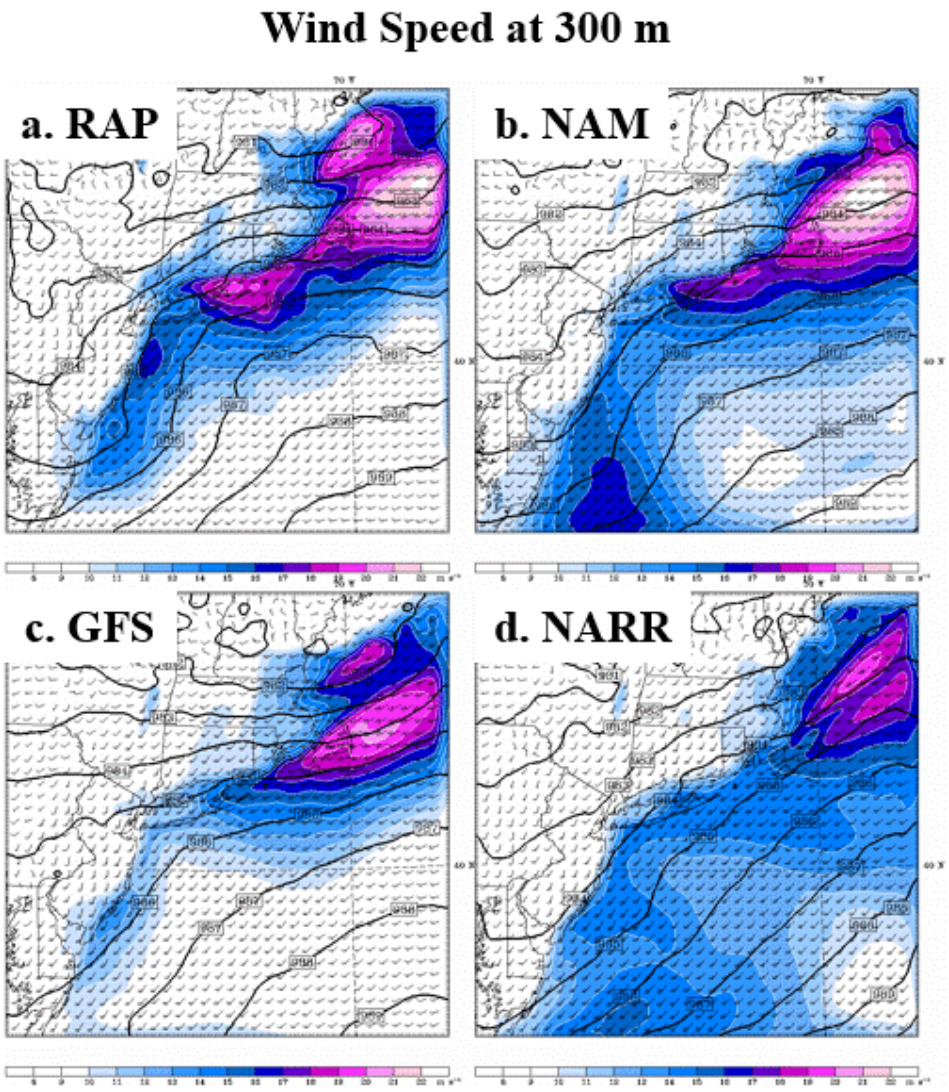

Figure 5.12. As in Fig. 5.10 but for 300-m wind speed (m s^{-1}).

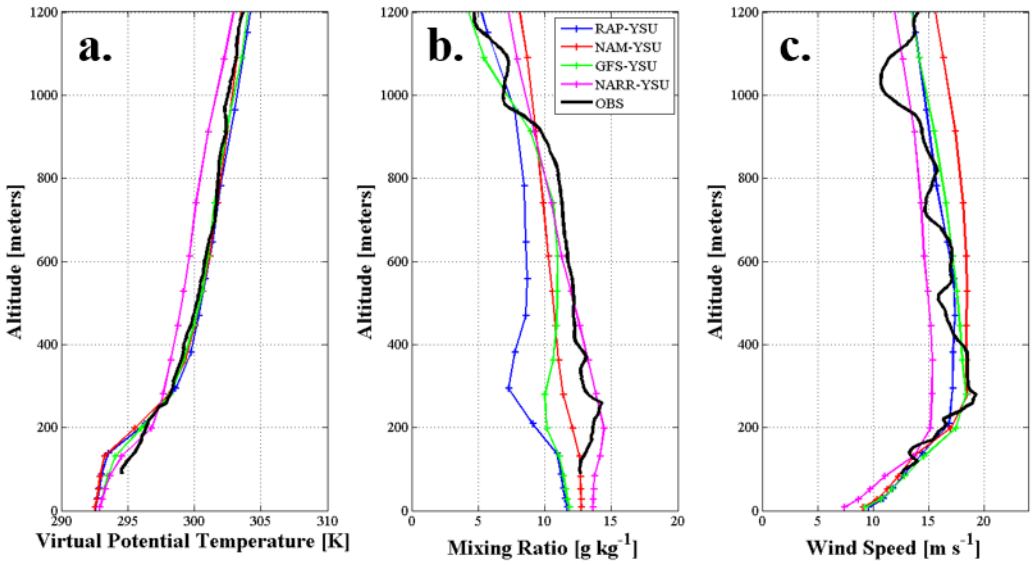

Figure 5.13. As in Fig. 5.5 but for RAP (blue), NAM (red), GFS (green), and NARR (magenta) analysis initial and lateral boundary condition model runs. Only the YSU PBL scheme is shown here.

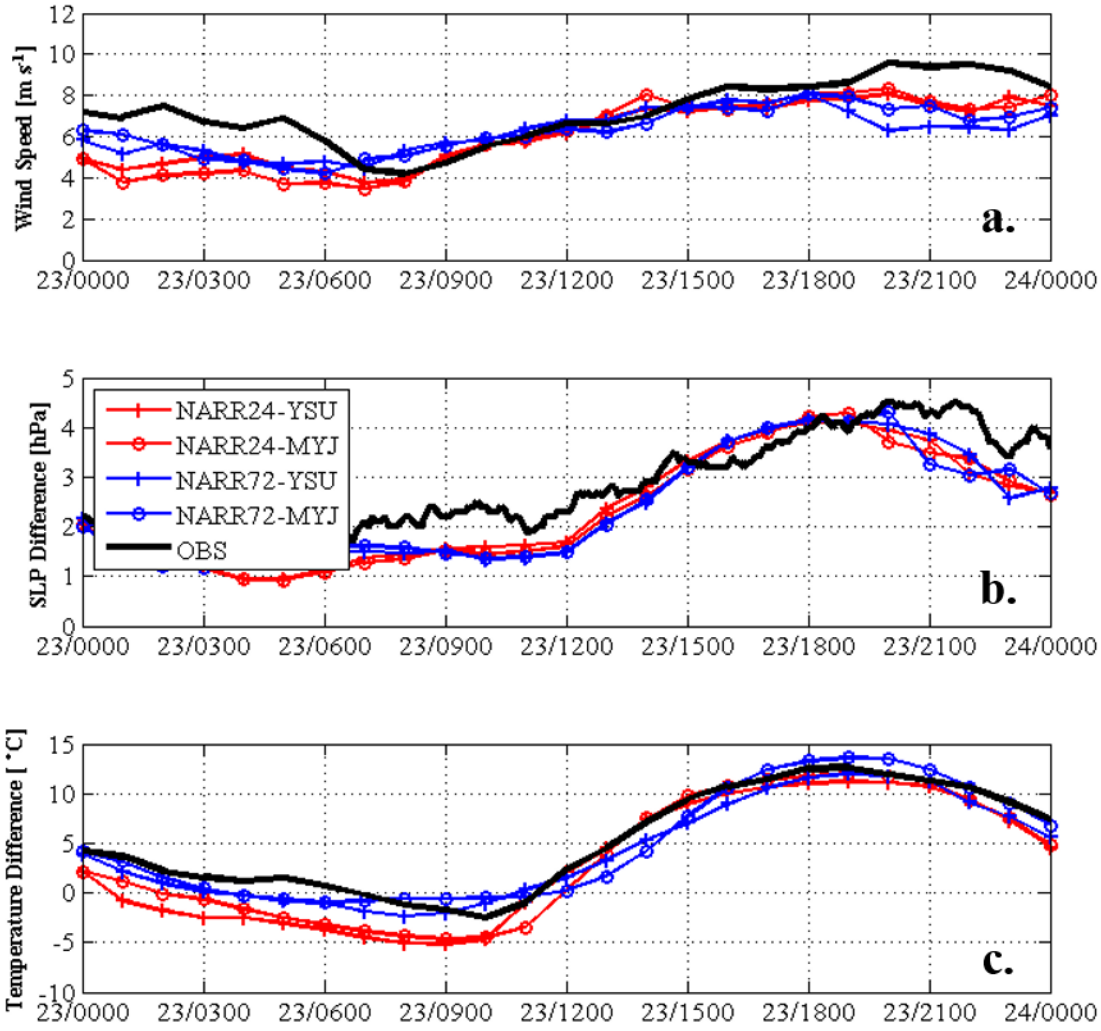

Figure 5.14. As in Fig. 5.3 but for the 24-hour (NARR24) and 72-hour (NARR72) simulations.

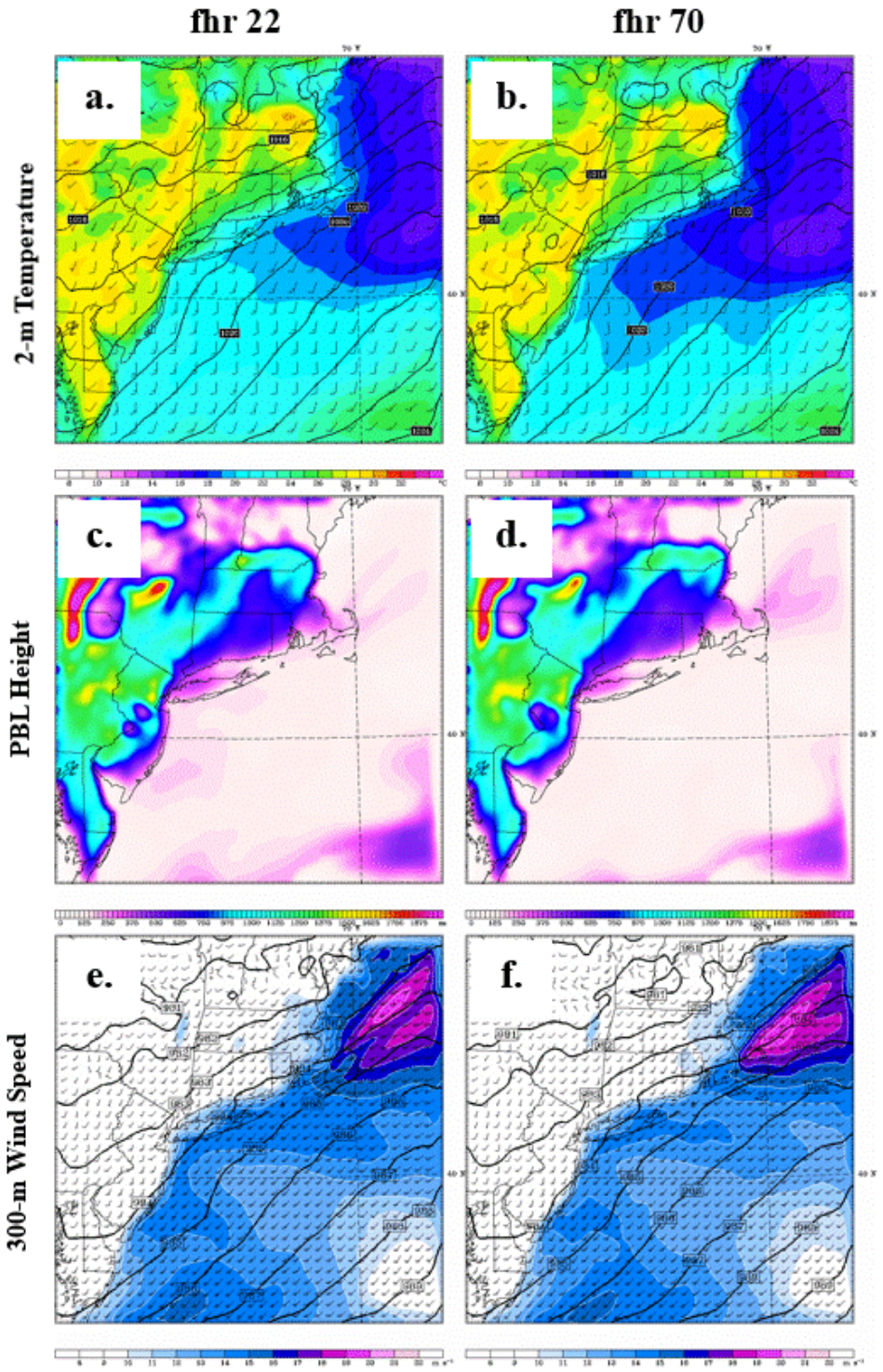

Figure 5.15 As in Fig. 5.4 but for (a,c,e) the 22-hour and (b,d,f) the 70-hour forecasts using NARR analyses as initial and lateral boundary conditions. All plots are for the YSU PBL scheme.

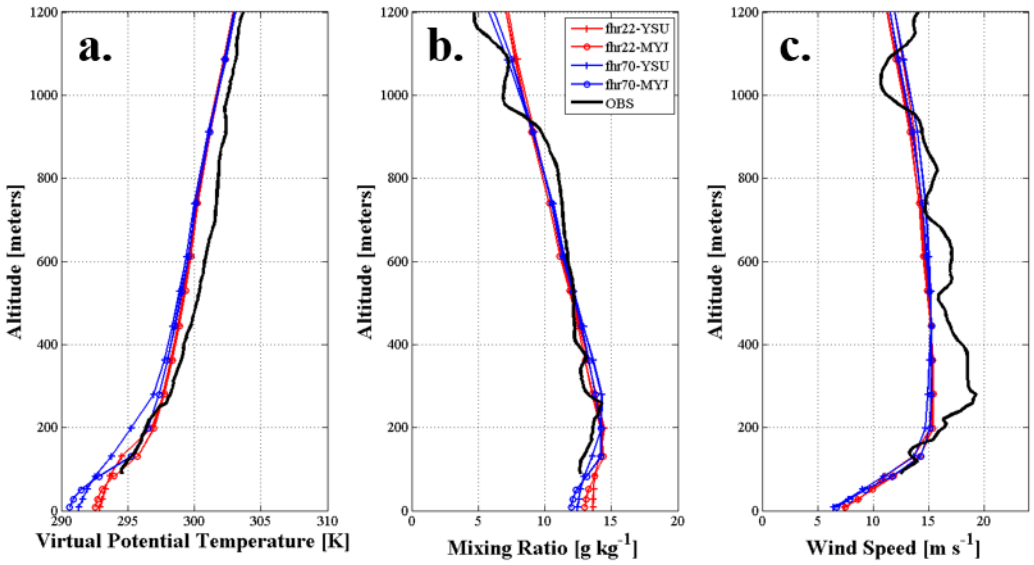

Figure 5.16 As in Fig. 5.5 but for the 22-hour (red) and 70-hour forecasts using the NARR analyses as initial and lateral boundary conditions. YSU (+) and MYJ (o) PBL schemes are shown here.

Chapter 6: Conclusions

Six WRF planetary boundary layer schemes were evaluated over the coastal waters of Southern New England in an effort to quantify the systematic errors in wind speed, temperature and moisture produced by the schemes and how they varied in time and space. Several observational datasets were used to compare with model output that included moored buoys, ocean platforms, and land surface stations. Unique to this study, vertical observations in the coastal marine environment were provided by the Cape Wind tower and aircraft observations as part of the IMPOWR field campaign. The main conclusions of this study are summarized as follows:

1. Mean errors in wind speed, temperature and dew point temperature are highly variable in the coastal and offshore regions, varying by season, diurnal period, latitude and distance from the coast. All PBL schemes generally show similar ME values, with the exception of the BouLac scheme which shows warmer surface temperatures during the cool season and stronger (weaker) winds over the land (water).
2. Model verification results at the Cape Wind tower in Nantucket Sound show that wind speed biases are negative for all schemes, diurnal periods and seasons. Biases are largest at the 20-m level during the warm season (except for the BouLac scheme) most likely due to prevailing warm southerly flow over a colder SST field in the model leading to increased stability and less mixing of momentum down to the surface.
3. During the cool season the flow regime is mostly offshore, resulting in cold continental air flowing over warm water and the development of a neutral to unstable MABL. Cool

season wind speed biases are largest at 60 m, likely due to enhanced mixing resulting from warmer model SST fields and resultant sensible heat fluxes.

4. During the warm season perturbations to the SST field result in changes to the MABL structure. Specifically a warmer SST field was shown to improve the profiles of moisture and temperature throughout the shallow MABL, as well as minor improvements to the wind profile within the MABL. Minimal changes were observed above the MABL due to the presence of a strong stable layer.
5. Different analyses used as initial and lateral boundary conditions lead to larger variations in atmospheric structure throughout the MABL and free atmosphere than different PBL schemes alone.

These conclusions will be further discussed in the following sections.

6.1 Historical Study Period

In order to assess the short-range performance of WRF PBL schemes over the coastal waters of southern New England, WRF simulations were conducted for 90 dates from 2003 – 2011, equally divided between warm (April – October) and cool (September – March) seasons as well as 0000 UTC and 1200 UTC model initialization times. Simulations were performed out to 30 forecast hours for 6 WRF PBL schemes; two first-order schemes (YSU and ACM2) and four 1.5-order schemes (MYJ, MYNN2, BouLac and QNSE). Model results were compared with NDBC moored buoys and C-MAN stations, NWS ASOS stations, and 9 years of multi-level observations from the Cape Wind meteorological mast located in Nantucket Sound.

During the warm season at the Cape Wind tower, ME in wind speed was largest at the 20-m level for most schemes (-0.2 – -0.8 m s^{-1}) and decreased in magnitude with height, resulting in modeled shear profiles greater than that of the observations. Large temperature biases (~2 °C) were found at both the 10- and 55-m levels, and the models typically displayed a slightly more stable temperature profile than observed. The model shear and temperature profiles suggest the existence of a shallow stable layer in the models that inhibits the mixing of momentum from the 60-m level and above down to the surface as evident in the observations. Also, the large temperature biases, along with the knowledge of Nantucket Sound being a small, shallow body of water that is consistently warmer than adjacent waters, lead to the hypothesis that localized cool biases in the prescribed RTG SST products may be the leading cause of the observed errors through erroneously small surface fluxes and resultant maintenance of a shallow near-surface stable layer. The localized nature of these biases is supported by the ME in wind speed and temperature at buoy 44020 in Nantucket Sound varying in sign and magnitude from adjacent land and water stations.

During the cool season at the Cape Wind tower, ME in wind speed for the 6 schemes was consistently negative and increasing in magnitude with height from 20 m (< 0.8 m s^{-1}) to 60 m (< 1.4 m s^{-1}). Temperature ME values were negative yet smaller than during the warm season (< 1.8 °C) and ~0.5 °C smaller at 10 m than at 55 m. Model stability profiles for the cool season were generally neutral to unstable for all schemes, due to the presence of a superadiabatic surface layer that is commonly observed over the water during outbreaks of cold continental air. Wind directions at the tower during the cool season were observed to be largely westerly to northwesterly which would allow for the advection of cold continental air over the warmer waters and establishment of a neutral to unstable regime. Similar to the warm season, it is hypothesized that SST errors may be the leading cause of the difference between model and observed shear profiles. If the SST field

is consistently too warm during the cool season the sensible heat fluxes will be larger than observed, resulting in a deeper mixed layer in the models and a more relaxed shear profile compared with observations. This theory is further corroborated by cool season wind speed biases at buoy 44020 in Nantucket Sound being positive and larger in magnitude than adjacent stations, implying that the biases are localized and that they switch sign from positive at the buoy height of 5 m to negative at 20 m.

6.2 IMPOWR Long-EZ Flights 20-23 June 2013

During the spring and summer of 2013 – 14 several Long-EZ aircraft flights were conducted in the MABL over Nantucket Sound and surrounding waters as part of the IMPOWR field campaign. This study focused on 3 flights that occurred during the 4-day period of 20 – 23 June 2013 in steady southwesterly flow that intensified in strength throughout the period. The flights occurred in the afternoons and evenings of 20, 21 and 23 June, during the periods of maximum diurnal heating and strongest observed wind speeds. A weak low-level wind maximum (~10 m s^{-1}) was observed at ~150 m over Nantucket Sound on 20 June that increased in magnitude and height throughout the period, from 14 m s^{-1} at ~190 m on 21 June to 19 m s^{-1} at ~300 m on 23 June. Model profiles compared with profiles derived from aircraft spirals around the Cape Wind tower in Nantucket Sound revealed a near-surface temperature error in the models of ~1 – 2 °C, similar to the temperature ME found during the historical study. The cooler near-surface temperatures in the model simulations led to a shallower MABL as well as a stronger and deeper stable layer above the MABL than was observed, resulting in under-predictions of the LLJ altitude by 50 – 100 m. Due to the existence of the strong stable layers in the model simulations, the TKE-

prognostic schemes under-predicted TKE in the MABL (~0.5 – 1.0 m s^{-1}) resulting in under-mixing in the models and negative wind speed errors near the surface that became positive up through the MABL. Low-level (< 300 m) wind speeds were consistently under-predicted (5 – 7.5 m s^{-1}) by all model PBL schemes over the offshore waters south of Long Island and Block Island Sound for all 3 flights, with the models completely missing a strong south-southeasterly diurnal circulation south of Long Island on 20 June.

6.3 WRF MABL Sensitivity to SST Field and Initial/Boundary Conditions

Several sensitivity tests were conducted for simulations of the 23 June flight to assess the sensitivity of the MABL to the prescribed SST field as well as the initial and lateral boundary conditions used to force the simulations. Two SST sensitivity experiments were performed, the first of which applied a piecewise-continuous perturbation function to the SST field that had the effect of warming the waters of the southern upstream regions (+1.5 °C) while cooling the waters over the eastern New England Shelf and Gulf of Maine (-1.5 °C), increasing the land-sea temperature contrast in New England. In Nantucket Sound the perturbation had the effect of decreasing the MABL depth and weakening the stable layer above, allowing for more mixing of momentum from above and increased wind speeds (~1 m s^{-1}) from 100 – 200 m. The second SST experiment involved perturbing the entire SST field by +1.5 °C and -1.5 °C in an attempt to assess the impacts of SST errors on the MABL structure in Nantucket Sound. Despite increasing the land-sea temperature contrast and surface pressure gradient, the negative SST perturbation simulations resulted in slightly weaker winds at the surface over Nantucket Sound compared with the positive perturbation due to the increase in stability above the MABL. The positive SST perturbation

simulations agreed better with aircraft observations of temperature and mixing ratio (and showed small improvements in near-surface wind speed), placing more credence in the theory of SST errors being a contributor to model MABL biases.

Model simulations were performed using RAP, NAM, GFS and NARR analyses as initial and lateral boundary conditions to assess the sensitivity of the WRF MABL and LLJ structure to the analyses used to force the model. Large differences were found in diurnal heating of the land surface, with the RAP-WRF showing the strongest heating and the NARR-WRF under-heating the interior regions. The differences in land surface temperatures led to differences in PBL height as well as 300-m winds. The RAP-WRF showed LLJ magnitudes and spatial extents that agreed best with the aircraft observations, while the NARR-WRF under-predicted both the magnitude and spatial extent of the strong winds. A final experiment was performed using the NARR-WRF where the forecast lead time was increased by 48 hours to test how the MABL would evolve throughout a longer simulation. Compared with the control simulations, the extended forecast lead time resulted in cooler temperatures over the water, a stronger and deeper stable layer and less mixing of momentum down to the surface, leading to a larger under-prediction of wind speeds at the surface.

6.4 Future Work

In the future an effort should be made to acquire more in situ observations of the MABL over the New England Shelf in the interest of a better spatial and temporal understanding of model biases as well as more accurate offshore wind resource mapping. Targeted MABL aircraft observations during the cool season could provide valuable insight into the nature of the model

biases above the height of the Cape Wind tower used in this study. A similar study should utilize the NASA SPoRT MODIS SST product which is issued twice daily at 2-km resolution. The MODIS SST was neglected in this study due to data availability and consistency concerns, but the product would add the capability of a very high-resolution diurnally varying SST field that has been shown to improve coastal diurnal circulations and MABL structure. Similar to Suselj and Sood (2010), the master length scale in the MYJ surface layer and PBL schemes can be altered to better represent mixing in different stability regimes and potentially improve model momentum fields in the lower MABL. The seasonal and diurnal errors of the various available gridded analyses in the MABL should also be quantified over the New England Shelf region in the future since these analyses are commonly used to create offshore wind resource maps, either directly or through forcing mesoscale models.

Literature Cited

Archer, C. L., and Coauthors, 2013: Meteorology for Coastal/Offshore Wind Energy in the United States: Recommendations and Research Needs for the Next 10 Years. *Bull. Amer. Meteor. Soc.*, **95**, 515-519.

Angevine, W. M., M. Tjernström, and M. Žagar, 2006: Modeling of the Coastal Boundary Layer and Pollutant Transport in New England. J. Appl. Meteor. Climatol., **45**, 137-154.

Bell, G. D., and L. F. Bosart, 1988: Appalachian Cold-Air Damming. Mon. Wea. Rev., 116, 137-161.

Benjamin, S.G., W.R. Moninger, S.S. Weygandt, M. Hu, D. Devenyi, J.M. Brown, T. Smirnova, J. Olson, C. Alexander, K. Brundage, G. Grell, S. Peckham, T. L. Smith, S.R. Sahm, B. Jamison, 2009: Technical Review of Rapid Refresh/RUC Project, NOAA/ESRL/GSD internal review, 168 pp.

Black, P. G., E. A. D'Asaro, W. M. Drennan, J. R. French, P. P. Niiler, T. B. Sanford, E. J. Terrill, E. J. Walsh, and J. A. Zhang, 2007: Air-Sea Exchange in Hurricanes: Synthesis of Observations from the Coupled Boundary Layer Air-Sea Transfer Experiment, Bull. Amer. Meteor. Soc., **88**, 357-374.

Bougeault, P., P. Lacarrere, 1989: Parameterization of Orography–Induced Turbulence in a Mesobeta—Scale Model. *Mon. Wea. Rev.*, **117**, 1872–1890.

Colle, B. A., J. B. Olson, and J. S. Tongue, 2003: Multiseason Verification of the MM5. Part I: Comparison with the Eta Model over the Central and Eastern United States and Impact of MM5 Resolution. Wea. Forecasting, **18**, 431-457.

Colle, B. A., and D. R. Novak, 2010: The New York Bight Jet: Climatology and Dynamical Evolution. *Mon. Wea. Rev.*, **138**, 2385-2404.

Davies, P. A., 2000: Development and mechanisms of the nocturnal jet. *Meteor. Appl.*, **7**, 239-246.

Draxler, R.R. and G.D. Rolph, cited 2014: HYSPLIT (HYbrid Single-Particle Lagrangian Integrated Trajectory) Model. [Available online at http://www.arl.noaa.gov/HYSPLIT.php.]

Dudhia, Jimy, 1996: A multi-layer soil temperature model for MM5. The Sixth PSU/NCAR Mesoscale Model Users' Workshop.

Dvorak, M. J., B. A. Corcoran, J. E. Ten Hoeve, N. G. McIntyre, and M. Z. Jacobson, 2013: US East Coast offshore wind energy resources and their relationship to peak-time electricity demand. *Wind Energy*, **16**, 977-997.

Edson, J.B., et al., 2007. The coupled boundary layers and air–sea transfer experiment in low winds (CBLAST-LOW). Bull. Amer. Meteor. Soc. **88 (3),** 341–356

Garratt, J. R., 1992: *The atmospheric boundary layer*. Cambridge University Press, pp. 316.

Helmis, C. G., Q. Wang, G. Sgouros, S. Wang, and C. Halios, 2013: Investigating the Summertime Low-Level Jet Over the East Coast of the USA: A Case Study. Boundary-Layer Meteor, **149**, 259-276.

Holtslag, A.A.M., and B.A. Boville, 1992: Local versus nonlocal boundary-layer diffusion in a global climate model, J. Climate, **6**, 1825-1842.

Hong, Song–You, Yign Noh, Jimy Dudhia, 2006: A new vertical diffusion package with an explicit treatment of entrainment processes. *Mon. Wea. Rev.*, **134**, 2318–2341.

Hong, X. D., P. J. Martin, S. P. Wang, and C. Rowley, 2009: High SST variability south of Martha's Vineyard: Observation and modeling study. J. Mar. Syst., **78**, 59-76.

Hsu, S. A., Eric A. Meindl, and David B. Gilhousen, 1994: Determining the Power-Law Wind-Profile Exponent under Near-Neutral Stability Conditions at Sea, J. Appl. Meteor., **33**, 757-765.

Iacono, M. J., J. S. Delamere, E. J. Mlawer, M. W. Shephard, S. A. Clough, and W. D. Collins, 2008: Radiative forcing by long–lived greenhouse gases: Calculations with the AER radiative transfer models. *J. Geophys. Res.*, **113**.

Janjic, Zavisa I., 1994: The Step–Mountain Eta Coordinate Model: Further developments of the convection, viscous sublayer, and turbulence closure schemes. *Mon. Wea. Rev.*, **122**, 927–945.

Kain, John S., 2004: The Kain–Fritsch convective parameterization: An update. *J. Appl. Meteor.*, **43**, 170–181.

LaCasse, K. M., M. E. Splitt, S. M. Lazarus, and W. M. Lapenta, 2008: The Impact of High-Resolution Sea Surface Temperatures on the Simulated Nocturnal Florida Marine Boundary Layer. Mon. Wea. Rev., **136**, 1349-1372.

Mellor, G. L., and T. Yamada, 1982: Development of a turbulence closure model for geophysical fluid problems. Rev. Geophys., **20**, 851-875.

Mesinger, F., and Coauthors, 2006: North American Regional Reanalysis. *Bull. Amer. Meteor. Soc.*, **87**, 343–360.

Mlawer, Eli. J., Steven. J. Taubman, Patrick. D. Brown, M. J. Iacono, and S. A. Clough (1997),

Radiative transfer for inhomogeneous atmospheres: RRTM, a validated correlated–k model for the longwave. *J. Geophys. Res.*, **102**, 16663–16682.

Nakanishi, M., and H. Niino, 2009: Development of an improved turbulence closure model for the atmospheric boundary layer. *J. Meteor. Soc. Japan*, **87**, 895–912.

NDBC, 2009: Handbook of Automated Data Quality Control Checks and Procedures. NDBC Technical Document 09-02. [Available online at http://www.ndbc.noaa.gov/NDBCHandbookofAutomatedDataQualityControl2009.pdf.]

Nunalee, C. G., and S. Basu, 2014: Mesoscale modeling of coastal low-level jets: implications for offshore wind resource estimation. *Wind Energy*, **17**, 1199-1216.

Ohsawa, T., S. Shimada, J. Tambke, and B. Lange, 2009: A study on effective usage of mesoscale model for accurate offshore wind simulation. Proc. of EOW 2009, PO. 11, Stockholm, Sweden. [Available online at http://proceedings.ewea.org/offshore2009/allfiles2/401_EOW2009presentation.pdf.]

Olson, J. B., B. A. Colle, N. A. Bond, and N. Winstead, 2007: A Comparison of Two Coastal Barrier Jet Events along the Southeast Alaskan Coast during the SARJET Field Experiment. Mon. Wea. Rev., **135**, 3642-3663.

Pleim, Jonathan E., 2007: A Combined Local and Nonlocal Closure Model for the Atmospheric Boundary Layer. Part I: Model Description and Testing. *J. Appl. Meteor. Climatol.*,**46**, 1383–1395.

Shimada, S., T. Ohsawa, S. Chikaoka, and K. Kozai (2011), Accuracy of the Wind Speed Profile in the Lower PBL as Simulated by the WRF Model, *Sola*, **7**, 109-112.

Shimada, S., and T. Ohsawa, 2011: Accuracy and Characteristics of Offshore Wind Speeds Simulated by WRF. Sola, **7**.

Shin, H. H., and S. Y. Hong, 2011: Intercomparison of Planetary Boundary-Layer Parametrizations in the WRF Model for a Single Day from CASES-99, *Boundary Layer Meteor.*, **762 139(2)**, 261-281.

Skamarock, W. C., and Coauthors, 2008: A description of the Advanced Research WRF version 3. NCAR Tech. Note NCAR/TN-475+STR, 113 pp, doi:10.5065/D68S4MVH.

Stull, R. B., 1988: An Introduction to Boundary Layer Meteorology. Springer, 670 pp.

Storm, B., J. Dudhia, S. Basu, A. Swift, and I. Giammanco, 2009: Evaluation of the Weather Research and Forecasting Model on Forecasting Low-level Jets: Implications for Wind Energy. Wind Energy, **12**, 81-90.

Sukoriansky, S., B. Galperin, and V. Perov, 2006: A quasi-normal scale elimination model of

turbulence and its application to stably stratified flows. Nonlin. Processes Geophys., **13**, 9-22.

Suselj, K., and A.Sood, 2010: Improving the Mellor-Yamada-Janjic Parameterization for wind conditions in the marine planetary boundary layer. Boundary Layer Meteor., **136**, 301-324.

Xie, B., J. C. H. Fung, A. Chan, and A. Lau, 2012: Evaluation of nonlocal and local planetary boundary layer schemes in the WRF model. J. of Geophys. Res.: Atmos., **117**, D12103.

Zhang, J. A., F.D. Marks, Jr., M.T. Montgomery, and S. Lorsolo, 2011: An estimation of turbulent characteristics in the low-level region of intense Hurricanes Allen (1980) and Hugo (1989). Mon. Wea. Rev., **139**, 1447-1462.